Title
A MEASUREMENT OF THE ANOMALOUS GYRO-MAGNETIC RATIO OF THE MUON

Authors
Schrank, G.
Henry, G.R.
Swanson, R.

Publication Date
1965-10-28

UCRL-16469

University of California

Ernest O. Lawrence Radiation Laboratory

A MEASUREMENT OF THE ANOMALOUS GYROMAGNETIC RATIO OF THE MUON

DISCLAIMER

UCRL-16469
UC-34 Physics
TID-4500
(46th Ed.)

UNIVERSITY OF CALIFORNIA

Lawrence Radiation Laboratory
Berkeley, California

AEC Contract No. W-7405-eng-48

A MEASUREMENT OF THE ANOMALOUS GYROMAGNETIC RATIO OF THE MUON

G. Schrank, G. R. Henry, and R. Swanson

October 28, 1965

Printed in USA. Price $6.00. Available from the Clearinghouse for Federal Scientific and Technical Information, National Bureau of Standards, U. S. Department of Commerce, Springfield, Virginia.

CONTENTS

A MEASUREMENT OF THE ANOMALOUS GYROMAGNETIC RATIO OF THE MUON

G. Schrank* and G. R. Henry†

Princeton University and
Lawrence Radiation Laboratory
University of California
Berkeley, California

and

R. Swanson

University of California, San Diego

October 28, 1965

ABSTRACT

A measurement of (g-2) for the free, positive muon was made. The value obtained was $(g-2)_\mu = 2(0.00106 \pm 0.000067)$ and is to be compared with the theoretical value of 2(0.0011654).

The technique consisted of trapping polarized muons, one at a time, in an essentially homogeneous, 28-kG magnetic field for about eight muon lifetimes. While in this field, the muon undergoes cyclotron motion (ω_c) and its magnetic dipole moment also precesses (ω_p) about the magnetic field vector. The difference frequency ($\omega_c - \omega_p$) was measured and this quantity, in appropriate units, is $(g-2)_\mu$.

I. INTRODUCTION

In this report a measurement of the g-factor of the free, positive muon is described. The g-factor is defined as the ratio of the muon's magnetic moment (about 1 in units of $e\hbar/2m_0c$) to the muon's spin (equal to 1/2 in units of $\hbar$). Here in the Introduction a few remarks on the purpose of the measurement are followed by a brief, descriptive outline of the experiment. The main body of the report consists of an outline of the theory, detailed descriptions of the apparatus, procedures of the experiment, and analysis of the data.

The muon occupies a unique position among the current spectrum of "elementary" particles. All experiments to date indicate that it is nothing more than a heavy electron. That is, when the weak interaction is neglected, the muon interacts only electromagnetically with all other particles. In addition, it is electromagnetically orthogonal to its ground state (the electron)— i.e., $\mu \rightarrow e + \gamma$ is not observed. Although no quantitatively correct theory of strong interactions exists, the electromagnetic interactions are properly described by today's Quantum Electrodynamics. Given the photon-electron-muon system, QED can compute correctly the interactions among them. But QED is not constructed to account for any underlying connection between these objects. Consequently, the central question in the electromagnetic world today is, "Why the muon?". Indeed, since so much is known about the electromagnetic world, it is not too much to hope that a solution of the muon problem might point the way to a solution of the more complex problem of the strongly interacting particles. In any event, just because it is possible to compute with QED, any experiment that measures a property of the muon is in part a test of QED and, separately, is also potentially capable of solving the muon puzzle.

Adding to the interest of this measurement of $(g-2)_\mu$ is the precision with which the g-factor can be determined. QED predicts (Refs. 1 to 9) that $g_\mu = 2(1.001165)$. But, by means of the appropriate experimental procedure, it is possible to measure directly the quantity $(g-2)_\mu$. Since $(g-2)_\mu = 2(0.001165)$, a measurement of $(g-2)_\mu$ to a given precision yields a value for g that is about 1000 times more precise. Consequently it is $(g-2)_\mu$ rather than g directly that was measured in this experiment.

Our technique of the $(g-2)_\mu$ measurement can be described in a few words. Muons were trapped in a uniform magnetic field, and the precession frequency of the spin vector was compared to the cyclotron frequency of the momentum vector. The difference between these two frequencies, experimentally determined, is proportional to $(g-2)_\mu$ for the muon. This work was started in 1960 (Ref. 10), when the CERN group (Refs. 11-14) was measuring the same quantity. Our goal was to obtain an independent and, we hoped, a more accurate result. As our work progressed, it became apparent that our accuracy would not be as good as theirs; but since our experimental setup was so different from the CERN apparatus, any systematic errors would probably be different; and since the g-factor is of considerable theoretical interest, our experiment was pursed until a result was obtained. In brief, and stated in the most favorable way, our result indicates that if QED breaks down at small distances, the breakdown occurs at dimensions smaller than the numbers given in the following table:

Table I. Limits of validity of quantum electrodynamics

	Princeton-Univ. of Calif.	CERN
Photon propagator cutoff	$\Lambda \geq 0.25$ BeV/c $\lambda_0 \leq 0.8 \times 10^{-13}$ cm	$\Lambda \geq 1$ BeV/c $\lambda_0 \leq 0.2 \times 10^{-13}$ cm
Dispersion cutoff	$\Lambda \geq 0.4$ BeV/c $\lambda_0 \leq 0.5 \times 10^{-13}$ cm	$\Lambda \geq 1.7$ BeV/c $\lambda_0 \leq 0.12 \times 10^{-13}$ cm

A block diagram of the apparatus if shown in Fig. 1. A longitudinally polarized 150-MeV/c muon beam (Ref. 15) enters the central region of a uniform-field air-core dc solenoid through a gap in the windings. The beam is degraded to about 40 MeV/c with B_4C blocks; some multiple scattering of the beam also takes place in these blocks. Those muons leaving the blocks with sufficiently small pitch angles, defined by an $S_1S_2S_3\mu$ counter coincidence, are trapped inside the solenoid between two magnetic mirrors,

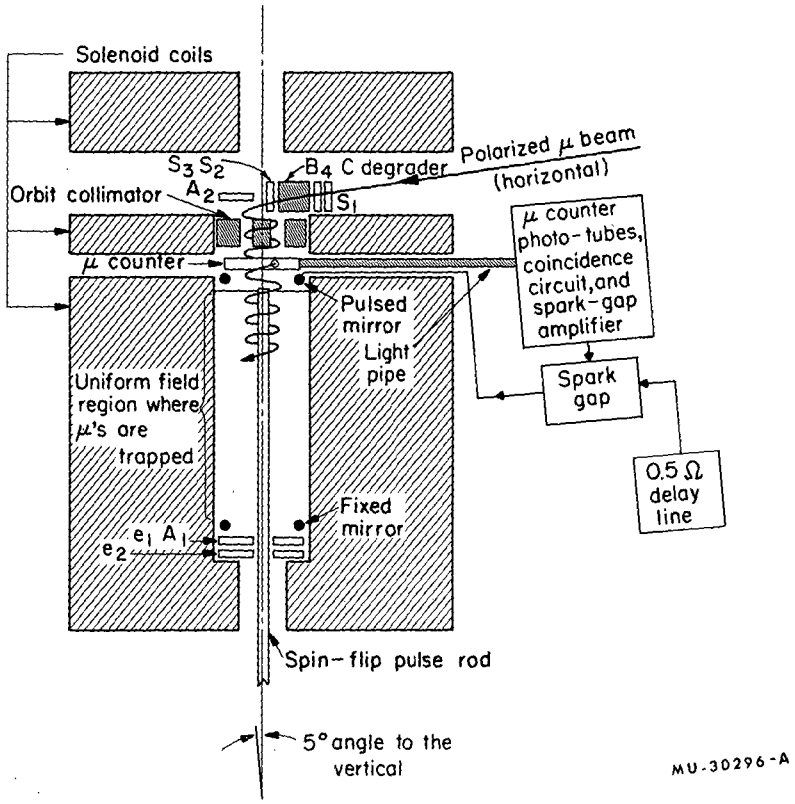

Fig. 1. Block diagram of $(g-2)_\mu$ apparatus.

one at each end of the uniform-field region. The bottom mirror is dc, but the upper mirror is pulsed and turned on only after the muon has entered the uniform-field region. One muon at a time is trapped in this way and inspected. The trapped muon, drifting slowly up and down between the two mirrors, moves essentially in the transverse plane of the solenoid field. Its orbit is a helix of shallow ($< 5°$) pitch angle.

The muon enters the uniform field with its spin $\underset{\sim}{\sigma}$ antiparallel to its velocity vector $\underset{\sim}{v}$ and, if g were exactly equal to 2, these two vectors would remain parallel "forever" in the magnetic field. But g does not equal 2 exactly and, as is discussed in detail in Sec. II, the spin vector precesses (ω_p) about 0.1% faster than the cyclotron frequency (ω_c). Consequently, the spin vector slowly drifts into the radial direction and on around to the parallel position, as shown in Fig. (2a). As described in Sec. II, the difference frequency $(\omega_p - \omega_c)$ is proportional to $(g-2)_\mu$. This experiment, then, consists of a measurement of the angle between the spin vector $\underset{\sim}{\sigma}$ and the velocity vector $\underset{\sim}{v}$ as a function of time.

The technique that we used to watch this angle utilizes the circumstance that one can determine the muon's spin direction by measuring the radiation pattern of electrons when the muon decays: $\mu \rightarrow e + \nu_1 + \nu_2$. The electron-distribution function from μ^+ decay is:

$$N(x,\theta)\, dx\, d\Omega = \frac{x^2}{2\pi} \left[(3-2x) + (2x-1)\cos\theta\right] dx\, d\Omega\,, \qquad (1)$$

where $N(x,\theta) \equiv$ the probability of one's observing an electron of energy x (in units of its maximum value $x_m = 2E/m_\mu$) come out at an angle θ with respect to the muon's spin vector in the rest frame of the muon. This pattern can be visualized in Fig. 3 for electrons with $x = 0.75$. In this experiment the muon is kept inside the trap until it decays and those decay electrons that escape through the bottom end of the solenoid are observed ($e_1 e_2$ coincidence in Fig. 1).

However, one more operation is required before the $\underset{\sim}{\sigma} \cdot \underset{\sim}{v}$ angle can be inferred from these escaping electrons. On Figs. 2(a) and 3, when one looks along the z axis, one always "sees" the $\underset{\sim}{\sigma}$ vector from its "side," regardless of the $\underset{\sim}{\sigma} \cdot \underset{\sim}{v}$ angle; thus no information on this angle is obtained. It is necessary to flip the spin vector $\underset{\sim}{\sigma}$ by means of a current pulse through a rod that runs along the solenoid axis (see Fig. 1). From Fig. 2(b) and the right-hand rule, it is seen that the B_θ field produced by this

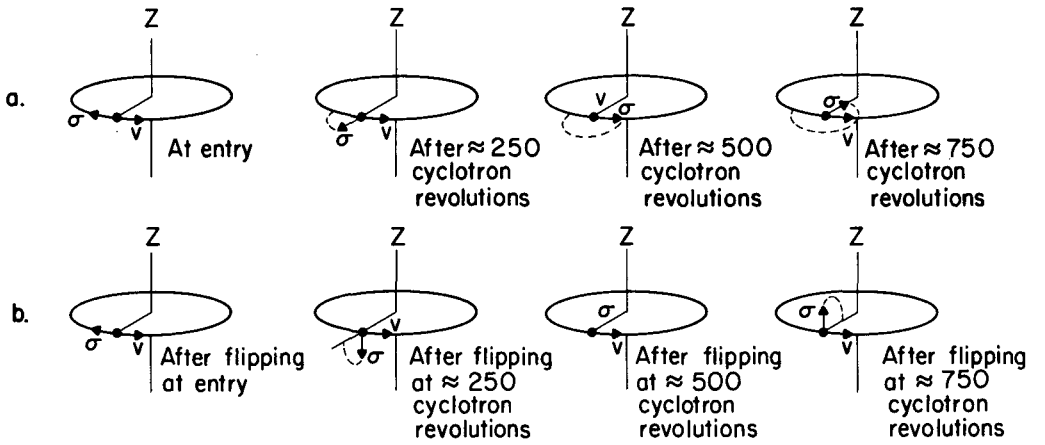

MU-30297

Fig. 2(a). Muon motion in a homogeneous magnetic field. The spin precesses about 0.1% faster then the velocity,
(b) Effect of spin-flip. The spin-flip pulse flips the radial component of the spin into the z direction; and leaves the azimuthal component unchanged.

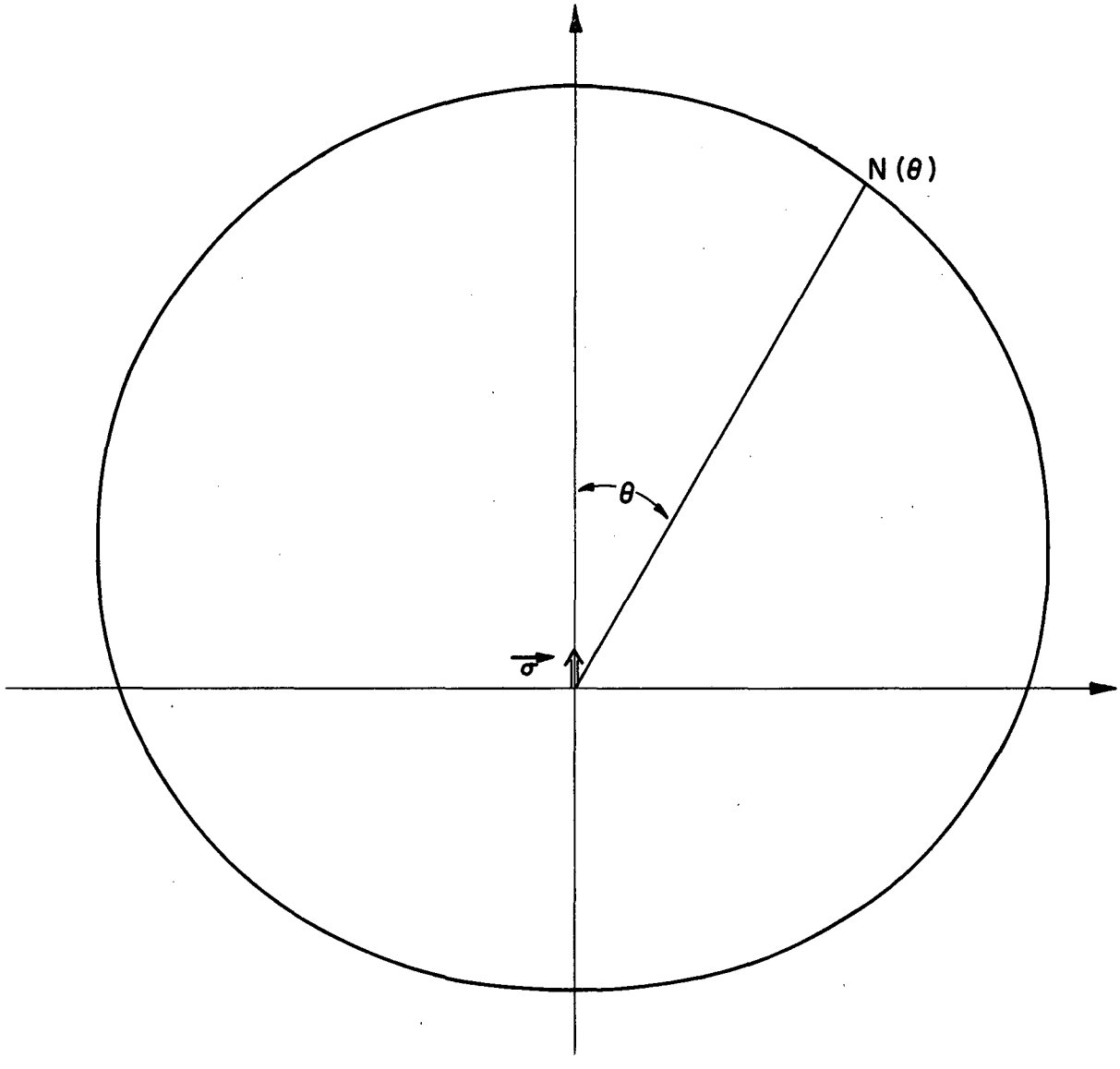

MUB-8648

Fig. 3. Muon decay pattern for an outgoing electron energy of 40 MeV.

current pulse has no effect on the spin if the pulse is applied when $\underset{\sim}{\sigma}$ is either parallel or antiparallel to $\underset{\sim}{v}$, and that the spin precesses around this pulsed B_θ field if the pulse is applied when $\underset{\sim}{\sigma}$ has a radial component. Indeed, in general, the radial component of $\underset{\sim}{\sigma}$ is flipped by the central-rod pulse, leaving the azimuthal component of $\underset{\sim}{\sigma}$ unchanged; by the proper choice of total charge in this pulse, the flip angle is made equal to 90°, i.e., the flip pulse effects the transformation

$$\begin{pmatrix} \sigma_r \\ \sigma_\theta \\ \sigma_z \end{pmatrix}' = \begin{pmatrix} 0 & 0 & 1 \\ 0 & 1 & 0 \\ -1 & 0 & 0 \end{pmatrix} \begin{pmatrix} \sigma_r \\ \sigma_\theta \\ \sigma_z \end{pmatrix} . \qquad (2)$$

After the flip, σ_z' remains constant as the muon drifts back and forth between the mirrors.

Finally electron counters $(e_1 e_2)$ are gated on only <u>after</u> the above-described flip pulse has been applied. Thus, they "see" an electron with a probability (σ_z') given by the radial component σ_r just <u>before</u> flipping. Figures 2 and 3 show that a maximum probability for detecting a decay electron occurs at a flip time corresponding to 250 cyclotron revolutions, a minimum probability at a flip time corresponding to 750 cyclotron revolutions, etc. If the muon decays before the flip pulse is applied, its electron does not come within the electron gate and cannot be counted. Therefore the probability of seeing the decay electron, as a function of <u>time of flip pulse</u> (not of time of decay), takes the form of a muon-decay curve with a superposed sinusoid (see Fig. 4). The frequency of this superposed sinusoid is $(\omega_c - \omega_p)$ and is proportional to $(g-2)_\mu$.

The overall experimental sequence of events leading to the final data (Fig. 4), can now be outlined. Refer again to Fig. 1, where a 150-MeV/c polarized muon beam enters the counter telescope $S_1 S_2 S_3$. The B_4C blocks between S_2 and S_3 degrade this momentum down to around 40 MeV/c. Muons around this lower, trappable momentum spiral through the collimator in the throat of the solenoid and pass through the μ-counter which is made of a strip of 0.010 inch thick plastic scintillator viewed by two photomultipliers. Only a small fraction of the initial beam passes through $S_1 S_2 S_3$ μ. A coincidence between the two μ-counter phototubes and S_3 (denoted

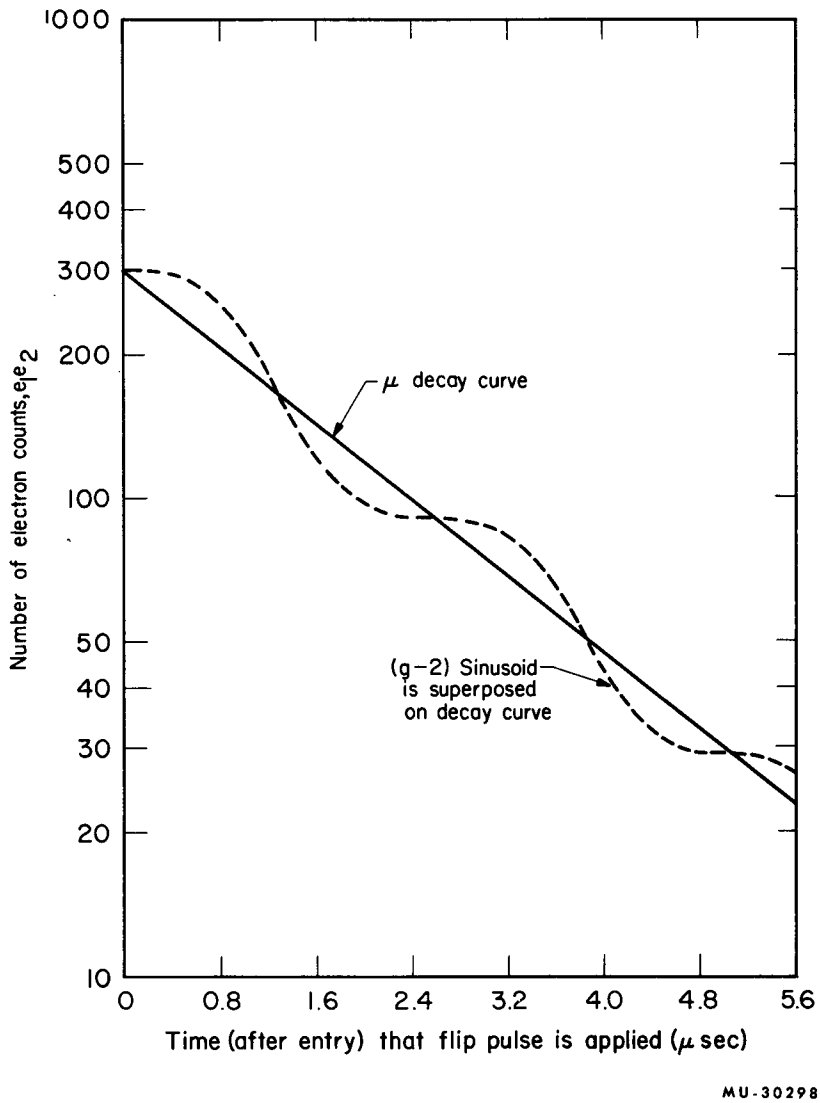

Fig. 4. Number of decay electrons from trapped muons vs the time at which the spin-flip pulse is applied.

hereafter by μ_T) is considered to indicate a trappable muon, defines time t = 0, and initiates the logic program. There are five basic parts in this logic program: First, the top (pulsed) mirror is turned on as rapidly as possible after the μ_T coincidence. Second, at a specific chosen time after μ_T, the spin-flip pulse is applied at any one of 64 discrete times from 0.7 to 7μsec after μ_T, in 0.1-μsec steps. Third, after the spin-flip pulse has been applied, the gate on $(e_1 e_2)$ is opened for a fixed (very long) interval to look for the decay electron. The electron count, if it comes, is stored in a pulse-height analyzer (PHA), each of whose 64 channels represents one particular flip-pulse time. Fourth, after the close of the $(e_1 e_2)$ gate, the logic is advanced one unit so that the next trapped muon will be flipped after precessing 0.1 μsec longer than the preceding one. This steppping procedure runs from 0.7 to 7μsec (as described above) and then starts again at the 0.7-μsec delay. Finally, if at any time after μ_T (t = 0) either of the muon anticounters $\bar{A}_1$ or $\bar{A}_2$ or the μ-counter itself "sees" a muon, the electron gate is closed--since this means that the muon was not trapped for the full precession interval, due to multiple scattering in μ, or some other cause.

Finally (as previously stated), the electron $(e_1 e_2)$ data in the PHA will form a curve as indicated by the dotted line in Fig. 4, and a calibrated time scale on the abscissa will give a measurement of $(g-2)_\mu$.

II. THEORY

A. The Anomalous Gyromagnetic Ratio of the Muon

The story of anomalous g-factors really begins with the discovery that the electron has spin. Classically, there is an intrinsic relation between the angular momentum of a charged particle (or charge distribution) and its magnetic moment. A charged particle moving in a circle has orbital angular momentum

$$L = mvr$$

where
$m \equiv$ particle mass
$v \equiv$ particle speed
$r \equiv$ particle orbit radius
$e \equiv$ particle charge,

and it creates a magnetic dipole field around the "current (i) loop" with moment

$$\mu = i\,(\pi r^2) = \frac{ve}{(2\pi r)}\,\pi r^2 = \frac{1}{2}\,evr. \tag{3}$$

Thus

$$\mu = \frac{eL}{2m}\ .$$

This relation between μ and L holds for charge distributions also, as long as $\rho_e \propto \rho_m$; that is, as long as the charge and mass densities have the same ratio throughout the distribution. Therefore it was expected in the early part of this century that for the electron,

$$\mu_{el} = \frac{eL}{2m} = \frac{e}{2m}\left(\frac{\hbar}{2}\right)\ .$$

That this could not be the case was discovered in the laboratory by observations of the anomalous Zeeman effect exhibited by many elements. Therefore, the formula was modified to

$$\mu_{el} = g\left[\frac{e}{2m}\left(\frac{\hbar}{2}\right)\right], \tag{4}$$

where g defines the gyromagnetic ratio, a dimensionless number. It was experimentally established that $g \approx 2$, and since the classical theory implied

that g should be unity, this g-factor was for a long time called the anomalous gyromagnetic ratio of the electron.

With the introduction of the Dirac equation in 1926, the situation changed sharply. By using the Dirac equation to find the electron energy eigenstates in a magnetic field, one finds that g is predicted to be exactly equal to 2. This triumph of the Dirac equation changed the g-factor of 2 from an anomaly to an "expected" result.

Quantum field theory changed the picture again (Refs. 1 to 9). The quantization of both the electromagnetic and the Dirac electron fields gives rise to vacuum fluctuations in the photon and electron populations. These fluctuations are analogous to the zero-point energy of the harmonic oscillator, and they interact with the particle described by the Dirac equation; but the interactions are in principle unobservable and have the net effect of changing the observed properties of the electron. Thus the Dirac equation is interpreted as giving the properties of the "bare" particle, without these interactions, whereas laboratory observed quantities necessarily include the interactions.

Any text on quantum electrodynamics discusses the calculation of anomalous g-factors. It is possible to give a brief verbal account of the physics involved without getting too involved in the computational details. The physics rests upon Dirac's[16] original quantum mechanical formulation of the theory of emission and absorption of photons by an electromagnetic system (since any interaction problem can be described in these terms), and upon the subsequent development of this theory in which the appearance of infinite quantities was overcome--to some extent. According to the rules of quantum mechanics, the amplitude (a_{fi}) for the transition of an electromagnetic system, from state i at time t = 0 to state f at time t = T, under the influence of a periodic perturbation potential $\Delta H = U(\underset{\sim}{x})e^{\pm i\omega t}$, is

$$a_{fi} = \int \psi_f^* \, \Delta H \, \psi_i \, d^4x \qquad (5)$$

$$= -\left(\frac{i}{\hbar}\right) \int_0^T \exp(i\omega_f t)\, U_{fi}\, \exp(\pm i\omega t)\, \exp(-i\omega_i t)\, dt,$$

where $\omega_j \equiv \frac{\text{energy of state } j}{\hbar}$

$U_{fi} \equiv$ time-independent matrix element connecting the two states.

Thus
$$a_{fi} = - \frac{\left[\exp i T (\omega_f - \omega - \omega_i)\right] - 1}{\hbar(\omega_f - \omega - \omega_i)} U_{fi} \quad . \tag{16}$$

And
$$\left| a_{fi} \right|^2 = \left| U_{fi} \right|^2 \frac{4 \sin^2 (\frac{T\Delta}{2\hbar})}{\Delta^2} \quad , \tag{7}$$

where

$$\Delta \equiv \hbar (\omega_f - \omega - \omega_i) \, .$$

For the emission and absorption of photons, the periodic potential is the vector potential describing the photon involved, and the wave function ψ is the solution of the appropriate wave equation for the matter involved. Aside from computational problems--such as the representation, the gauge, and c numbers vs q numbers--there are two points to be made regarding this transition amplitude. First, as $T \longrightarrow \infty$, the amplitude has a finite value only for $\omega = \omega_f - \omega_i$, that is, energy is conserved. Second, the amplitude has a finite value for small T for an arbitrary ω just so long as $T\Delta/2\hbar \lesssim 1$; this means that an electron can emit and absorb with finite amplitude the same photon within time interval T without conserving energy ($\omega_f = \omega_i$ but $\omega > 0$). In short, "inside the uncertainty principle" anything goes and all transitions are possible.

Such "virtual" effects contribute infinities to the detailed computation of any transition-matrix element. Some of these divergences are due only to mathematical problems and can be eliminated. Others, much more serious in character, are eliminated in two steps. In the first step the infinite parts are separated from the finite (observable) parts of the matrix elements. In the second step, <u>all</u> these infinite parts can be combined in a "natural" way with the two phenomenological constants m_0 and e_0. These divergences are then eliminated by a redefinition of mass and charge. [Although this technique is applicable to computations such as energy-level shifts in atoms and g-factor corrections, it is <u>not</u> applicable to the computation of a

number for the physical mass of the electron or the muon. And even where it does work, its beauty is not overwhelming. It is simply a tacked-on prescription that has been found to give finite numbers for some problems, numbers which, so far, agree with experimental values in an astonishing fashion.] It has been shown that this "renormalization" procedure can be consistently applied to all orders of the perturbation expansion, i.e., to the emission and absorption of any number of photons and pairs.

In particular, to order e^2, the relevant graphs are

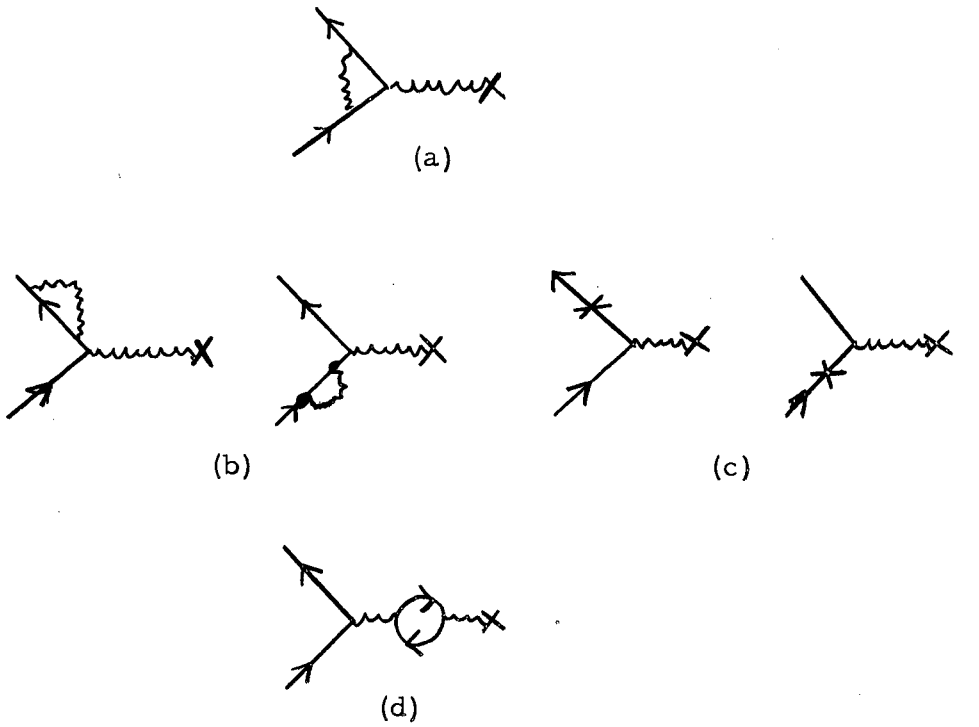

Evaluating these graphs for the electron (or muon) in a static external field (this experiment), one finds that (d), the vacuum polarization term, gives no contribution. Graphs (c), the mass renormalization terms, are infinite but cancel the leading divergence in graphs (b). The remaining part of (b), the self-energy terms, combine with (a), the vertex term, to give the finite result α/π.

By such techniques, the correction, to fourth order, to the Dirac g-factor of the electron and of the muon has been computed by several people (Refs. 1 to 9). For the electron, the computed result is

$$(g-2)_{el} = \left[\left(\frac{\alpha}{\pi}\right) - 0.656 \left(\frac{\alpha}{\pi}\right)^2 + \cdots \right]$$

$$= 2\left[0.0011596\right].$$

The best measurement to date (Refs. 17 to 21) gives $(g-2)_{el} = \frac{\alpha}{\pi} - (0.654 \pm 0.01)\left(\frac{\alpha}{\pi}\right)^2$. For the muon the computed result is

$$(g-2)_{\mu} = \left[\left(\frac{\alpha}{\pi}\right) + 1.50 \left(\frac{\alpha}{\pi}\right)^2 + \cdots \right]$$

$$= 2\left[0.0011654\right],$$

where α is the fine-structure constant $\approx 1/137$. The series converge rapidly since $\alpha/\pi \approx 1/500$.

The source of the difference between the muon and electron g-factors is easily described physically. The electron calculation is carried out as if the universe were populated only with electrons and photons; in particular, the vacuum fluctuations of all particles except the electron itself may be neglected, since all other particles are very much heavier than the electron. If a similar program is carried out in computing the muon g-factor (only muons and photons), the result is identical to that of the electron. In the case of the muon, however, not all other particles may be validly neglected; the much lighter electron, through its vacuum fluctuations, strongly affects the fourth-order perturbation calculation. Thus the difference in g-factors is not due to different theoretical techniques, but is due instead to the different places occupied by muon and electron in the elementary-particle mass spectrum.

The deviation of g from 2, predicted by quantum field theory, is now the quantity enjoying the name "anomalous gyromagnetic ratio" of the electron (or muon). It is this deviation, $(g-2)_{\mu}$, that is measured in this experiment.

B. Muon Motion in the Solenoid

Before discussing in detail the motion of the muon in the solenoid, we note that, as Bloch has pointed out (Ref. 22) the expectation value of the spin operator must necessarily have the same time dependence as one would obtain from the classical equations of motion. Since in this experiment only the expectation value of the muon spin is observed, a quantum-mechanical description of the spin is unnecessary. Similarly, a classical description of the muon position and velocity suffices, since the product $\Delta p \Delta q$ is many orders of magnitude larger than $\hbar$ in this experiment.

1. Nonrelativistic Motion

In first approximation, the muons in this experiment move non-relativistically through a homogeneous magnetic field. This simple case will be considered first, and the modifications due to special relativity, field gradients in the mirrors, and pulsed fields will be considered later.

The classical equations of motion for a charged particle with a magnetic dipole moment are

$$\frac{d\underset{\sim}{s}}{dt} = g/2 \quad \frac{e}{m} (\underset{\sim}{s} \times \underset{\sim}{B}) \tag{8}$$

and

$$\frac{d\underset{\sim}{v}}{dt} = \frac{e}{\underset{\sim}{m}} \quad (\underset{\sim}{v} \times \underset{\sim}{B}) \ , \tag{9}$$

where

e = electric charge (positive)

m = rest mass

$\underset{\sim}{s}$ = spin angular momentum

g = gyromagnetic ratio

$\underset{\sim}{B}$ = magnetic field

$\underset{\sim}{v}$ = velocity (constant in a pure B field)

ω_0 = cyclotron frequency = eB/m .

The solutions of these equations are most easily examined when they are expressed in cylindrical coordinates in which the z axis is the solenoid symmetry axis, $\underset{\sim}{r}$ is the radius vector from the z axis to the muon, and $\hat{\theta}$ is the direction orthogonal to $\hat{r}$ and $\hat{z}$ so that $\hat{r} \times \hat{\theta} = \hat{z}$ (a circumflex

indicates a unit vector). For the uniform-field case, (the simplest solution), the muon velocity (concentric orbit) is:

$$\begin{aligned} v_\theta &= - v \cos \epsilon \\ v_r &= 0 \\ v_z &= v \sin \epsilon \ . \end{aligned} \tag{10}$$

Thus the muon moves in a right circular helix of pitch angle ϵ . The solution for the spin equation in the same coordinate system is

$$\begin{aligned} s_\theta &= (s \cos \epsilon) \cos \omega_\Delta t \\ s_r &= (s \cos \epsilon) \sin \omega_\Delta t \\ s_z &= -(s \sin \epsilon) \ , \end{aligned} \tag{11}$$

where, at $t = 0$, $\underset{\sim}{s}$ and $\underset{\sim}{v}$ are antiparallel (true for a μ^+ coming from pion decay)

$$\omega_\Delta = (g/2-1)\ (eB/m) \ .$$

Since the velocity is described in this coordinate system with no explicit time dependence, the time dependence in the spin equations describes the spin motion with respect to the velocity. For example, if $g = 2$, the spin and velocity equations of motion become identical, and the explicit time dependence in the spin solutions disappears. This disappearance indicates that there is no time dependence in the relative spin and velocity orientation, and that if at $t = 0$, $\underset{\sim}{s}$ and $\underset{\sim}{v}$ are antiparallel, they remain so forever.

In fact, $(g/2-1) \approx 0.001$, so that $\omega_\Delta \approx 0.001 \times \omega_0$, and the muon spin slowly precesses with respect to the velocity. In the nonrelativistic approximation, the rate of spin precession and the cyclotron frequency of the muon are not functions of velocity. Thus a spread of muon energies in the solenoid has no "smearing" effect on the $(g-2)_\mu$ spin precession and, rather remarkably, this continues to hold true even in the relativistic region.

2. Effect of Mirrors

If the field were perfectly homogeneous, the muons would not be confined to a finite volume, but would continue to drift down the z axis in an infinite helix. Thus, some field deformation or perturbation is required to confine the muons to a finite region. The technique used (borrowed from plasma physics) was to increase B_z slightly for $|z| \geq 14$ inches. Although the general "magnetic mirror" problem is quite complicated, a

limiting case applicable to our situation is very simple. The first approximation we require is that B_z does not vary radially, and that the field is cylindrically symmetric. Then from $\nabla \cdot B = 0$, $\nabla \times B = 0$, we find

$$\begin{aligned} B_r &= -\frac{r}{2}\frac{\partial B_z}{\partial z} \\ B_\theta &= 0 \\ B_z &= B_z(z) . \end{aligned} \tag{12}$$

Second, we consider only the case where $0 \leq \epsilon \leq 0.1$ radian and where $(\partial B_z/\partial z)\, 2\pi r\epsilon << B_z$. In this case we can find a relation between the incremental "mirror" field and ϵ_{max}, the maximum helix pitch angle that can be reflected. The condition for reflection is clearly that $v_z \to 0$. Since

$$v d(\sin\theta) = \ddot{z}\Delta t = -\frac{e}{m} v_\theta B_r \Delta t = -\frac{r}{2}\frac{e}{m} v \cos\epsilon \frac{\partial B_z}{\partial z}\Delta t, \tag{13}$$

and since $r = \dfrac{mv}{eB_z}$

$$d(\sin\epsilon) = -\frac{\cos\epsilon}{2\sin\epsilon}\frac{dB_z}{B_z} ; \tag{14}$$

and since

$$\cos\epsilon \approx 1 \quad \text{for} \quad 0 \leq \epsilon \leq 0.1,$$

$$d(\sin^2\epsilon) = -\frac{dB_z}{B_z} . \tag{15}$$

Therefore, for reflection, we must have

$$\frac{\Delta B_z}{B_z} = \sin^2\epsilon_{max} , \tag{16}$$

for $\epsilon_{max} \approx 0.1$ radian, $\dfrac{\Delta B_z}{B_z} \approx 0.01$.

In this derivation several approximations were made; we ignored $\dfrac{dv_\theta}{dt} = \dfrac{e}{m} v_z B_r$, the variation of r as B_z increases, and nonconcentricities that could arise if the ΔB_z variation occurred over a distance $\leq 2\pi\epsilon r$. In fact, these small corrections are quite unimportant and are easily computed by perturbation methods. It is of course crucial that the muon spin not be depolarized by the magnetic mirrors. This question,

somewhat more complicated than the problem of orbits in the mirrors, is discussed in Ref. 23. The conclusion is that although passage of a muon through one mirror does introduce some change in the muon polarization relative to its passage through a uniform field, passage through the opposite mirror produces cancellation effects, and the average polarization change due to the mirrors vanishes when averaged over several reflections. Here the mirror at positive z has been considered. The same results apply to the negative z mirror. A convenient approximate model of the solenoid magnetic mirrors is obtained by taking $\partial B_z/\partial z = \text{const}$, so that $\left(\frac{\partial B_z}{\partial z}\right) 4 \text{ in.} \approx 0.01\, B_z$.

3. Observation of the Muon-Spin Direction

As pointed out in Sec. I, no information about the muon-spin direction in the r,θ plane can be obtained by observing the electrons emitted along the z axis. Yet it is in the r,θ plane that the characteristic $(g-2)_\mu$ motion occurs. A way around this problem is offered by the "spin-flip" pulse discussed in the Introduction, which as a first approximation may be considered to convert S_r into S_z (and vice versa) at a chosen time. A current down the z axis produces an azimuthal (B_θ) field, which clearly has the desired effect, if the field strength and duration of the pulse are properly adjusted. Thus, for a 90° "flip",

$$\frac{\pi}{2} = \int \omega_s \, dt = \left[\frac{\mu_0 \epsilon (g/2)}{2\pi\, rm}\right] \int i \, dt = \left[\frac{\mu_0 \epsilon (g/2)}{2\pi\, rm}\right] Q , \qquad (17)$$

and it seems that the proper spin flip can be obtained simply by passing the correct charge down the z axis, regardless of the pulse length. Actually, this is not quite the whole story. The pulse should be long compared to the muon's period of revolution so that nonconcentric orbits "see" a B_θ that is averaged over their orbits. Otherwise, the spin is flipped too far (if the muon is close to the z axis) or not far enough (if the muon is far from the z axis). In Appendix D we show that if the flip pulse is long enough (adiabatic with respect to the cyclotron motion), the noncentric muons are flipped the same amount as the concentric ones.

At the same time, the flip pulse should be short compared to the $(g-2)_\mu$ precession period; otherwise it is impossible to flip any spin

component in the r, θ plane into the z direction. The situation is analogous to an electron resonance experiment where the spin cannot be flipped over if the rf field is too weak. For a pulse that is square in time, we must have $B_{flip} \geq B_z[1 - (2/g)]$ in order to achieve a 90° spin flip. The component of S in the r, θ plane that is flipped by the spin-flip pulse into the z direction depends on the value of B_{flip}. This is illustrated in Table II. Thus we see that it is in fact S_r that is flipped into the z direction only if $B_{flip} \to \infty$. The exact linear combination of S_r and S_θ that is flipped into the z direction is dependent on the shape of the flip pulse in time. The combination used in this experiment is described in Sec. III. D. The combination of S_r and S_θ that is actually flipped into the z direction is irrelevant as long as it is identical for every flip pulse (i. e., as long as the flip pulse has the same shape and magnitude every time, as is the case here).

Table II. Effect of magnitude of B_{flip} on which component of $\underset{\sim}{S}_\perp$ is flipped.

Magnitude of B_{flip}	Component of $\underset{\sim}{S}_\perp$ which is flipped
$B_{flip} \to \infty$	$\underset{\sim}{S}_r$
$B_{flip} \to \frac{2}{g}(g/2-1)B_0$	$\underset{\sim}{S}_\theta$

4. Relativistic Motion

There are several ways of obtaining the classical relativistic equations of motion for a particle with charge, spin, and magnetic moment. The simplest one is to write the equations of motion for the particle in its rest frame in a covariant way (Ref. 24). Then this covariant formulation gives the unique extension to other Lorentz frames.

Since we are interested in the spin of the particle, we must find some covariant generalization of the spin in the particle's rest frame. The relativistic generalization of a three-component axial vector (e. g., angular momentum) is a rank-two tensor, and spin motion may be discussed in terms of this tensor. A somewhat simpler scheme is used by Bargmann et al. (Ref. 25). They defined a polarization four-vector as:

$S = (S^0, \underset{\sim}{S})$. In the particle's rest frame (R), $S = (0, \underset{\sim}{S})$.

Therefore, in all frames $S \cdot U = 0$,* where U = four velocity. For a particle of rest mass m, charge e, and gyromagnetic ratio g,

$$\frac{dS}{d\tau} = \left(\frac{ge}{2m}\right) [F \cdot S + (S \cdot F \cdot U) U] - \left(\frac{dU}{d\tau} \cdot S\right) U . \qquad (18)$$

In homogeneous fields one also has

$$\frac{dU}{d\tau} = \left(\frac{e}{m}\right) F \cdot U . \qquad (19)$$

Therefore, for homogeneous fields,

$$\frac{dS}{d\tau} = \frac{e}{m} [g/2 \; F \cdot S + (g/2-1) (S \cdot F \cdot U) U] . \qquad (20)$$

Solution of the two last equations yields the result that for circular motion perpendicular to a pure $\underset{\sim}{B}$ field (both with respect to the laboratory frame), the g-2 frequency $\omega_\Delta = [(g/2)-1] \; eB/m = (g/2-1) \; \omega_0$, where ω_0 is the zero-energy cyclotron frequency. This most remarkable

* We follow the conventions of Bargmann et al., namely: $c = \hbar = 1$, coordinate four-vector of components $x^0 = t$, x^1, x^2, x^3: $x = (x^0, \underset{\sim}{x})$. The symbol τ is proper time; a dot between symbols means contraction of neighboring indices with the metric tensor (e.g., $x \cdot x = (x^0)^2 - \underset{\sim}{x}^2$), metric tensor

$$\ldots \quad g_{\alpha\beta} = \begin{bmatrix} 1 & 0 & 0 & 0 \\ 0 & -1 & 0 & 0 \\ 0 & 0 & -1 & 0 \\ 0 & 0 & 0 & -1 \end{bmatrix} \quad , \text{ and } \quad F^{\alpha\beta} = \begin{bmatrix} 0 & -E_1 & -E_2 & -E_3 \\ E_1 & 0 & -B_3 & B_2 \\ E_2 & B_3 & 0 & -B_1 \\ E_3 & -B_2 & B_1 & 0 \end{bmatrix} .$$

result shows that for the conditions assumed, ω_Δ is not a function of the particle velocity. Thus, in the extreme relativistic region, the spin could make many rotations in each complete cyclotron revolution.

Although the above result is completely valid, the underlying physics is somewhat obscured, perhaps, by the covariant formulation adopted. For our simple case in which only a constant homogeneous magnetic field is present, $B = B_z$, we can achieve the above result by another method. We examine the case where the particle motion is confined to the transverse (X-Y) plane. The orbital motion is circular, of course, with an angular frequency $\omega = \omega_0/\gamma$, where $\gamma = (1 - v^2/c^2)^{-1/2}$. To examine the motion of the spin of the particle, we make a Lorentz transformation to the particle's rest frame (R), expressing quantities in (R) as primed quantities and taking $\underset{\sim}{\beta}$ as the particle's velocity in the lab system. Since $\underset{\sim}{B} \perp \underset{\sim}{\beta}$, $\underset{\sim}{B}' = B'_z = \gamma B_z$, and the spin precesses at an angular frequency $\omega'_s = g/2\ \gamma\omega_0$. Because of time dilation, then, we are tempted to write for the spin precession frequency in the lab system $\omega_s = (g/2)\omega_0$; this is, however, incorrect because we have not allowed for Thomas precession of the spin (due to the circular motion of the particle), which would be present even in the absence of any dynamic interaction affecting the spin (Thomas precession is a purely kinematic effect). The Thomas precession is given by (Ref. 26),

$$\Omega_{\text{Thomas}} = \omega\ (1-\gamma)\ , \tag{21}$$

where ω is the orbital angular frequency as above. Thus we have

$$\begin{aligned} \omega_s &= (g/2)\ \omega_0 + \Omega_{\text{Thomas}} \\ &= (g/2)\ \omega_0 + (\omega_0/\gamma)\ (1 - \gamma) \\ &= [\ (g/2) - 1]\ \omega_0 + \omega_0/\gamma \end{aligned} \tag{22}$$

And, clearly, $\omega_\Delta = \omega_s - \omega = [\ (g/2) - 1]\ \omega_0$, which is identical to the result of Bargmann et al.

The complete independence of ω_Δ from γ is, however, at least partly a "coincidence." For helical motion, where there is a velocity component parallel to the magnetic field, there is a γ dependence. The exact form of the dependence depends on exactly how ω_Δ is defined. Fortunately the effects are small for the experimental conditions here. In Ref. 21, for example, the correction is quoted:

$$\frac{\omega_\Delta}{\omega_0} = (g/2-1)\left(1 - \frac{\gamma}{1+\gamma}\left\langle \beta_z^2 \right\rangle\right) . \tag{23}$$

Or, for the experimental conditions here, with the maximum β_z of all orbits used,

$$\frac{\omega_\Delta}{\omega_0} = (g/2-1)\,(1 - 0.0005) , \tag{24}$$

so that the correction is about 0.1% at most.

5. Injection and Trapping

A very critical part of the experimental design was the entrance region of the solenoid. In this region the muons, incident at ≈ 150 MeV/c, must be slowed to ≈ 30 to 50 MeV/c, with the velocity direction chosen to maximize the number entering the solenoid at acceptable pitch angles. The shape and strength of the magnetic field in the injection region play a crucial role.

The absolute value of the magnetic field in the entrance region was chosen first. A value substantially lower than that of the solenoid field would lead to a very small acceptance solid angle for the entering muons, as shown in Ref. 27. If the field in the entrance region is too high ($B_{ent.} \geq B_{solenoid}$), those muons which would have acceptable helix pitch angles in the solenoid would not be able to "clear" various obstructions in the entrance region (see Figs. 5 and 6), because their pitch angles in the entrance region would be too small. The optimum value of $B_{ent.} = 0.98\, B_{sol}$ was chosen on the basis of numerical and graphical calculation. Since the solenoid-coil geometry was fixed by other considerations, little could be done to change the field shape.

Once the entrance field was chosen, the optimum helix pitch angle for the degraded muons was fixed by Eq. (15), as well as the acceptable spread in angle. The pitch angle, in conjunction with the orbits of the 150-MeV/c muons in the fringe field, fixed the angle of solenoid tilt from the vertical. The small size of the allowable spread in helix angles ($\approx 2°$) indicated that multiple scattering in the muon degrader would cause a loss of useful muons. Accordingly, the major part of this degrading was done in boron carbide (B_4C), which appeared to be the best compromise between low Z (≈ 5) and high density (2.5 g/cc).

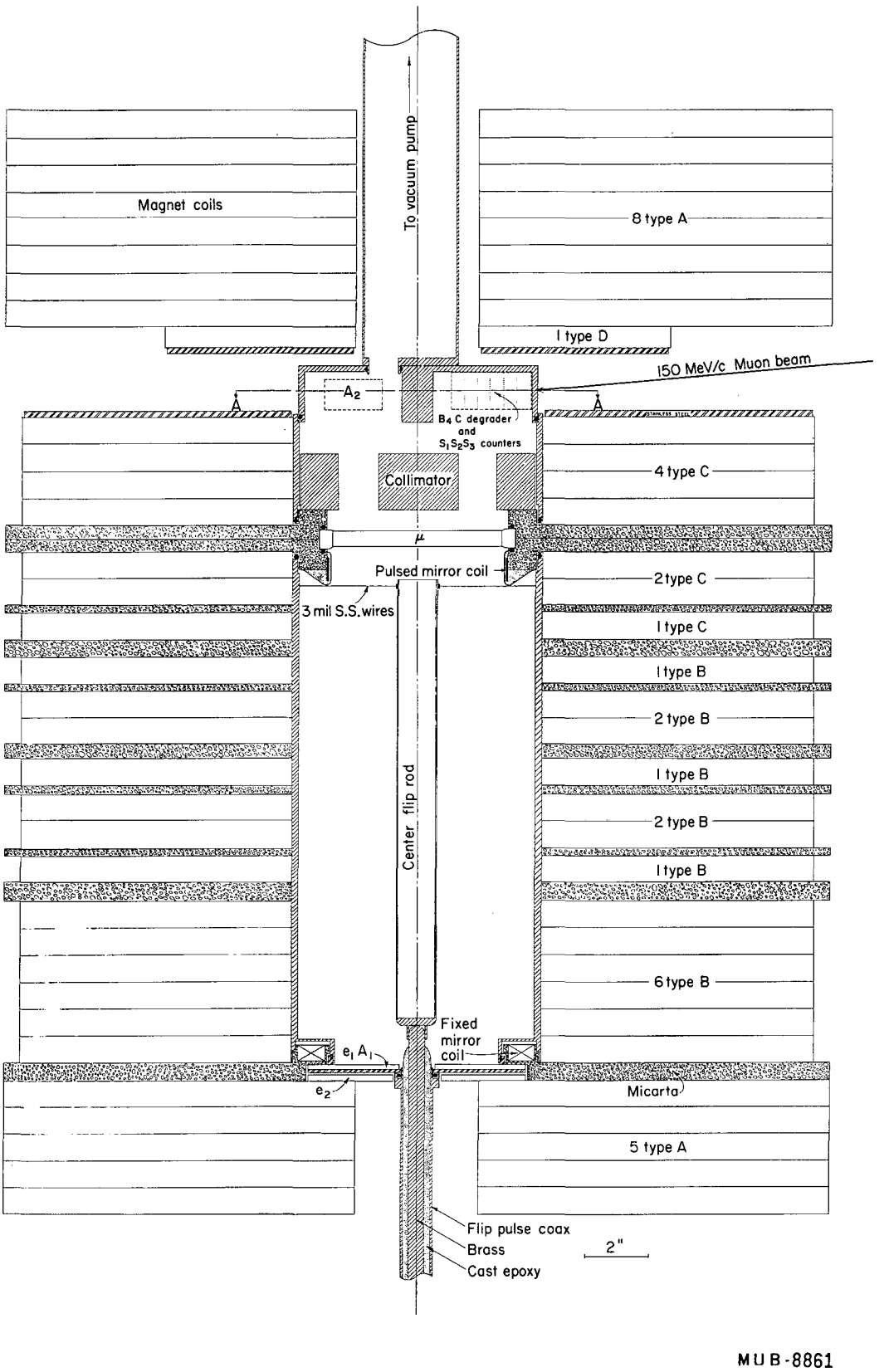

Fig. 5. Scale drawing of axial section of (g-2) apparatus showing magnet coils with micarta separators, vacuum chamber, counters, mirror coils, center flip rod, and collimator.

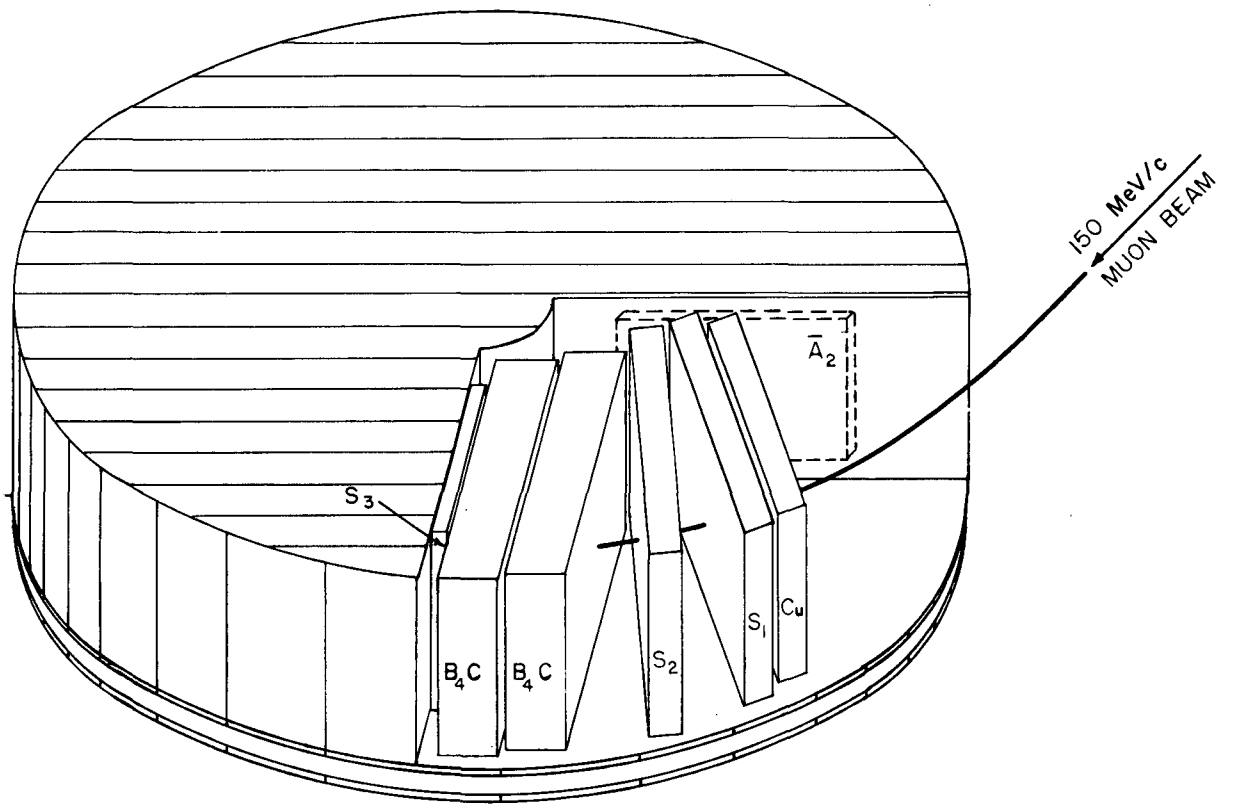

MUB-8774

Fig. 6. Lid of vacuum chamber showing three degraders (B, C and Cu) and four counters (S_1, S_2, S_3, $\bar{A}_2$).

There were, after these choices, some 3 degrees of freedom remaining: the total amount of degrader, and the two radii of the cylindrical collimator in the solenoid throat. The degrader was chosen so as to put a maximum number of muons into the 30 to 50 MeV/c range inside the solenoid. There was considerable latitude in degrader thickness due to the initial momentum spread of the beam.

The choices of the inner and outer radii of the collimator were based on a graphical calculation. It was necessary to exclude muons of high momenta, as their large orbits and small scattering angle in the μ-counter would result in their stopping in the pulsed or static mirror coils (Fig. 5). At low momenta there was the danger of the muons stopping in the center brass rod inside the solenoid or in the μ-counter itself. All such events contribute background since they appear to be due to trappable muons but, in fact, are muons that have stopped in some solid material--after triggering the electronic logic circuitry (see Sec. III.F). The radii chosen were $r_{inner} = 1.3$ inch, $r_{outer} = 2.5$ inch.

During the trapping process itself the current change in the top mirror caused some concern. At this time

$$\frac{d\bar{\Phi}}{dt} \approx 30 \text{ kV} ,$$

where $\bar{\Phi}$ is the magnetic flux enclosed by a typical muon orbit, and this azimuthal E field could conceivably depolarize muons in the mirror region. The effects of this $\underset{\sim}{E}$ field were computed, with the conclusion that the depolarization is negligible. Even if a muon were in the mirror region during the entire current-rise time, the E field could change the angle between $\underset{\sim}{S}$ and $\underset{\sim}{V}$ by 5° at most.

III. EXPERIMENTAL APPARATUS

A. Meson Source

The muons injected into the solenoid arise from the decay of pions made by the external proton beam of the Lawrence Radiation Laboratory's 184-inch cyclotron. The usual convenient source of muons (i.e., pion decay in the vicinity of the target) was useless because such muons were unpolarized. Accordingly, an efficient beam-transport system was designed (Ref. 15) to collect a 7.5% $\Delta p/p$ from a 2-inch diameter source with a solid angle of 6.5 millisteradians. The system is shown in Fig. 7.

The system provided polarized muons in the following way: The input bending magnet was adjusted to send 135-MeV/c pions down the optic axis, and the output bending magnet was set to bend 150-MeV/c particles on the optic axis. This procedure selected the highly polarized muons from forward in-flight decay of the 135-MeV/c pions; it also eliminated nondecaying particles from the target, thus providing an uncontaminated beam of polarized positive muons. Details of muon flux and polarization are given in Secs. IV.A and VIII.A.

B. Aphrodite

1. Solenoid and Ancillary Equipment

The details of the finished magnet and enclosed ancillary gear are described in this section, and the magnet design and field measurements in Secs. III.B.2 and III.B.3. Sketches of the magnet are shown in Figs. 1 and 5. Figure 5 is a scaled drawing of the axial section of the magnet. The magnet consists of a stack of individual coil "pancakes"--one of them sketched in Fig. 8--the whole array forming an air-core solenoid with an inner cylindrical "working volume" approximately 22 inches long by 8 inches in diameter. Although three different types of coil pancakes were used, the construction technique of all pancakes was identical. Two strands of hollow, square copper tubing were covered with fiberglass sleeving (Bentley-Harris BH Special Treated F/G), wound as shown on a specially constructed form with a fiberglass sheet separator between the two layers, and then potted in a Teflon-coated mold in a high-temperature epoxy designed to operate with substantial strength at temperatures > 100°C. The faces of the potted coils were then ground flat and parallel to ±0.002 inch. In the final configuration, different types of these pancakes were used, with the charcteristics given

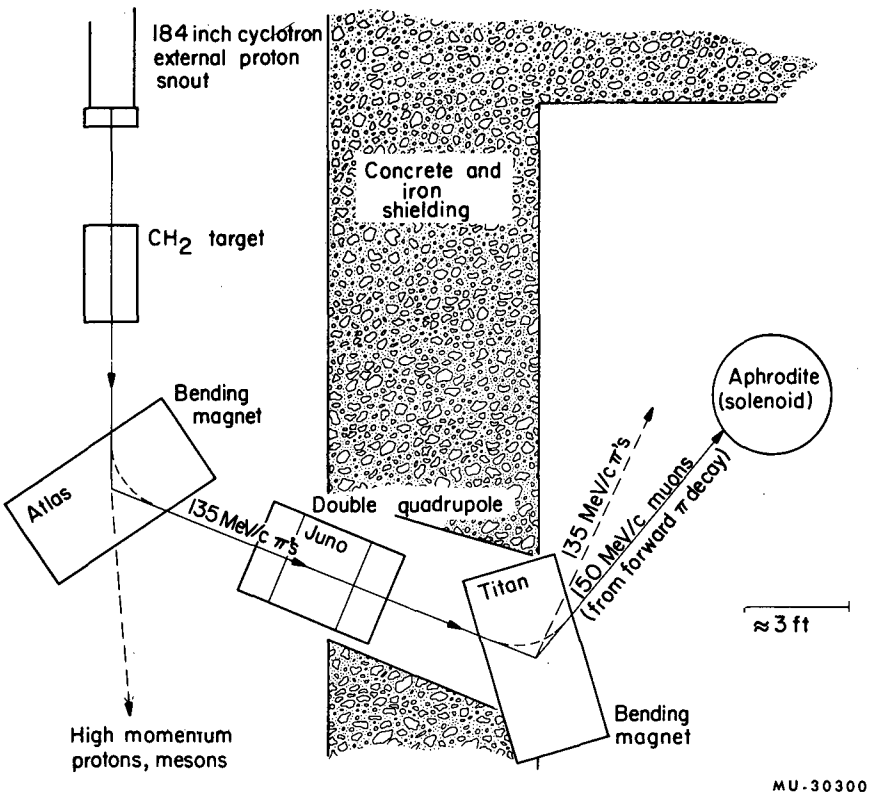

Fig. 7. π-μ Beam optics system.

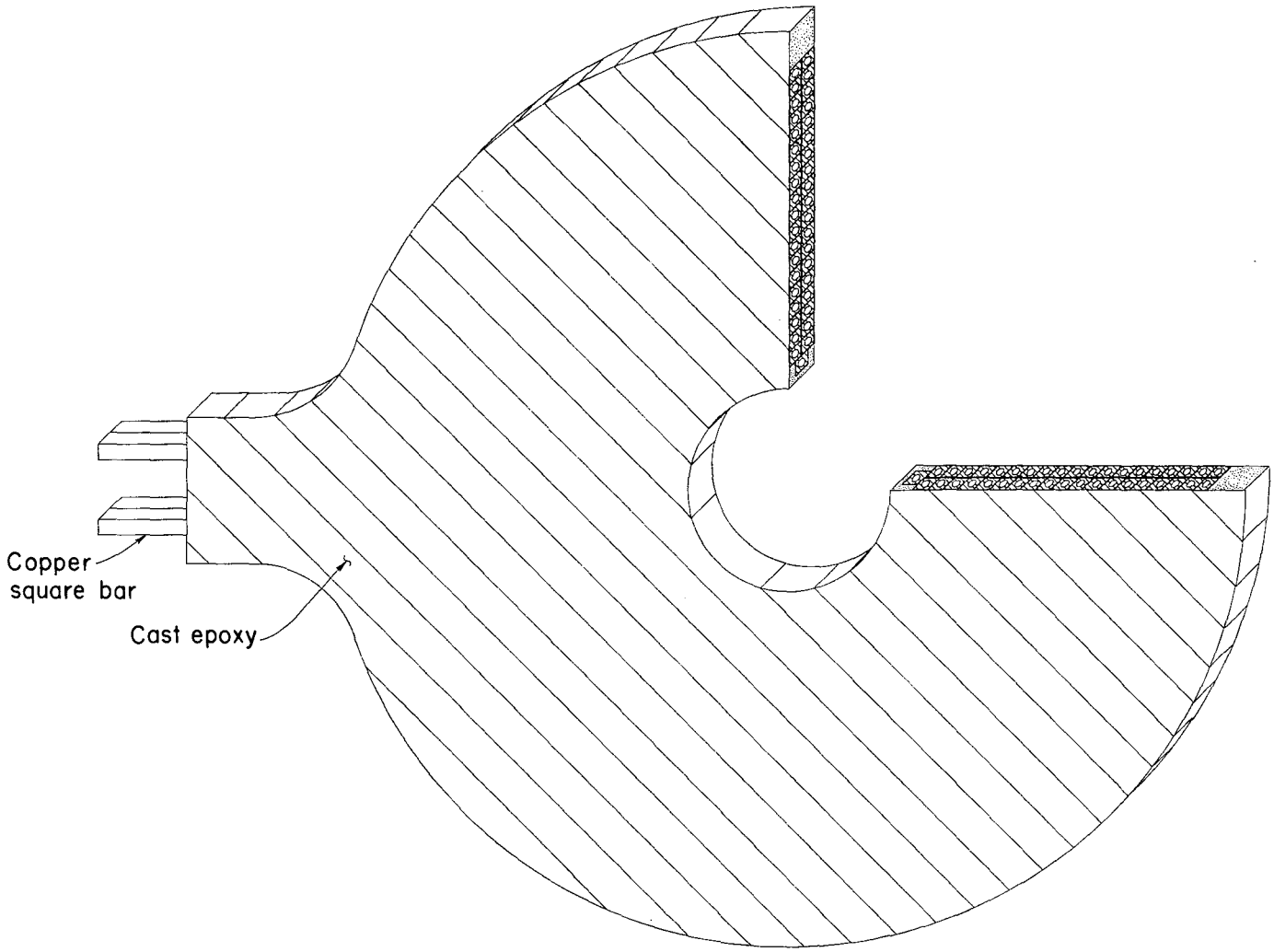

Fig. 8. Solenoid coil pancake.

in Table III. All pancakes were cooled with LC water with a 300-psi drop across each strand. The coils, arranged so that all the leads occupied a 90° azimuthal region, were all connected to a high-pressure manifold by means of rubber hose with Breco connectors. For the copper used in the coils, the resistivity was as given by the manufacturer-- $\rho_{20°C} = 1.71$ microhm cm. With this number, together with the empirical relation,

$$\text{water flow} = 1.81\, h_f^{\,.555}\, D^{2.695} \text{ liters/sec} \qquad (25)$$

where

$h_f \equiv$ pressure gradient in psi/mt.

$D \equiv$ hole diam in inches,

Table III is readily constructed.

Table III. Solenoid-coil data.

Coil	A 4 in. i.d. 26 in. o.d.	B 8 in. i.d. 26 in. o.d.	C 8 in. i.d. 26 in. o.d.	D 4 in. i.d. 16 in. o.d.
No. of coils used	13	13	7	1
Length of one strand (feet)	104	89	89	54
Water flow through one strand at 300 psi differential (gal/min)	1.7	1.9	1.9	1.2
Resistance of one strand (at final temp) (mΩ)	10.2	8.7	8.8	10.5
Wire size (in.^{2})	0.365	0.365	0.365	0.275
Water hole diam (in.)	0.220	0.220	0.220	0.170
Amperes flowing	1600	1600	1800	1300
Computed temperature rise (°C)	58	46	60	55

The average temperature rise $\langle \Delta T \rangle = \frac{\sum_i (\text{flow})_i (\Delta T)_i}{\text{total flow}}$ is thus estimated to be $\langle \Delta T \rangle = 96°\text{F}$ which, considering the fluctuations and uncertainties in hole diameters (strong dependence), agrees reasonably well with the measured value of 81°F. Table III shows that the total dc power consumed by the magnet is

$$P = \sum_i I_i^2 R_i = 1.7 \text{ MW}.$$

Since the highest possible magnetic field was desired, the individual pancakes were kept as close together as possible, consistent with the field-design requirements. The pancakes were stacked coaxially with the axis in a near-vertical orientation and separated either by 5-mil-thick Mylar disks or by Micarta disks. The main vacuum chamber and both mirror coils were built in as the stacking progressed. The whole stack was then clamped between two 1-inch. - thick stainless steel plates by means of three stainless steel bolts 1-1/4 in. in diameter and 4 feet long (see Fig. 9). The scale of the magnet can be judged by the 6-ft ladder shown in Fig. 9.

This basic, compact, high-field design philosophy dictated that all the other equipment, light pipes, mirror coils, vacuum apparatus and electronic leads had to be designed to slide into slots in the Micarta-disk separators, the thicknesses of which were determined previously by magnetic-field-shape requirements. In Fig. 5 the light pipes for the μ, $e_1\bar{A}_1$, e_2, and $\bar{A}_2$ counters come out perpendicular to the paper, as do the electrical leads to both the pulsed and dc mirror coils. In particular, all counter light pipes had to be at least 3 feet long in order that the phototubes could be located where the fringe magnetic field was small enough (about 2 kG) to allow magnetic shielding. Each shield consisted of a triple coaxial array of iron cylinders. The outer was 6 in. in diameter with a 5/8 in. wall; the middle was 3-1/2 in. in diameter with a 1/8 in. wall; and the third (mu metal) was of various sizes to fit each type of phototube. A drop in pulse height of about 10 to 20% from the phototubes was still observed with these shields when the magnet was turned on to full power, but since this main magnetic field was constant throughout the experiment, this drop was not troublesome. Altogether there were seven of these triple iron shields, and the resulting distortion of the fringe field in which they were located was severe (a factor-of-two change in the field at some points). However, the

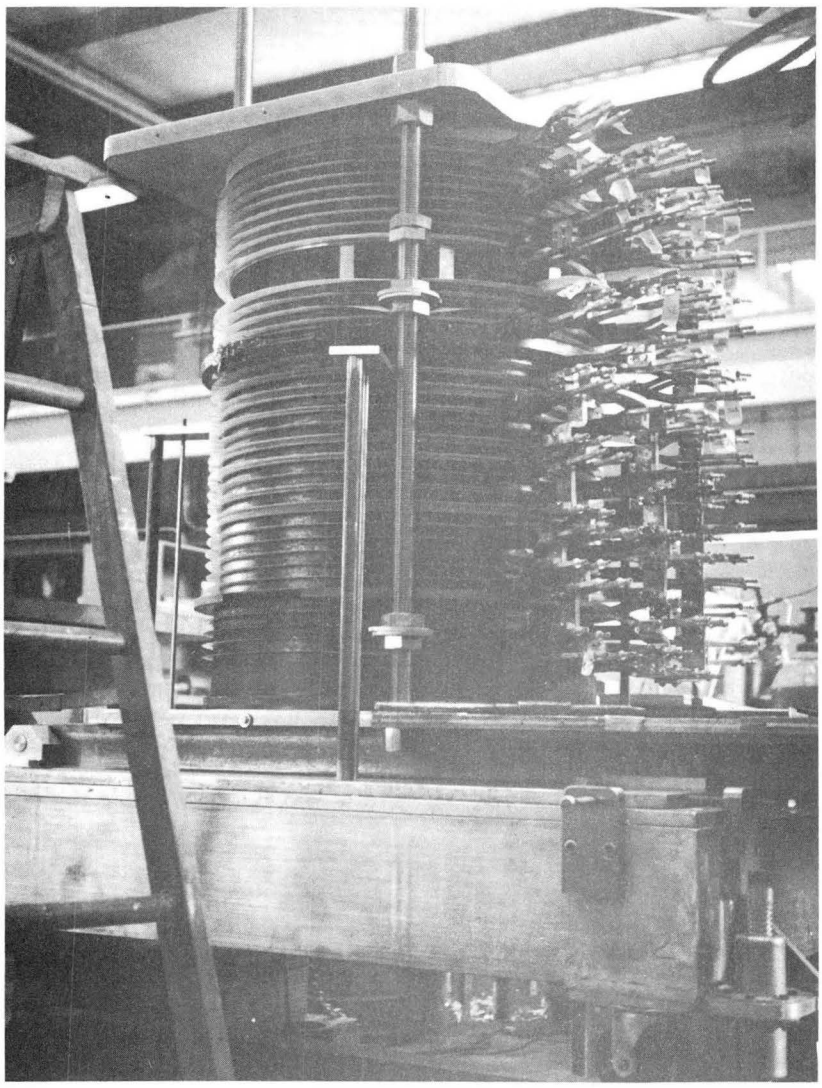

ZN-5294

Fig. 9. Photograph of assembled (g-2) solenoid.

overall effect on the field inside the solenoid, although noticeable, resulted in less than 0.1% measured change at any point and could be neglected.

The fixed mirror coil was wound with 1/8 in. refrigeration tubing, which was covered with fiberglass sleeving and then potted in epoxy in the bottom Micarta disk as shown in Fig. 5. A three-strand parallel winding ensured that the water flow was sufficient to run 500A through the coil. In practice the mirror carried 250A.

The pulsed mirror coil consisted of a single 6 in. - diameter turn of copper strap (1 in. wide by 40 mils thick) and can be seen in Fig. 5 just below the μ-counter. It was potted in epoxy fastened directly to a Micarta disk separator, which carried the two-strap high-voltage transmission line to the coil through a radial slot (not shown in Fig. 5).

The vacuum system proved to be one of the most troublesome parts of the apparatus. During the initial phase of the work, about 100-microns pressure was considered to be good enough, since the principal concern was in keeping the muon-residual gas scattering low enough to prevent muons from escaping the trap during their lifetime. Consequently fore-pump techniques were employed, together with Lucite and epoxy seals. During the experiment it became necessary to introduce anticounters into the vacuum to reduce background, and it was discovered that at the 50-micron pressure which a fore-pump would achieve, the pulsed mirror induced enough current and hence visible light in the residual gas to completely "wipe out" any scintillation counter which was optically exposed inside the "vacuum." Indeed, when peeking by eye through a Lucite window, one was greeted by a blinding flash from inside the "vacuum" every time the pulsed mirror was fired. This light was most undesirable since any muon counter and anticounter, to be efficient, had to have less than 0.05 gm/cm^2 between it and the vacuum because of the very small residual range of the trapped muons.

Two things were done. The vacuum system was cleaned up and the pumping speed was increased by opening up the pump-out line and installing an oil-diffusion pump. These improvements resulted in a best vacuum (magnet off and cold) of 0.03 micron and a normal operating vacuum (magnet hot) of about 1 micron. Although this helped considerably, it was insufficient to eliminate all light from the induced discharge, so covering of all counters inside the vacuum was necessary. It was possible to light-shield all counters

(see Sec. III.F) except the μ-counter, which was too close to the pulsed mirror. Consequently it was necessary to gate this counter off a few nanoseconds before the pulsed mirror came on, and this resulted in a somewhat reduced efficiency of this counter when it was used as an anticounter.

The current path for the spin-flip pulse presented a number of especially tricky mechanical, electrical, vacuum, and light pipe design problems. A 5-Ω coaxial line came in along the solenoid axis from the bottom and made a vacuum seal with the $e_1\overline{A}_1$ counter (see Fig. 5). The center conductor continued along the axis to a point just below the pulsed mirror, where it made electrical contact with the outer, brass vacuum can by running through a uniform array of 30 radial spokes made of 3-mil stainless steelwire. This wire was silver plated to reduce the resistance of the array to $\approx 0.1\Omega$. [The total thickness of stainless steel which a muon had to traverse when it entered the trap depends upon its helix pitch angle and the radius at which it traverses the array, but an average muon goes through about 7 mg. This is to be compared with its residual range of 150 mg/cm^2, its root-mean-square multiple-scattering angle in these wires of $\sqrt{\theta^2} \simeq 2°$, and its "outscattering" angle of $\simeq 4°$.] The spin-flip current-return path was down the brass wall of the vacuum can to a stainless steel ring which made contact with the $e_1\overline{A}_1$ counter (see Fig. 5). The current path continued through the binding screws of the $e_1\overline{A}_1$ counter to its stinless steel base plate, and finally to the outside sheath of the 5-Ω incoming coax line.

2. Solenoid Design

The solenoid was designed on the basis of several general considerations. Primarily, these include: (i) the muon lifetime vs $(\omega_p - \omega_c)$; (ii) total dc power available at the 184-inch cyclotron; (iii) the momentum distribution of polarized muons available at the cyclotron; (iv) the lower limit of usable muon momentum (due to scattering and degrading in the counters) and (v) the speed with which the pulsed mirror could be turned on. These, as well as a number of secondary factors, are discussed in this section. After the optimum overall dimensions of the solenoid were chosen, a computer was used[28] to determine the detailed pancake stacking configuration.

First, it can be shown that a substantial gain in accuracy can be achieved if at least one full $(g-2)_\mu$ revolution is seen during the measurement. Since the muon lifetime (τ) is 2μsec, a field of $B_{min.} = \frac{2\pi mc}{\tau e(g/2-1)} \approx 30$ kG is minimal, with the highest possible field providing the largest number of

$(g-2)_\mu$ revolutions in 2μsec and hence the best accuracy in the measurement, all other things being equal.

Next, there was a limited amount of magnet power available at the 184-inch cyclotron--aproximately 1.8 megawatts. In order to maximize the field, the computer varied several parameters while keeping the solenoid length and power input constant. The varying parameters included the inner and outer radii of the magnet. It was also necessary to vary the wire size and the water-hole diameter (Table III) simultaneously, because the voltage and current of the available power are both fixed and the permissible output temperature should be kept well below boiling. To be sure, the best choices of these parameters will change for a different solenoid length and, at the time the magnet was designed, it was not known just how fast the pulsed mirror could be closed nor what muon-momentum distribution could be achieved (thus determining the magnet length). Consequently some reasonable estimates were put into the initial solenoid design (see Ref. 10). In the final stages of the experiment, a 50% increase in the magnet length would have been welcome.

Next, it turns out that there is a rather sharp lower limit to the useable muon momentum (p_{min}). This limit is due basically to two factors. The first consists of multiple scattering and energy-loss problems in the basic logic counter, the μ-counter in Fig. 5. A minimum loss of ≈ 2 MeV in this counter is required if > 70% counting efficiency is desired. In Fig. 10 two quantities are plotted against the muon momentum at the front face of the μ-counter; (a) the muon momentum after traversing the μ-counter, and (b) the accompanying root-mean-square multiple-scattering angle in a plastic scintillation counter 0.025-in.thick. One cannot work very close to the "traversal threshold" of the μ-counter because of the large multiple scattering and the strong dependence of the outgoing momentum on counter thickness.

The second factor that determines the limiting momentum is shown in Fig. 11, where the momentum density of muons leaving the B_4C degraders is plotted vs outgoing momentum. Here the muon momentum density is a sharply rising function of the outgoing momentum. In this experiment the area under this curve from 0 to 50 MeV/c was equal to approximately 20% of the 150-MeV/c muons incident on the degraders.

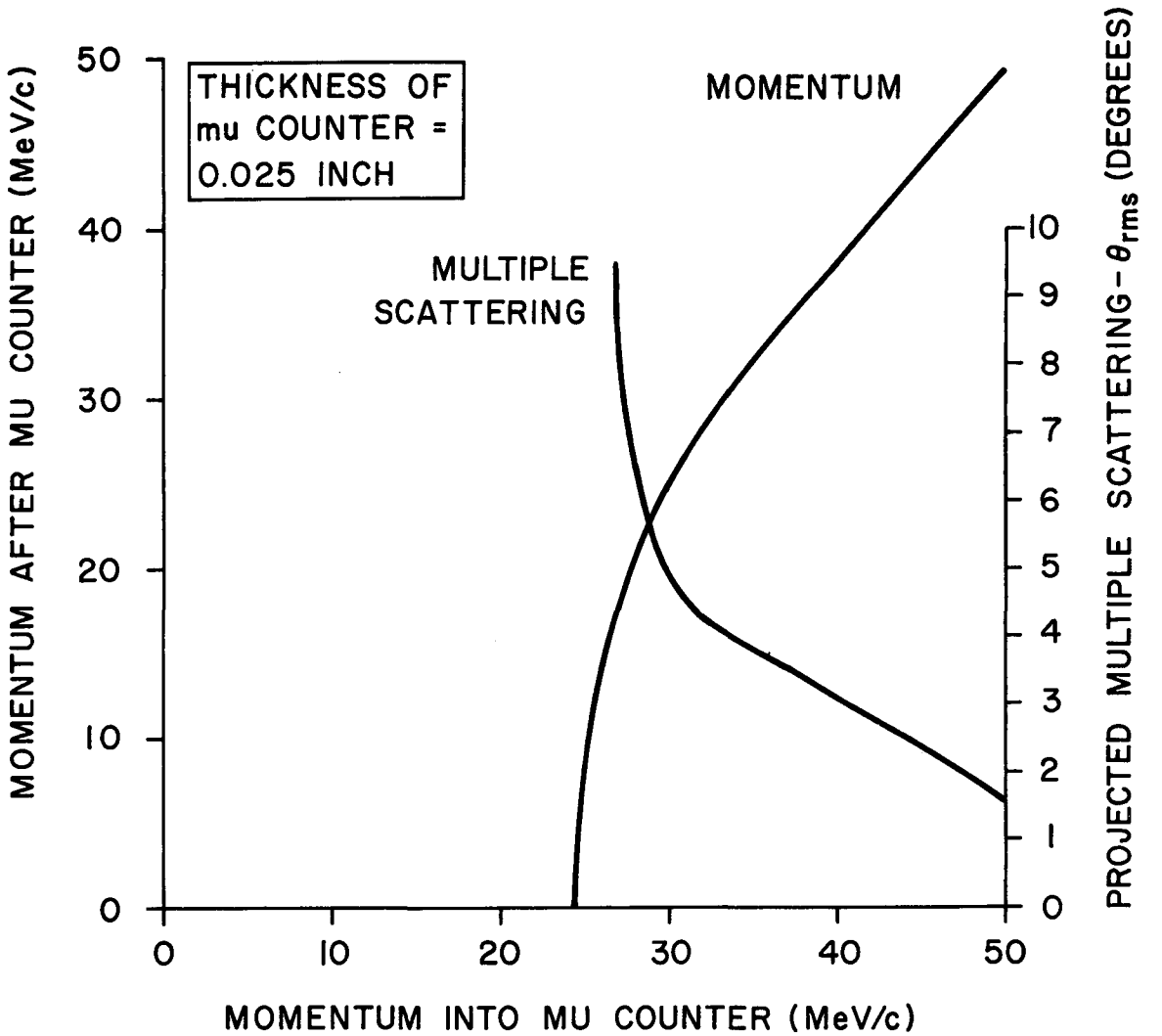

MUB-8649

Fig. 10. Muon-momentum loss and multiple-scattering angle in the μ-counter.

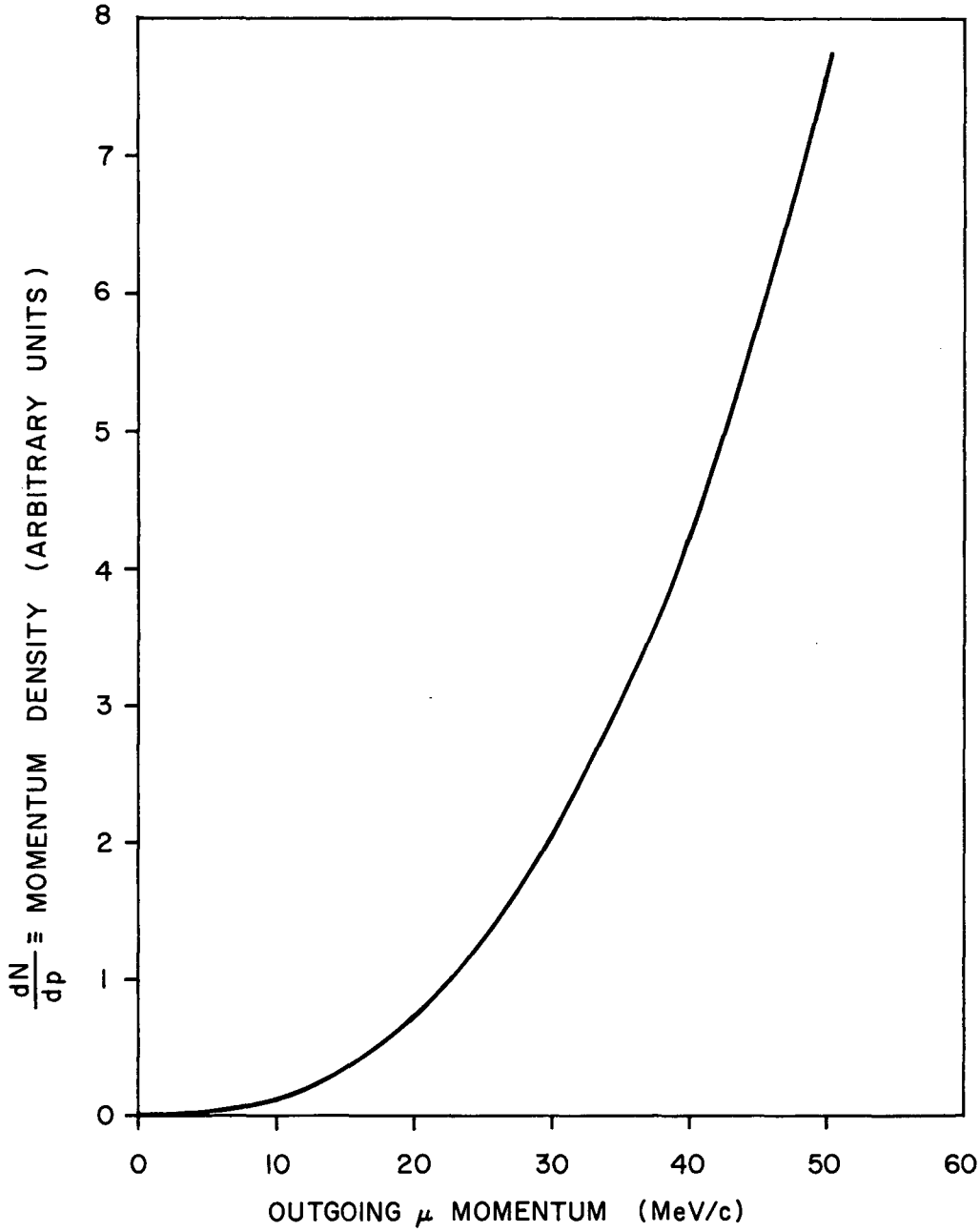

Fig. 11. Muon-momentum density at the downstream face of the B_4C degrader.

From these two figures the minimum useable momentum is seen to be $\geq$ 35 MeV/c. Therefore, the inside radius of the solenoid cannot be less than $\rho_{min} \approx p_{min}/B_{sol}$ (corresponding to no useable trapped muons) and should be as much larger than this number as possible.

In Fig. 12 is plotted the round-trip time vs pitch angle for three muon momenta. It was initially estimated that about 90 nsec would be required to close the pulsed mirror, and the final figure was 57 + 60 $\approx$ 120 nsec (Ref. 29). A longer solenoid would have made the closing of the pulsed mirror a much simpler problem, although, since the muon spends much of its time in the far end mirror, the gain in (round-trip time) vs (solenoid length) is discouragingly low.

The successful operation of the experiment depends upon the spin vector remaining in the transverse plane throughout the muon's lifetime in the trap. Any fields, electric or magnetic, which interact with the spin vector must be either eliminated or shown to have a negligible effect. For example, in the solenoid itself, the magnet pancakes are constructed so that the inner crossover windings represent an axial current flow. If the pancakes were stacked in a "regular" fashion--i.e., so that all crossover windings carried current in the same direction--and were all located at the same azimuthal position, then an axial current line of 3000 A would exist on the wall of the trapping region. The integrated effect of such a wall current on the θ spin component is zero, but the axial and radial spin components precess around this field. Although this axial spin component is small (because the helix pitch angles are small, and the radial component changes sign every cyclotron revolution), it is conceivable that a resonance could exist between the mirror bouncing precession, which does move the transverse component out of the transverse plane, and this "crossover" precession. Consequently, the pancakes were constructed and stacked with alternating axial crossover windings to eliminate any $\omega_{c.o.}$.

There is a rather narrow useful range for the ratio $R \equiv B_{injection}/B_{solenoid}$. As R decreases, the acceptance solid angle rapidly diminishes, whereas for R = 1, the acceptable muons do not clear the B_4C degrader. A range of $0.97 < R < 0.99$ can be considered useable. This determines the value of the solenoid field in the injection region, although between these two regions it is necessary only that the field be $< B_{sol.}$.

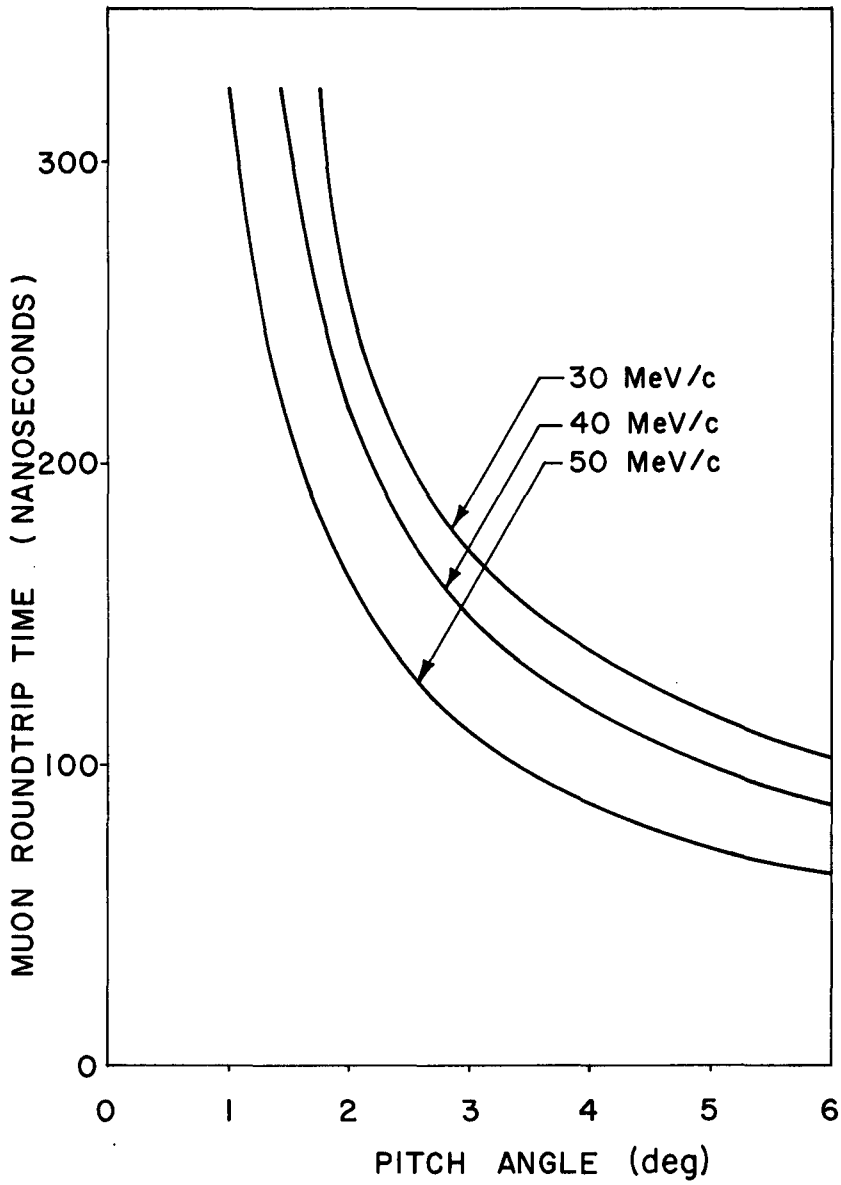

Fig. 12. Time required for muons leaving the μ-counter to spiral down the solenoid to the mirror at the far end, be reflected, and return to the μ-counter.

The uniformity of the solenoid field itself is determined by two factors. First, since it is B_{AVE} (over the history of the trapped muon before it is flipped) which enters into the formula for $(g-2)_\mu$, any fluctuations should not be too large compared to the desired accuracy-(although if the field is known everywhere a remarkably accurate value for B_{AVE} can be obtained even with fairly large "bumps"). For the actual operation of the experiment, a more stringent requirement on the field uniformity is due to the fact that those muons with pitch angles $\epsilon < B_{source}/B_{bump}$ will be reflected from the bump, and this, in turn, means less time available to close the pulsed mirror. In the final configuration better than 0.1% uniformity was achieved.

After the length, i.d., and o.d. were determined on the basis of these considerations, an individual pancake size was fixed. By trial and error we then obtained the required spacing between pancakes to give the desired field shape. That is, one would assume a spacing configuration, insert it into the computer program (Ref. 28), compute the axial field, then change the spacing configuration in a direction that, by guess, should smooth out the ripples, and put the new spacings into the computer program. With a little practice, 0.1% on-axis uniformity could be achieved in about 25 iterations.

The final spacing configuration is shown in Fig. 5.

3. Solenoid Field Measurements

The characteristics of the solenoid magnetic field dictated, to a large extent, the technique finally used for its measurement. The high degree of field homogeneity led to the adoption of a difference technique--i.e., the variations in magnetic field were measured from point to point, rather than the absolute value at each point. After this field mapping, the absolute value of the field at one reference point was measured.

The effect of "bumps" in the solenoid field on the muon orbits required rather accurate measurements of the field variations. The measurement technique (suggested by Joseph H. Dorst, head of the LRL Magnet Group) consisted in moving a coil from one point to another, and integrating (in time) the voltage output of the coil. The integrated voltage then is proportional to the magnetic-field difference between the two points, because the voltage developed in a coil by a changing magnetic field is given by

$$V = N \frac{d\bar{\Phi}}{dt} \quad , \tag{26}$$

where $\bar{\Phi}$ is the total magnetic flux linking the coil, N is the number of turns of the coil, and

$$\int V dt = N(\bar{\Phi}_2 - \bar{\Phi}_1) = NA\,(\bar{B}_2 - \bar{B}_1) \quad , \tag{27}$$

where A is the geometric area of the coil and B_1 (B_2) is the average magnetic field over the coil area at point 1 (2). An effective area may be defined for a coil as $A' = NA$. In this terminology the probe coil used had an effective area of 1363 cm^2, although its physical dimensions were only $\approx$ 1 cm o. d. and $\approx$ 1 cm in height.

When a coil with an accurately known area was available, the only remaining electrical problem was integration of the coil output voltage. The system used was essentially a Miller integrator; a schematic version of which is shown in Fig. 13. The operation of the integrator is best understood by at first ignoring the amplifier and imagining terminals a and b to be connected. Then we have a simple RC integrator with a time constant (τ) equal to RC. The voltage across the capacitor bears a linear relationship to the integrated probe-coil voltage as long as the time in moving the probe coil from point 1 to point 2 is much less than τ and much longer than L/R (L is inductance of the coil). Unfortunately, these conditions imply that the capacitor voltage V_{cap} will be small:

$$V_{cap} = A'\,(\bar{B}_2 - \bar{B}_1)\,\frac{t_2 - t_1}{\tau} \quad . \tag{28}$$

The Kintel amplifier offers a way around this problem. The amplifier works in such a way that points a and d are kept at the same potential, and no current flows from point d into the amplifier. Thus, from the viewpoint of the probe coil, the Miller integrator looks like an RC integrator with $C \to \infty$. The capacitor "sees" a current source of

$$i = \frac{A}{R}\,\frac{d}{dt}\,(\bar{B}) \quad , \tag{29}$$

so that in moving the coil from point 1 to point 2 the capacitor voltage becomes

$$V_{cap} = A'\,(\bar{B}_2 - \bar{B}_1)\,\frac{t_2 - t_1}{RC} \quad . \tag{30}$$

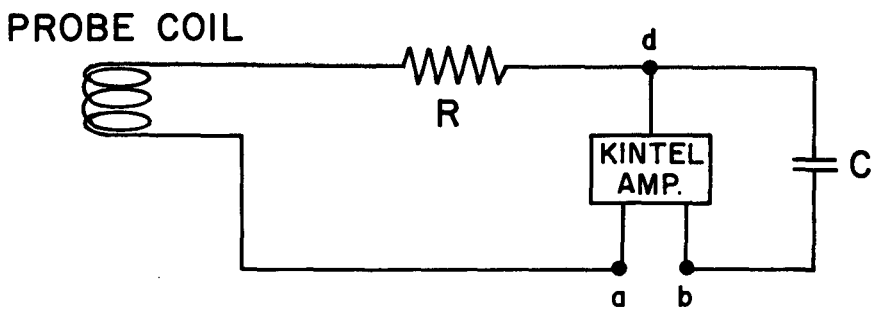

Fig. 13. Schematic of Miller integrator for measuring solenoid field.

This circuit appears similar to a simple RC integrator, but the important point is that $RC = \tau$ no longer needs to be much larger than the time in moving from point 1 to point 2. The condition on R still does hold, however: $R >> L/(t_2-t_1)$. By using the Miller integrator rather than a simple RC integrator, we were able to use RC = 0.001 sec rather than the $\approx$ 3000 sec otherwise necessary, thereby gaining a factor of 3×10^6 in capacitor voltage. Typically, a field change of 1 G gave a capacitor voltage of 10 mV. This voltage was monitored by a four-digit volt meter.

The system accuracy was limited chiefly by the capacitors used, which like all physical capacitors exhibited some leakage and "soakage" (change of capacity in time when a voltage is applied). In practice, it was possible to map the solenoid field to within ± 10 G with respect to a fixed reference point in about 30 seconds. Since the overall field was $\approx$ 28,000 gauss, this represents a relative accuracy of 3 to 4 parts in 10^4. The absolute measured field corresponded to the computed field to about 0.1%, and the relative agreement was excellent, that is the computed bumps were all found in the expected locations, with very nearly the expected magnitudes. The average solenoid field was found to be 28.2±0.2 kilogauss.

C. Pulsed Mirror System

It is essential to close the magnetic bottle as rapidly as possible after a muon has entered it. To see the strong dependence of the final counting rate on this mirror closing time (T_c), we must compute the number of muons entering the uniform-field region as a function of their round trip time T_r--i.e., the time needed by the muon after first passing through the μ-counter to spiral down to the bottom dc mirror, be reflected, and spiral back up to the upper-mirror position. This function $N(T_r)$ is actually a functional of the strength and time profile of the bottom mirror (due not only to less time spent by muons in a stronger mirror for any given momentum but also to muons of higher pitch angles being reflected by a stronger mirror), the thickness of B_4C degrader, the $S_3 \rightarrow \mu$ delay time, and the ratio $(B_{injection}/B_{solenoid}) \equiv R$, all of which affect the momentum distribution of muons entering the bottle. In Sec. IV. B and C, the procedures used to vary these parameters and to maximize the number of trapped mu's

$$N = \int_{T_c}^{\infty} \frac{dN(T_r)}{dT_r}\, dT_r \qquad (31)$$

are described. In this section, however, it suffices to show the essential dependence of N upon T_c.

For any given magnitude of momentum, assume that all pitch angles ϵ_i are equally populated by the muon orbits leaving the B_4C degrader. This assumption is valid here because the rms multiple-scattering angle of muons leaving the B_4C degrader is much larger than the range of useable pitch angles, and one is actually accepting trappable muons from near the maximum of the Gaussian scattering distribution. Upon leaving the B_4C degrader, the muon velocity vector makes an angle ϵ_i with the transverse plane and the muon is in a magnetic field B_i. As shown in Fig. 1, it spirals down through a region of weaker field and thence into the solenoid with a pitch angle ϵ_s. Since conditions of adiabaticity hold during this motion,

$$\sin^2\theta_i = \frac{B_i}{B_s} \sin^2\theta_s \,, \tag{32}$$

where θ is the angle between the momentum vector and the solenoid axis, θ_i is this angle in the injection plane, and θ_s is this angle in any plane inside the solenoid. But $\theta = (\pi/2) - \epsilon$, and $\epsilon << \pi/2$. Therefore,

$$1 - (\epsilon_i)^2 \approx \frac{B_i}{B_s} (1 - \epsilon_s^2)$$

$$= R (1 - \epsilon_s^2) \,. \tag{33}$$

The number of muons that are in the | momentum | interval between p and (p + dp) and that enter the uniform-field region (B_s) with pitch angles between 0° and ϵ_m is $\delta N(p)$:

$$\delta N(p) = \delta \int_0^{\epsilon} dN(p, \epsilon_s) = \delta \int_0^{\epsilon_m} \frac{\partial N}{\partial \epsilon_s} d\epsilon_s$$

$$= \delta \int_0^{\epsilon_m} \left(\frac{\partial N}{\partial \epsilon_i}\right) \left(\frac{\partial \epsilon_i}{\partial \epsilon_s}\right) d\epsilon_s \,. \tag{34}$$

Note that $\epsilon_{i(min)}$ maps into $\epsilon_{s(min)} = 0^\circ$, and that

$\epsilon_{i(max)}$ maps into $\epsilon_{s(max)} \equiv \epsilon_m$, according to formula (33).

With the foregoing assumption of uniform population of the ϵ_i angles, i.e., $\partial N/\partial \epsilon_i = K(p)$, Eq. (34) becomes

$$\delta N(p) = \delta \int_0^{\epsilon_m} K(p) \frac{R\epsilon_s d\epsilon_s}{\sqrt{(1-R) - R\epsilon_s^2}} = \delta K \left[\sqrt{1-R} - \sqrt{(1-R) - R\epsilon_m^2} \right] . \tag{35}$$

Under the entrance conditions (see Sec. II. B. 5), $(1-R) \approx 0.02 > R\epsilon_m^2 \simeq 0.005$, so that

$$\delta N(p) = \delta K \left[(1-R)^{1/2} + \frac{R\epsilon_m^2}{2(1-R)^{1/2}} + \cdots - (1-R)^{1/2} \right]$$

$$\approx \frac{R\epsilon_m^2 \delta K(p)}{2(1-R)^{1/2}} . \tag{36}$$

This relation holds for any given momentum. To complete the discussion, a final integration over the momentum distribution of the muons entering the solenoid must be done. Figure 11 shows that $\delta K/\delta p \approx p^{2.5}$ (there called dN/dp). Furthermore, for any given muon, the round-trip time is $T_r \approx \frac{2L}{V_{||}} = \frac{2Lm}{p \sin \epsilon_s} \approx \frac{2Lm}{p \epsilon_s}$ since all muons are quite nonrelativistic.

Thus $\epsilon_m = 2Lm/p\, T_c$. Consequently

$$\delta N(p) = \frac{p^{1/2} R 4 L^2 m^2 dp}{T_c^2 2 (1-R)^{1/2}} . \tag{37}$$

The limits on p are determined essentially by the inner and outer radii of the mechanical collimator and the strength of the solenoid field. The inner radius is fixed by the considerations given in Sec. III.C.2, and the outer radius is determined by the mechanical size of the solenoid ($\rho_{max}/\rho_{min} \approx 3$). Finally then, the number of trappable muons entering the solenoid is

$$N \approx \frac{K(\rho_{max})^{3/2}}{T_c^2} . \tag{38}$$

Upon closer inspection of the approximations made in Eq. (38), one finds a somewhat stronger dependence of N upon T_c. For example, those muons with small pitch angles are reflected by the bumps in the main solenoid and never make it to the mirror on the far end. A best final guess is that

$$N \approx \frac{1}{T_c^3} . \tag{39}$$

Thus, when the upper pulsed mirror was closed, every nanosecond was considered precious.

There are several general requirements that the pulsed mirror system had to meet and that, in effect, determined its circuitry and construction. First, since the load is a coil--i.e., a "pure" inductance--there is an inevitable rise time of the pulsed mirror current through it. To minimize this rise time, a minimum number of turns must be used in this coil (namely one), and then it must be operated at as high a pulsed voltage as practical. The final voltage choice--30 kV--was picked as much for engineering convenience as for physics reasons.

Second, since the load is essentially a pure inductance with a very small resistive component, it is not necessary to deliver all the load current at 30 kV. The desired current waveform is a square pulse with no ringing on the leading edge which, in turn, is as sharp as possible. The most economical way to achieve this waveform is to start the current moving from a HV source in order to achieve the short rise time, i.e., to deliver the μH^2 energy required to establish the mirror field; then, when the necessary current is flowing (5000 A), to switch over to a source that will continue to deliver the 5000 A for the required 15 μsec but at a power level that just compensates for the small resistive loss in the mirror coil. As it turned out, only 1500 V were required to maintain the 5000 A, once this current was established. This switching circuitry, centered around a crowbar spark gap, is shown as a block diagram in Fig. 14.

Third, the required current is determined by the largest pitch angle of muons that can be trapped, together with the momentum distribution. For example, if we (arbitrarily) decide to trap all muons whose orbits have solenoid pitch angles up to 6°, then the mirror current must form a magnetic field (B_{mir}) at the plane of the loop, which, when added to the steady-state field B_{sol} satisfies:

$$B_{sol} + B_{mir} = \frac{B_{sol}}{\sin^2 84°} , \tag{40}$$

i.e.,

$$\left(\frac{B_{mir}}{B_{sol}} \right)_{6°} = 0.011 .$$

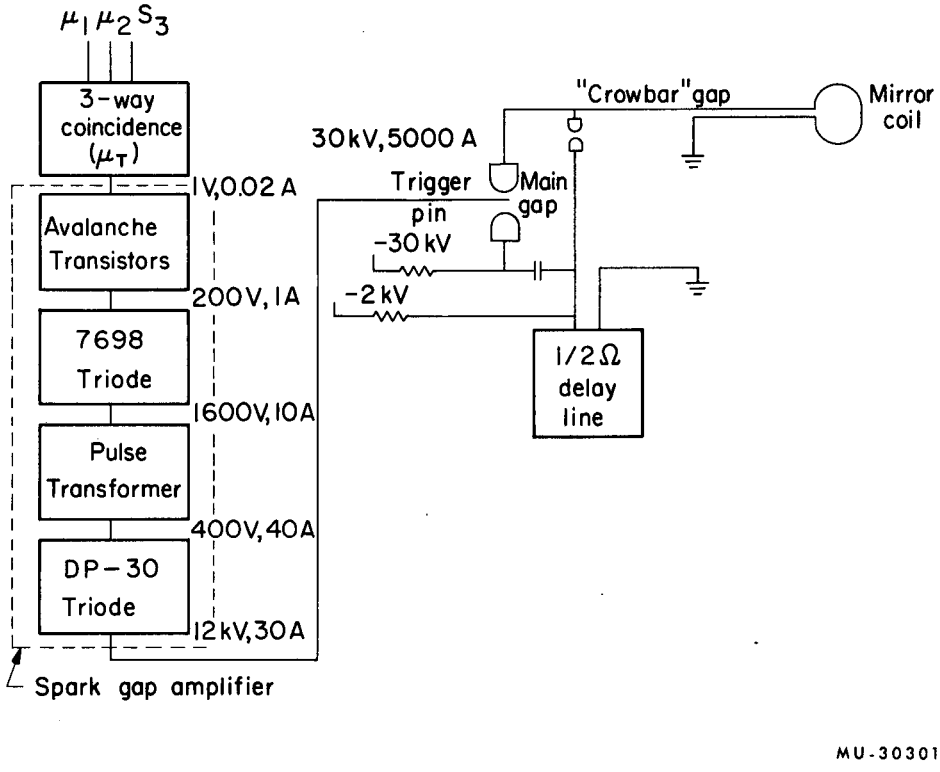

Fig. 14. Block diagram of pulsed-mirror electronics.

And this is valid for all momenta. However, a 50-MeV/c muon with 6° pitch has an axial speed of ≈ 1 cm/nsec, and therefore takes ≈ 60 nsec to make the round trip; this speed is to be compared with ≈ 170 nsec for a 50-MeV/c muon with 2° pitch angle. The essential point here is that the stronger the mirror the longer it must take to turn on; this is incompatible with the physics of the situation, which is that, for a given momentum, the muons that require a stronger mirror--i.e., those with large pitch angles--return most quickly to the door of the magnetic trap. One must therefore guess at the outset how fast a mirror can be constructed for a given mirror strength (current). After some initial experimentation, a mirror current of 5000 A was chosen.

Finally, an average muon rate of about 10/sec was expected. This figure determined how fast one had to recharge the circuitry after each event, as well as the average power dissipated.

With these general requirements as the boundary conditions, the pulsed mirror system was constructed. Block diagrams of the basic parts are shown in Figs. 14 and 15, detailed circuits are shown in Figs. 16, 17, and 18, and additional details are given in Ref. 29. A coincidence between S_3 and the μ-counter was the basic logic event that initiated the whole pulsed mirror system. The time at which the muon passed through the μ-counter scintillator defined t = 0. As described below, it took 57 nanoseconds from t = 0 to the start of the current rise in the mirror coil, and it took an additional 60 nanoseconds for the current to reach its final value (5000 A).

The S_3 and μ-counters were plastic scintillators on type 6199 phototubes. A tunnel-diode transistor-coincidence system on the anodes of these tubes fed an avalanche transistor pulser, which in turn drove a hard tube (12 kV at 20A) pulser. This 12 kV at 20A pulse triggered a 30-kV spark gap which switched into the mirror coil a HV condenser–low voltage charged delay line combination. In the description below, the t = 0 pulse is followed chronologically through the entire pulsed mirror system.

Because of the 30-kG field in which the S_3 and μ counter scintillators were located, it was necessary to transport the light from the plastic scintillators out through Lucite pipes 3-feet long (5 nsec) to a region where the phototubes could be magnetically shielded. (See Table IV). (A triple coaxial iron-cylinder shield reduced the residual field at the 6199's from ≈ 1 kG to less than 1 G.) It was necessary to keep the multiple

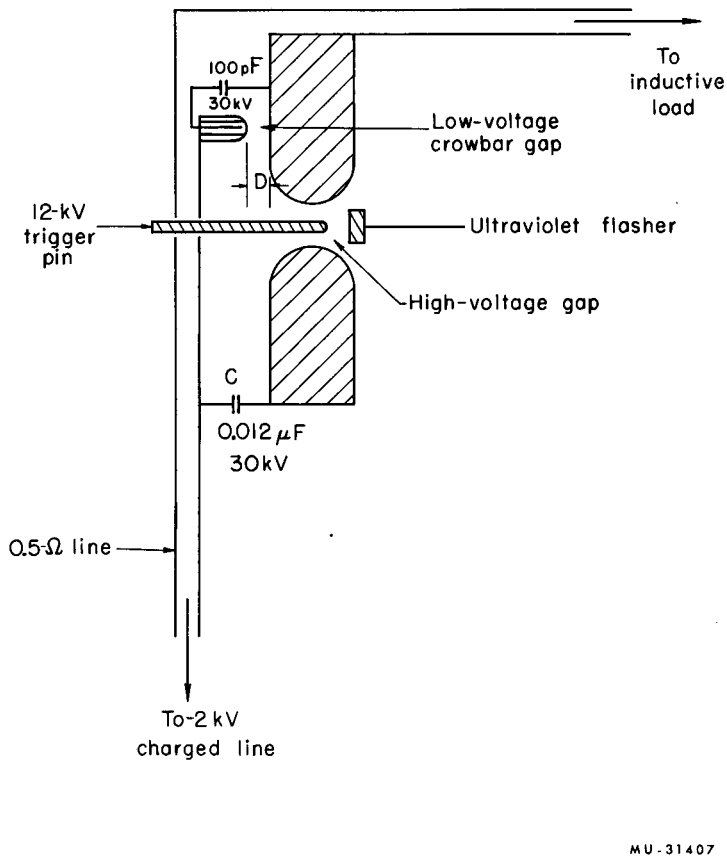

Fig. 15. Spark-gap circuitry for pulsed mirror.

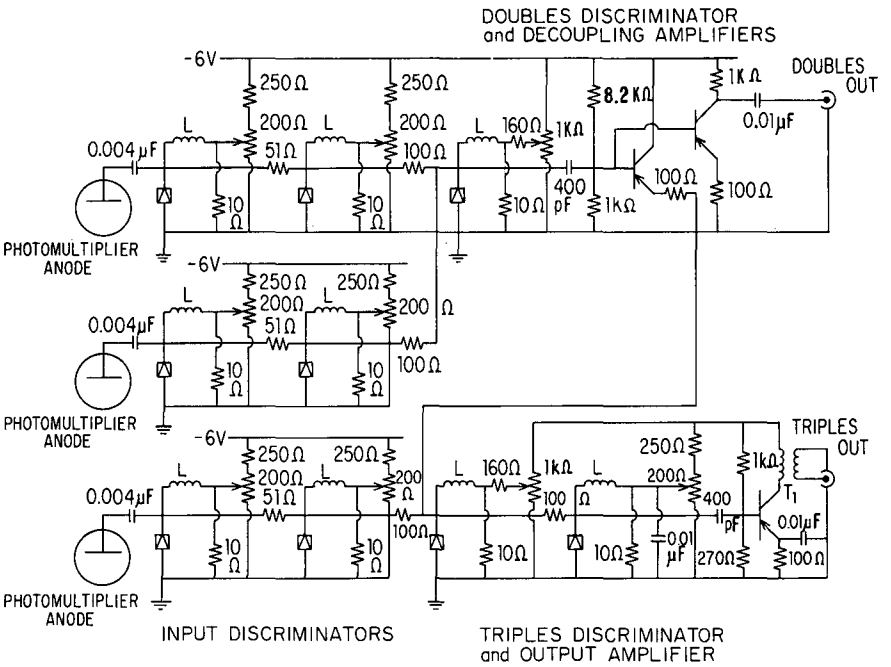

Fig. 16. Schematic of S_3—μ-counter coincidence circuit. All tunnel diodes are TD 119 (RCA) all transistors are Philco 2N 769. Trim "L" for desired pulse length 1μH or less. T_1 has 10-turn primary and 5-turn secondary, which are Trifilar wound or Terroxcube 102 core.

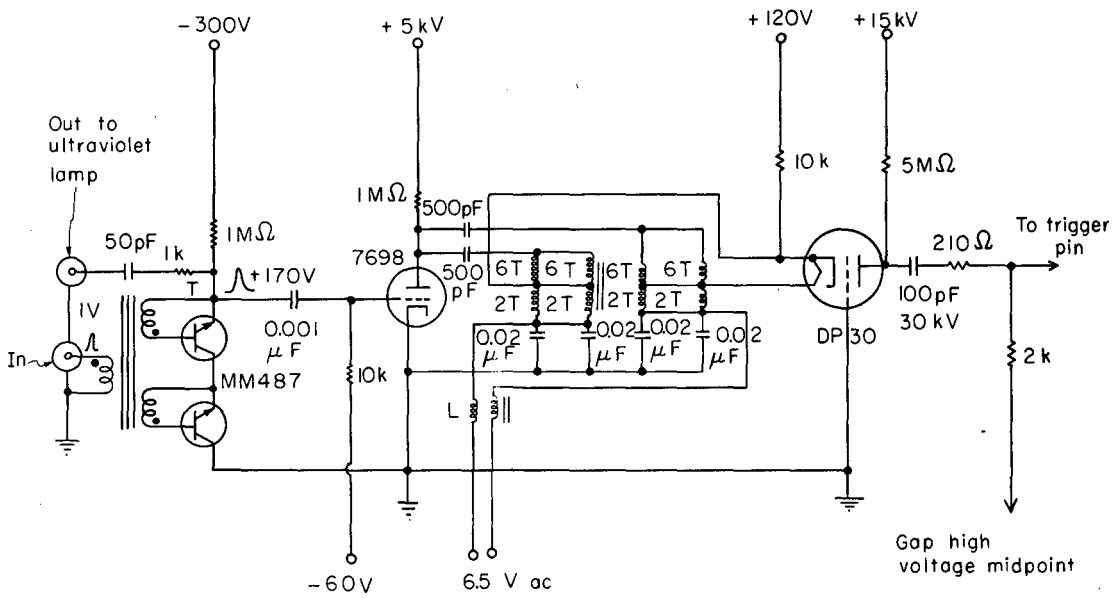

Fig. 17. Schematic of power amplifier feeding the 30 kV spark-gap trigger pin.

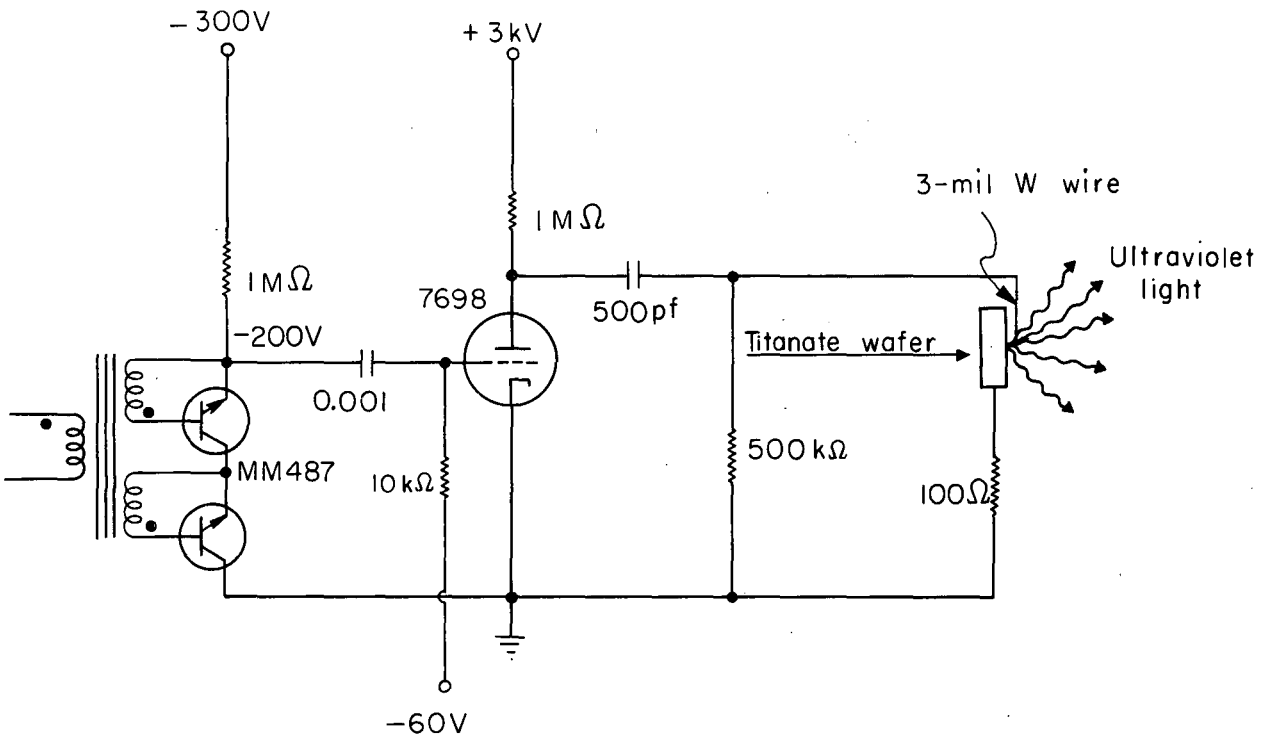

Fig. 18. Schematic of ultraviolet-light pulser.

Table IV. Time delays through trigger system.

	Delay (nsec)
Muon passage to 6199 photocathode (light-pipe time)	5
Photocathode to anode	23
Anode to coincidence output	4
Coincidence output to start of rise of pulse on trigger pin of spark gap (includes about 6 inches of RG-62U connecting cable)	11
Rise time of 12-kV pulse on trigger pin of spark gap	9
Spark-gap breakdown (time required for plasma current to build up until limited by external impedances)	$\lesssim 5$
	≈57

scattering of the muon in the scintillators to an absolute minimum. Consequently, the μ-counter scintillator was only 0.010-in. thick, the number of photons reaching the type-6199 cathodes was small, and the anode pulses were buried in the noise. The type-6199 tubes, specially selected for best signal-to-noise characteristics, were run at 2500 volts. A cathode-to-anode time of 23 nsec was measured.

Threefold and twofold coincidences of signals from the 6199 photomultiplier anodes were made with the circuit shown in Fig. 16. Each anode signal was handled by a two-stage tunnel-diode discriminator; the input diode set a triggering level, and the output diode shaped the signal to produce an output pulse whose length and height were independent of input-pulse heights. Two discriminator outputs were added resistively in a tunnel diode biased to select double coincidences. Transistor amplifiers provided decoupled outputs, one for external timing circuits in different parts of the experiment and the other to make a subsequent coincidence with the third input discriminator. The output of the triples coincidence diode, shaped by a second diode, drove a transistor output amplifier. The use of germanium tunnel diodes made undirectional coupling by germanium diodes impossible because the 200-mV output of these tunnel diodes would not switch the regular diodes. Signals were therefore directed by the use of asymmetrical resistive coupling and by an emitter follower after the doubles coincidence.

This circuit follows an earlier design except for a few changes that reduce the over-all delay from 11 to about 4 nsec. The changes include (a) the use of germanium tunnel diodes (RCA TD 119), which can switch in 0.3 nsec if not limited by the external circuit; (b) the use of resistive interstage coupling at all points where it will not result in unstable operation; (c) extremely compact circuit construction. Most of the improvement comes from (a). In normal use the input discriminators were set to a 1-mA threshold. Delays were measured with a 4-mA input signal of negligible rise time; the delay was measured between 50% level points on the input and output signals with a sampling unit (Tektronix type N). Typical coincidence curves with light pulses were 7-nsec wide full width at half maximum. The signal amplitude at any tunnel diode in the circuit is about 200 mV as viewed by the Tektronix type N unit. The delay of 4 nsec from

input to triples output is equally divided between input discriminator, doubles emitter follower, triples coincidence discriminator, and the output amplifier. The output amplifier delivers 1 V into 50 ohms; it can be dispensed with if a 200-mV output is adequate.

The general characteristics of an amplifier suitable for carrying the above 1-V 20-mA pulse up to a level where it would satisfactorily trigger the 30-kV spark gap with a minimum time delay are determined by the operating voltage of the gap as well as by the impedances "seen" by the gap. For reasons described below, a three-element gap was used here. In order to minimize t_R in the inductive load, one should use as high a voltage as possible on the pulse-producing network. As stated previously, general considerations of high-voltage engineering around the experimental apparatus resulted in the aforementioned 60-nsec rise time.

General experience indicates that one needs on the order of one-half of the gap's operating voltage on the trigger pin of a three-electrode gap if nanosecond breakdown times are to be achieved. To bring the output of the phototube coincidence circuit up to 12 kV at 20 A, we constructed the amplifier shown schematically in Fig. 17. Other combinations of small spark gaps, transistors, and tubes were investigated, but the final choice was as shown. This unit was found to be extremely reliable and, with coaxial heavy solid-metal shields compartmentalizing each amplifier section, showed no deterioration with operation even though 30 kV at 0.5 ohm appears on the trigger pin for about 30 nsec when the gap fires, and this pulse moves back, through the 210-Ω current limiting HV resistor, to the DP-30 anode. However, it was found necessary to shield magnetically the planar triodes from the 1-kG field in which they were located before the unit would operate properly.

It took approximately 11 nsec from the start of the 1-V input pulse into this amplifier to the time when the DP 30 was turned on and started to deliver current to the gap's trigger pin. About one-third of this time was needed to fire the avalanche transistors--and this was for the fastest ones in a batch of about 40. The total shunt capacitance seen by the DP 30 anode looking into the spark-gap trigger pin was about 15 pF; because this tube would deliver about 20 A, it took 9 nsec for the DP 30 to raise the voltage on the trigger pin to 12 kV. Thus a total of about 20 nsec was required to bring the input 1-V-at-20-mA pulse up to 12-kV-at-20-A on the

trigger pin of the gap, and if the gap were properly designed, it should begin to avalanche at or before this time.

To fire any spark gap quickly, two things must be done. Generally speaking, enough electrons must be liberated from one of the elements of the gap to locally overcome the capacity of the gas to absorb them and, simultaneously, the electric-field distribution in this region must be increased enough to initiate avalanche breakdown in the gas. One common method of initiating gap breakdown is to sharpen the tip of a centrally located trigger pin in a three-electrode gap and then put a voltage pulse on this pin high enough to liberate electrons either by field emission or by the ultraviolet radiation from the corona at the tip. This method requires a relatively high trigger-pin field or a sharp tip that would be subject to erosion by the plasma (or both); neither of these is consistent with minimum t_D operation for thousands of pulses. Similarly, the technique of firing a two-electrode gap by pulsing a trigger pin (usually a fine wire) just inside one of two electrodes depends for its operation on the motion of the trigger plasma with sonic speeds out into the gap where it both supplies the electrons and distorts the field. Again this technique is too slow for our purposes.

It has been known for some time that an ultraviolet source near the gap aids in gap breakdown, presumably because of the photoelectrons produced at the electrodes. However, diffusion of the electrons produced in the uv source out into the gap may also play a significant role in this technique. Both an auxiliary gap near the main one and a steady uv source have been used in the past. The auxiliary gap suffers from the same delay problems as the main one, and in addition needs quite a bit of power on the scale involved here. This power would have to come from the amplifier described above, and this takes time. Use of a steady uv source, on the other hand, simply results in the necessity of having to reduce the main-gap voltage well below the "clean" spontaneous breakdown point, and the difference must be supplied by the trigger-pin-pulse--which again takes time. The best arrangement was found to be a small power-pulsed uv source constructed by pressing the end of a 3-mil tungsten wire against the face of a 0.5-in.-diameter titanate disk. This ceramic wafer was made by sawing in half a 500-pF 10-kV ceramic condenser. The pulser that drove this uv light source, shown in Fig. 18, delivers about 5 A at 3 kV; the pulse length was chosen to be about 50 nsec. This circuit is basically the front end of

the main amplifier and needs only about 10% of the current at point T (Fig. 17) to trigger it. The uv light output rose to its maximum value about a nanosecond after the 7698 tube started to conduct (about 2-pF shunt capacitance with 5-A maximum current). Although the uv-light output from this source was not measured, individual pulses appeared to be "quite bright" when observed by eye during the daytime. The spectral distribution of this lamp is not known. This uv flasher was placed about an inch from the gap and could "see" all three electrodes (Fig. 15). Its effectiveness in liberating electrons into the gap is indicated by the experimental observation that when the gap was operated at a somewhat reduced voltage of 20 kV and held to within a few percent of the spontaneous breakdown point, this uv light pulser would fire the gap by itself, i.e., with no field-distorting pulse on the trigger pin. However, the delay in breakdown was appreciable, and as the gap voltage was raised the breakdown became sporadic, until at 30 kV the ultraviolet flasher alone would not fire the gap. With use, the white ceramic became covered with a brown deposit of residues manufactured by the plasma during the gap discharge, but its performance did not appear to be appreciably affected by this coating.

Under normal operating conditions, the delays in the circuitry were such that the uv lamp was pulsed on 19 nsec after the 1-V signal entered the "gap amplifier;" this time corresponds to the top of the rise of the voltage pulse on the trigger pin, as previously described. As far as could be seen with the present setup, onset of gap breakdown was immediate at this point (i.e., < 5 nsec).

In Table IV a summary of the delay times through each element of the pulsed mirror system is given. Note that the phototube delay is the slowest element in the chain. Since it was necessary to minimize multiple scattering in the μ-counter, a minimum amount of energy from the muon was extracted, and all 10 stages of gain in the type-6199 tubes were needed. In applications for which plenty of light is available and one is still interested in keeping the over-all delay to a minimum, about 2.5 nsec/stage can be gained by moving down to the dynode where 1 volt becomes first available.

D. Spin Flip Electronics

As discussed in Sec. II.B, in a coordinate system rotating with the cyclotron frequency of the muon, the muon spin appears to precess about the z axis (solenoid axis) with a frequency $\omega_\Delta = (g/2 - 1)\,\omega_c$. In that section it is also described how the muon spin is flipped out of the plane whose normal is the solenoid axis. This spin-flip pulse was obtained by discharging a capacitor in series with the flip wire; enough resistance was included to produce critical damping. The amplitude of the flip pulse as a function of time, determined with a pickup coil, was in agreement with a calculation based on the electrical parameters of the circuit. The electronics for generating the flip pulse from the output of the logic electronics is shown in Fig. 19. The cable from the hydrogen thyratron (KU405c) to the flip wire consisted of 10 lengths of RG8/U in parallel. The shape of the flip pulse was well represented by $I = Ate^{-t/\tau}$, with $\tau = 72$ nsec.

The equations of spin motion were numerically integrated to determine the resulting spin flip. If S_r, S_θ are the nonzero components of the spin at the start of the flip pulse, the z component of the spin just after the flip pulse is given by $S_z = 0.88\,S_r + 0.38 S_\theta$. This results in a phase shift of 23° of the radial-spin component before flip relative to the axial component after flip. The maximum amplitude of S_z is 0.96, which is a result of an unimportant technical compromise.

E. Logic Electronics

In order for one to perform the sequence of operations described in the Introduction and which lead to data for Fig. 4, one must provide a system that takes the signal from the muon telescope and generates a delayed spin-flip pulse. Electrons from muon decays occurring after the spin flip are then counted; the number of these per trapped muon is then the ordinate of Fig. 4.

The above functions were done automatically by a device that counted the number of decay electrons occurring after 1 of 64 distinct flip times which occur in a period of 6.4 microseconds. The flip delay was increased by 0.1 microsecond after each pair of incoming muons, and electron counts were stored in the appropriate section of a 64-word-core memory. In this way, 128 successive muons spanned the entire range of 64 possible flip

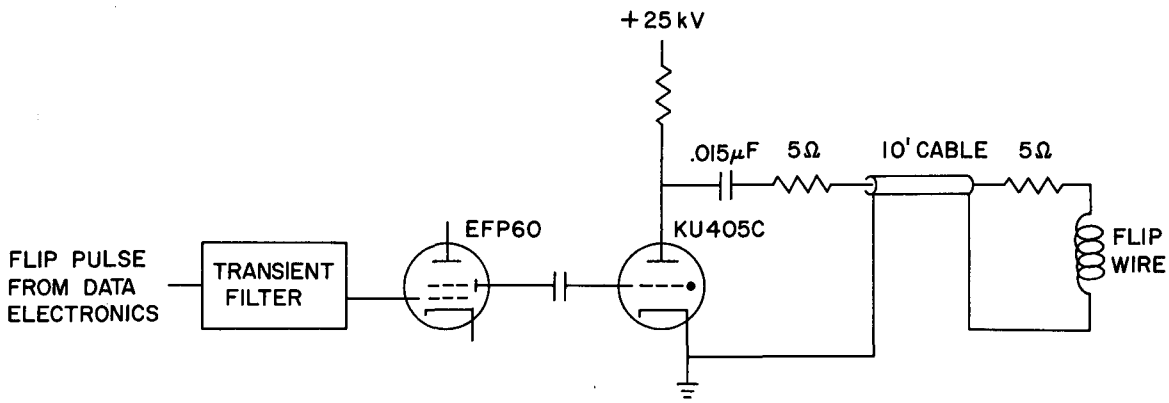

Fig. 19. Electronics of flip-pulse generator.

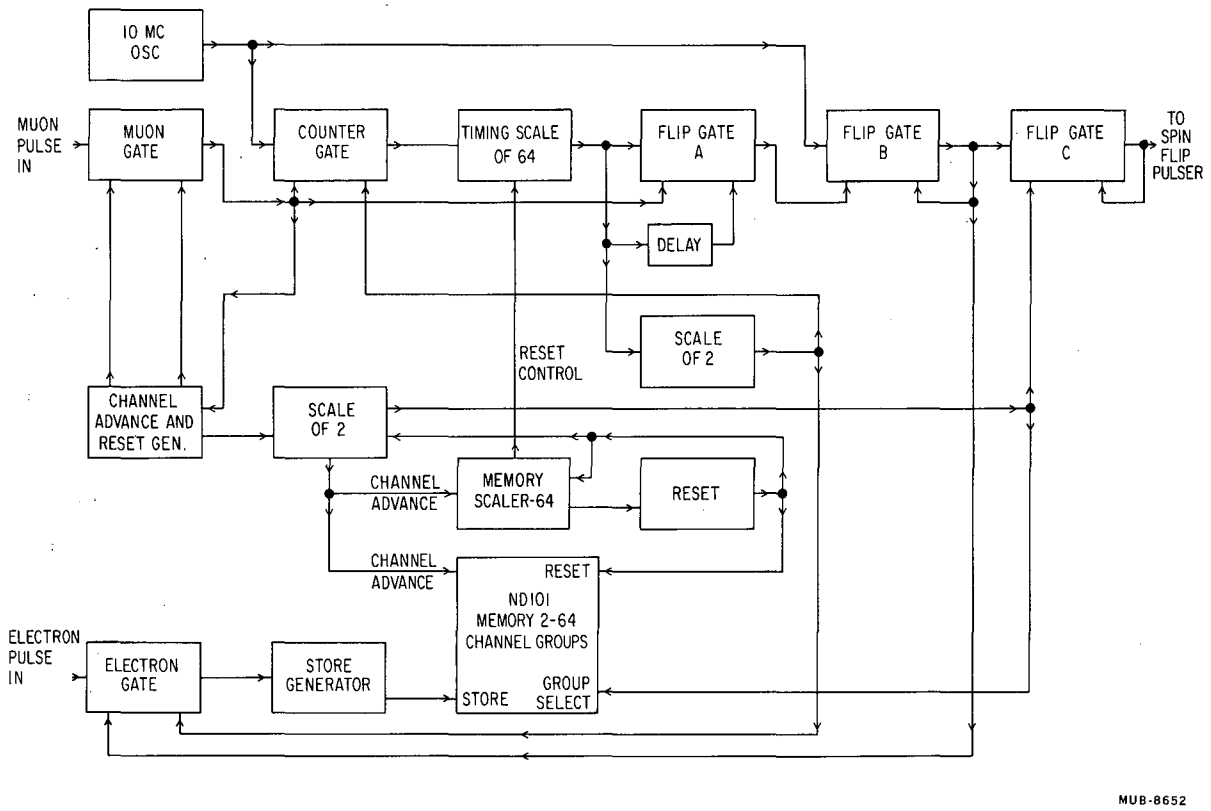

Fig. 20. Block diagram of data-recording electronics.

times, with the obvious benefit that drifts in counter efficiency or muon injection produced no spurious modulation of the time distribution, except in the unlikely case of coherence with the cycle of 64 used in data taking.

Only half of the muons were spin flipped. At each value of flip time, two muons were accepted. One was selected to produce a flip pulse while the other did not, and the resulting decay electrons from these two muons were stored in different halves of the memory. This process yielded 64 words of data from spin-flipped muons, and 64 from unflipped muons. The unflipped muons of course showed no anomalous precession.

A block diagram of the data electronics is shown in Fig. 20. Rather than describe the operation in detail, we comment on the functions carried out by the system. The time interval between muon in and flip pulse out was generated by counting a 10-mc oscillator in a scale of 64 which had been preset to the binary complement of the number of tenth microseconds in the desired interval. Errors due to scaler propagation time were eliminated by using the scaler output to gate a pulse from the 10-mc oscillator which was being counted and using this as the flip signal. The flip signal was also used to open a gate for the electron pulses; this gate remained open for 6.4 microseconds, an interval generated by letting the timing scaler count to 64 once again. An electron pulse during this interval resulted in a store command to the memory.

The timing scaler and the core-memory-address scaler were controlled from the memory scaler, which "remembered" the flip time while the timing scaler counted. After passage of each pair of muons, the memory scaler and the core-memory-address scaler were each advanced by one. After passage of each muon, the timing scaler was reset to the binary complement of the number in the memory scaler. The synchronization of the memory and core-memory-adress scalers was checked at each cycle of operation (128 muons).

The muon gate was closed 50 nsec after a muon pulse was accepted and remained so until all operations were complete and all circuits recovered. The electron gate was closed except for the 6.4-microsecond interval following the flip time.

Auxiliary equipment was available to reject electron stores that could have come from more than one muon. Because of the low muon-injection rate, it was not needed.

All of the above circuitry was transistorized. The scalers were capable of a 40-mc timing rate, and gates switched in about 6 nsec.

F. Counters

Seven counters were used in the apparatus, all of which were plastic scintillator – photomultiplier combinations. Some of the experimental problems encountered in the design and construction of these counters are of sufficient interest to warrant recording their solutions.

The location of each counter can be seen in Figs. 1, 5, and 6. Numbers C1, C2, and C3 were standard muon-beam counters that used plastic scintillators (about 1/4 by 1 by 2 inches) from which the light was piped through solid Lucite rods 3-feet long to phototubes (type-6810) on C1 and C2 and to a phototube (type 6199) on C3. As previously mentioned, it was necessary to place all phototubes far enough from the solenoid so that they could be shielded from the fringe magnetic field. A triple, coaxial iron and mu-metal cylinder shield was used with the common axis of the shield perpendicular to the solenoid axis. This arrangement allowed operation of the phototubes in a field of about 1 kilogauss with less than a 20% loss in pulse height when the solenoid was turned on.

The most difficult counter problems were encountered in the design and construction of the μ-counter and the inner electron counter ($e_1\overline{A}_1$). Detailed drawings of these two counters are given in Figs. 21 and 22.

The μ-counter had to (a) present as little material as possible to the passing muon because of multiple scattering and range-stoppage losses, with 50 mils of plastic scintillator being much too much, (b) operate with as little time delay as possible with 5 nanoseconds making a noticable difference; (c) pass through a vacuum seal; (d) operate at a sufficient level above noise to have $<< 1$ accidental logic coincidence/sec.; (e) operate in a region where an unavoidable gas discharge (from the pulsed mirror) illuminated the counter with a "bright to the naked eye" pulse of light for a few milliseconds after the muon passage; (f) operate in a dc magnetic field at ≈ 30 kG; and (g) pick up as many muons as possible within the "correct" range of pitch angles and also reject as many as possible of those outside this range. All of these requirements eliminated gas and/or solid-state counters from consideration. The final configuration of light pipe and 0.01--inch thick plastic scintillator is shown in Fig. 21. Several different orientations

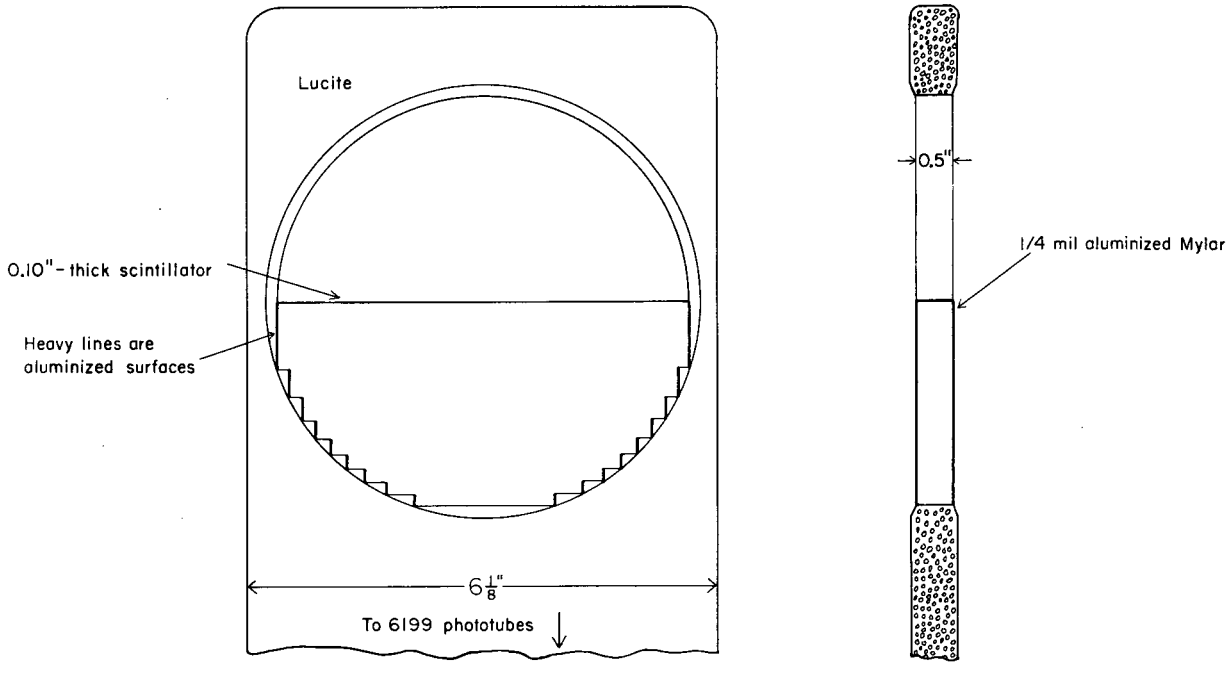

Fig. 21. Mu-counter head.

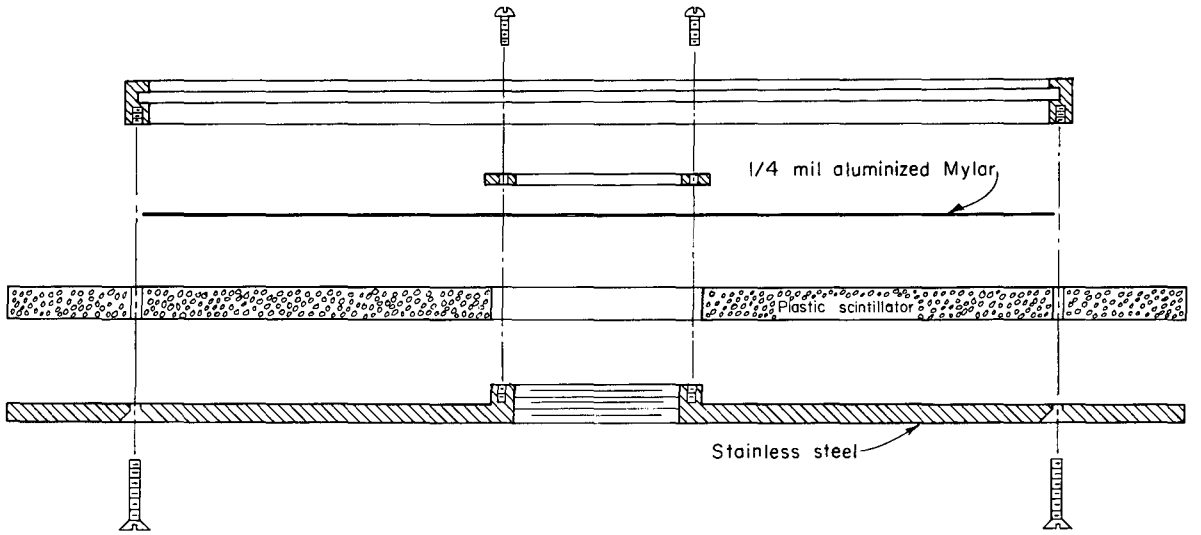

MUB-8780

Fig. 22. Expanded view of $e_1\overline{A}_1$ counter head.

of the scintillator (radial spokes and various angular positions), several different thicknesses of scintillator, coatings of white paint and/or evaporated aluminum on both scintillator and Lucite "head," and placement of the scintillator "end-on" were tried. Both electrons and 20-MeV protons were used in these tests. The 20-MeV protons were readily obtained with the same optics setup as was used with the 150-MeV/c muon beam by a change in the currents in the optics magnets. The 20-MeV protons worked most satisfactorily for these tests since they have the same dE/dx as the highest momentum trappable muon (≈ 3 times minimum), can be readily collimated so that all areas of the counter can be explored, and can be stopped in a back-up counter behind the mu-counter so that background can be completely eliminated. The light was carried out of the solenoid by a 1/2 inch by 6 inch slab of Lucite to the fringe-field region where the light was split in half and piped to two 6199 photomultipliers in coincidence.

The requirements on the inner electron counter ($e_1\overline{A}_1$) were of a different character but presented just as severe problems. An expanded drawing of the head is shown in Fig. 22. This counter had to (a) be used as an anticounter to reject those muons that tripped the S_3-μ counter coincidence but had pitch angles too large to be reflected by the bottom mirror ($\epsilon > 6°$) and hence stopped in this $e_1\overline{A}_1$ counter (if not rejected, these muons look just like trapped muons but, of course, supply only background to the final data); (b) be inside the vacuum, because the range of an $\epsilon = 6°$ 40-MeV/c muon is much less than the thickness of a six-inch-diameter vacuum window; (c) be completely light tight from the gas discharge that takes place inside the vacuum when the pulsed mirror is turned on; (d) be thick enough to count muon-decay electrons (minimum ionizing particles); (e) carry the scintillation light out three feet to the fringe-field region; (f) allow the spin-flip rod to pass through it from outside to inside the vacuum; (g) carry the spin-flip pulse (5000 A $\approx$ 200 nsec) from the center coax to the outside brass cylinder (the vacuum wall). The parts of the counter head were screwed together and then sealed at all edges with epoxy resin. An opaque epoxy sealed the 1/4-mil aluminized Mylar to the upper stainless steel ring. In practice, the mechanical strains set up in this counter after the vacuum chamber had been evacuated several times resulted in a loosening of the epoxy-metal-plastic bond and caused the most annoying vacuum problem in the system.

The bottom electron counter (e_2) was a "standard" scintillation counter with shape similar to $e_1\overline{A}_1$.

The last counter, namely the upper anticounter ($\overline{A}_2$) was placed inside the vacuum as shown in Fig. 5, and shielded from the light with 1/2-mil stainless steel foil; its light was piped out of the vacuum system through a Lucite rod sealed with epoxy to the brass lid.

Considerable effort was made to determine the efficiencies of each of these counters in order to keep track of every muon that entered the bottle, and eliminate electronically those that escaped. Standard coincidence-anticoincidence techniques using muons, protons, and electrons were employed. Innumerable voltage plateaus, discrimination bias, and cable-delay curves were taken. The results are given below.

The S_1, S_2, and S_3 beam counters were essentially 100% efficient at counting muons in the incoming beam.

Both the $e_1\overline{A}_1$ and the e_2 counters were more than 90% efficient at counting minimum ionizing electrons. Voltage plateaus were flat and of reasonable width.

The efficiency of the μ-$e_1\overline{A}_1$, and the $\overline{A}_2$ counters for counting muons was a strong function of the time delay chosen between the S_3 counter and the μ-counter in their coincidence circuit. This effect is simply due to the selection of pitch angles which any given $S_3 \rightarrow \mu$-counter delay makes. For a given muon $|$ momentum $|$, a shallower orbit takes longer to spiral down from S_3 to the μ-counter than does a steep orbit, and therefore requires a longer delay cable between the two counters to make a coincidence. Unfortunately, the resolving time of the $S_3\mu$ coincidence circuit (7 nsec) was of the same order as a typical $S_3 \rightarrow \mu$ transit time. This circumstance, coupled with the muon $|$momentum$|$ distribution, meant that even though some pitch-angle selection could be achieved by changing this delay, the dependence was not sharp by any means. However, with no mirror currents flowing but everything else operating, changing the delay cable between S_3 and μ-counter from 2 to 9 feet changed the ratio $\mu S_3(e_1\overline{A}_1)/\mu S_3$ from 0.8 to 0.3. At the same time, the ratio $\mu S_3\overline{A}_2/\mu S_3$ varied from 0.1 to 0.25. All of these numbers were also strong functions of collimator dimensions, solenoid field, and mirror strengths, and somewhat weaker functions of the physical position of the S_3 counter, the tilt of the solenoid axis, and several other variables. In the final configuration of all these variables, the numbers given in Table V were measured for these efficiencies.

Table V. Anticounter efficiencies.

	Fixed mirror	
	On	Off
$\mu S_3(e_1\overline{A}_1)/\mu S_3$	0.30	0.61
$\mu S_3\overline{A}_2/\mu S_3$	0.30	0.14
$\mu_{DEL.}\,\mu S_3/\mu S_3$	0.26	0.07

Many factors contribute to these numbers. One, scattering of the muons as they passed through the μ-counter accounted for most of the missing particles. In looking at the time distribution (after t = 0, defined by $S_3\mu$ coincidence) of muons arriving at the $\overline{A}_2$ counter, for example, we observed that about 30% of the mu's arriving at the $\overline{A}_2$ counter were "prompt;" i.e., their pitch angles were reversed in sign when the muons passed through the mu-counter and never reached the uniform-field region. Two, a sizeable fraction actually stopped in the μ-counter (after several passes through it) and were therefore never "seen" again. Three, scattering in the μ-counter could shift the center of the mu's orbit in the transverse plane enough that the orbit could intercept the central rod and thereby be lost. Making the center section of the collimator (see Fig. 5) large enough, however, eliminated this loss. Four, some pitch angles never made it down to $e_1\overline{A}_1$, even with no fixed mirror, because of a slight increase in $B_{sol.}$ from the top to the bottom of the solenoid. Five, an unavoidable "dead spot" in the $e_1\overline{A}_1$-counter just opposite the center hole from the light-pipe side occupied several percent of the $e_1\overline{A}_1$ face. Six, the μ-counter itself was about 50% efficient at counting those muons that were reflected when the fixed mirror was turned on. (This type of event is given in the table as $\mu S_3\mu_{DEL.}/\mu S_3$. This percentage is due both to the fact that the height of the μ-counter (1/2 inch) is such that it intercepted about one-half of the muon orbits and to the efficiency of the μ-counter for those mu's that do pass through it (probably > 80%). Finally, the geometrical configuration in the neighborhood of the A_2-counter was such that the brass lid unavoidably stopped about 30% of the muons that spiraled back up into the $\overline{A}_2$ region.

IV. EXPERIMENTAL WORK

A. Muon Source

Three possible sources of polarized muons were considered:

a. The muons "contaminating" the pion beam,

b. The muons from pions stopped in thin sheets of material,

c. The "forward" muons from in-flight pion decay (Appendix A).

The first possibility was ruled out in a preliminary beam study; the muon component of the meson beam turned out to be essentially unpolarized in the desired momentum range ($\approx$ 100 to 200 MeV/c). Further diagnostic work indicated that muons from forward in-flight pion decay were better suited to the experiment than muons from stopped pions. The basic problem in using muons from stopped pions was that in order to get the muons (4.2 MeV) out, the pion stopper had to be very thin (less than 100 mg/cm.^{2});this thickness made stopping a large number of pions difficult. Various geometries were tried, which, in conjunction with the $(g-2)_\mu$ solenoid magnetic field, permitted multiple traversal of the stopper by the pions. Even though some configurations enhanced the pion stopping power substantially, the technique, for our purposes, remained inferior to the use of muons from forward in-flight pion decay.

The most convenient momentum range for muons trapped in the solenoid was 30 to 50 MeV/c. It was desirable that the muon beam have a somewhat higher momentum, which made injection into the high-field region easier, and allowed the muons to lose energy in the beam-counter telescope. However, if the momentum was much higher (about 350 MeV/c was the peak of the meson-production spectrum), degrading smeared out the muons in a very thin layer in phase space, and the fraction from 30 to 50 MeV/c became very small. The momentum finally chosen (150 MeV/c) was the best compromise between the meson-beam flux (rapidly rising with increasing momentum) and the useable fraction after degrading (rapidly falling with increasing momentum).

The characteristics of the beam finally used are:

Pion momentum, 135 MeV/c

Forward-decay-muon momentum, 150 MeV/c

Muon polarization, 60%

Polarized-muon flux, 3000/sec over 1 sq. inch.

This method of producing polarized muons has the nice property of giving quite pure beams (making background low), since no single particle can get through the optics system; the upstream bending magnet was set for 135 MeV/c, the downstream bending magnet at 150 MeV/c.

The polarized muon beam is shown in Fig. 7. After momentum selection in the first bending magnet (Atlas), the 135-MeV/c pions had a straight flight path of $\approx$ 12 feet between Atlas and Titan (the second bending magnet). The muons (from decaying pions) that went in the forward direction along the beam line were polarized and had a momentum of $\approx$ 150 MeV/c. Thus Titan was set so as to send particles of 150 MeV/c into the $(g-2)_\mu$ solenoid (Aphrodite). The pions that did not decay were bent through a larger angle by virtue of their lower momentum and thus missed Aphrodite.

B. Static Diagnostics (Pulsed Mirror Not Operating)

After developing and constructing the polarized muon beam and experimental apparatus, we needed considerable time to tune the whole apparatus for best performance; this diagnostic tuning occupied much of the actual running time, and is described below.

Initially, we were interested in maximizing the number of those muons that were reflected from the bottom mirror, and were thus seen in counter $\overline{A}_2$ in the absence of the top pulsed mirror. More precisely, we wanted to maximize the number of reflected muons returning at times later than 100 nsec after their entry into the solenoid; these were the "trappable" muons. Muons that return at earlier times escape before the top mirror can be closed. Therefore, in this first phase of the diagnostics we took a series of time-of-flight curves, starting with a μ_T coincidence and stopping with detection of the muon in $\overline{A}_2$.

1. Degrader

The muon momentum degrader between S_2 and S_3 was adjusted first. This degrader was made of boron carbide (B_4C) for two reasons: (a) to reduce multiple scattering to a minimum; and (b) among low-Z compounds it appears to be the most dense (with the exception of diamond), with $\rho = 2.5$ c.m./cc . The B_4C was obtained in blocks of appropriate size ($\approx$ 2-1/2 by 1-1/2 by 1/2 in). The amount of boron carbide between S_2 and S_3 was varied, sweeping out a range curve. The maximum in "late reflections" was obtained at the same thickness as the maximum in μ_T coincidences ($\approx$ 2 inch B_4C).

2. Fixed Mirror Strength

The strength of the bottom mirror was also varied, from no current to about 400 A ($\approx 3\% B_{sol.}$). At zero current, a very few muons returned to $\overline{A}_2$, because of a slight slope in the solenoid field. As the mirror current was increased the number of returning muons increased, but the number of late returns leveled off at about 250 A and actually decreased somewhat at the highest mirror strengths. The reason for this behavior is that those muons reflected only by currents greater than 250 A had fairly steep helix pitch angles, made the round trip in less than 100 nsec, and were, therefore, not trappable. Also at these currents, the shallow-pitch muons turned around somewhat upstream of the mirror, and some completed the (shorter) trip in less than 100 nsec. Since the most efficient anticounter is $(e_1\overline{A}_1)$, we set the bottom mirror to 250 amperes, to allow as many as possible of the nontrappable muons to hit $e_1\overline{A}_1$. Figure 23 shows the time-of-flight distribution from μ_T to $\overline{A}_2$ for a small bottom mirror, and also for a 250-A mirror.

3. $S_3 \rightarrow \mu$-Counter Flight Time

One of the most important variable parameters was the time delay between S_3 and the μ-counter in the μ_T coincidence circuit. If this delay is set to zero, then a μ_T coincidence would be made on muons that travel almost straight down from S_3 to the μ-counter, i.e., $\epsilon \approx 90°$. If the delay is made longer, the muon making a μ_T coincidence must take longer to travel from S_3 to the μ-counter, a straight-line distance of 6 inch. Because the momenta below $\approx$ 30 MeV/c were eliminated by one collimation,

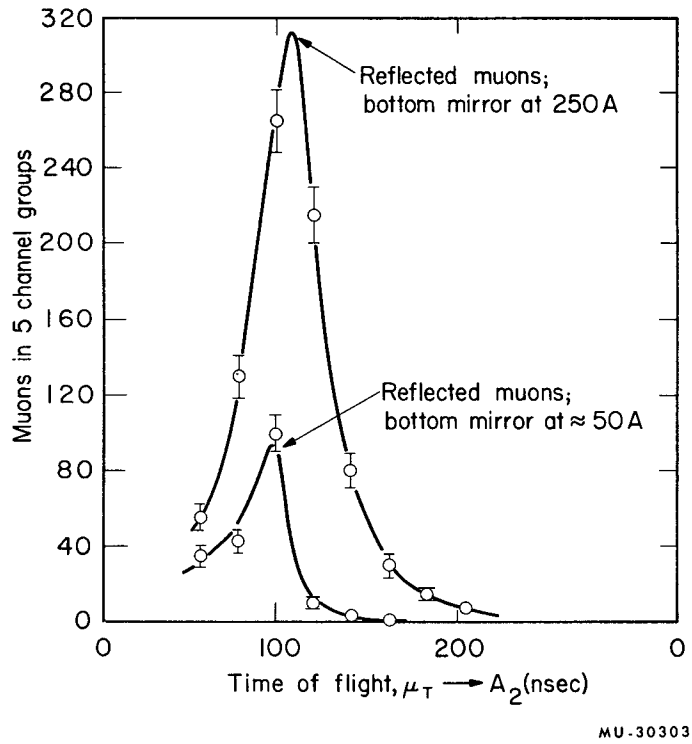

Fig. 23. Muon reflection from bottom mirror.

the longer travel times must represent flatter (shallower) pitch angles of the helical orbits. And since muons with flat pitch angles are the ones that take the longest time to make the round trip to $\overline{A}_2$, the S_3-to-μ flight-time requirement provided a means for picking out the muons that are trappable. This worked well, as is shown in Fig. 24. The late returns were maximized at about 7 feet of $S_3 \rightarrow \mu$ delay, but the number of μ_T's was considerably less than its maximum value. This was desirable, since the fraction of μ_T's that are trappable is thus greatly enhanced by the flight-time requirement, and the final signal-to-background ratio is proportional to this fraction. The $S_3 \rightarrow \mu$ delay was set at 8 feet, where the fraction of trappable μ_T's is largest. At more than 8 feet delay, the trappable fraction falls off again, and the overall counting rates drop even more precipitously.

4. Solenoid Tilt from Vertical

Finally, the μ_T counting rate was sharply improved by tilting the solenoid axis at about 5° to the vertical. One reason for this improvement is schematically shown in Fig. 1. The entering muons have about the right pitch angles initially when the solenoid is tilted. But much of the improvement is due to a somewhat larger effective entrance gap. The muon orbits in the entrance gap are curved vertically (as well as horizontally), but the gap is not, and many more muons get through when the solenoid axis is tilted by a few degrees.

The dependence of the number of late returning muons on any one of the above parameters depends on the settings of the other parameters. Therefore, several "iterations" were carried out to ensure that the optimal combination of settings was achieved.

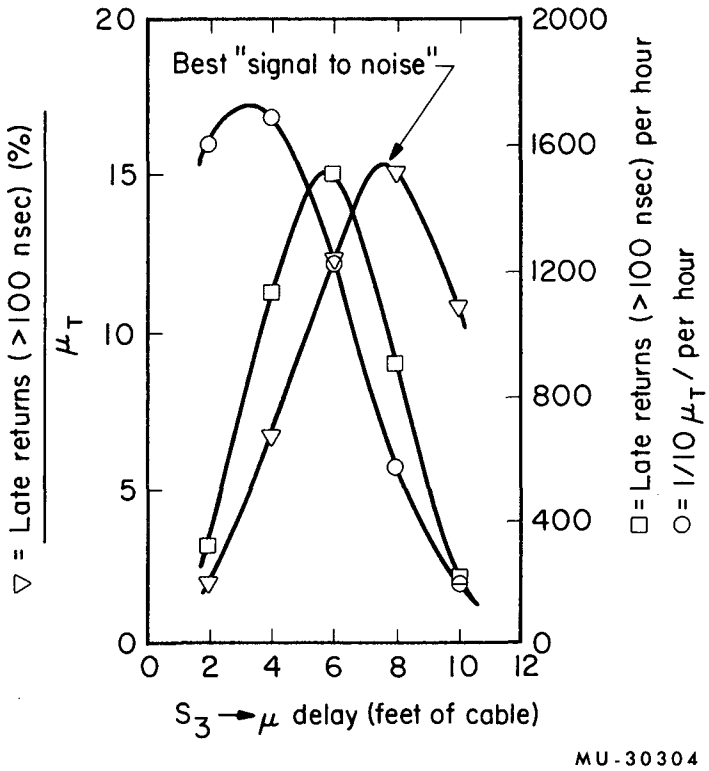

Fig. 24. Reflected shallow-pitch muons vs cable delay between S_3 and the muon counter.

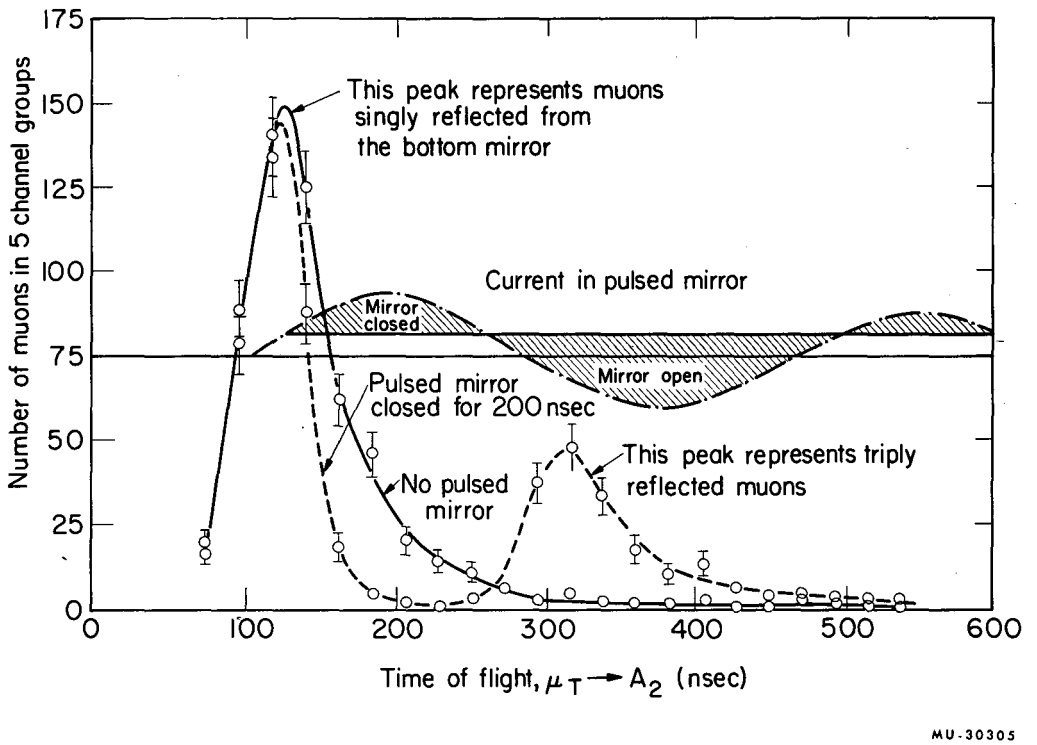

Fig. 25. Muons trapped in the solenoid for at least three reflections from the end mirrors.

C. Dynamic Diagnostics (Pulsed Mirror Operating)

1. rf and Light Shielding

As previously mentioned, the 30-kV 5000-A pulse through the single-turn coil that formed the upper mirror caused considerable light output from the residual gas in the vacuum chamber. It was not possible, in the time available, to keep the operating vacuum much better than about 1/2 micron. Consequently, all counters "exposed inside the vacuum chamber" were made light tight. The closeness of the μ-counter scintillator to the pulsed coil resulted in a large flux of kilovolt-range electrons (produced in the discharge) impinging on this scintillator. Consequently, it was necessary to gate off the μ-counter for several microseconds, the start of the gate being about 50-nanoseconds after the μ_T (t = 0) coincidence.

In addition to the light problem, considerable rf pickup in all the counter cables was encountered. Double electrical shielding of all counter cables, tubes, and even light pipes reduced this pickup to a tolerable level.

2. Three-Reflection Trapping (0.2 microsec)

After the pickup problem was solved, the top mirror was turned on for 200 nsec. Again, the diagnostic tool was muon time-of-flight from μ_T to $\overline{A}_2$. Figure 25 shows the effect of the top mirror. With the top mirror on, muons (those returning to $\overline{A}_2$ at times > 100 nanosec in the absence of the top mirror) were reflected back toward the bottom mirror, from which they must be reflected again in order to be seen in $\overline{A}_2$. Therefore, the late mirror-on peak represents muons that have made three reflections off mirrors, two from the bottom and one from the top.

3. One-Microsecond Trapping

Having seen that the top mirror did indeed reflect the late-returning muons, we next lengthed the pulsed mirror to one microsecond. Figure 26 shows the results. The late peak now represents muons that have been trapped for 1 microsec and have made many reflections off both mirrors.

4. Fifteen-Microsecond Trapping

Although the results of the 1-μsec trapping were encouraging, an examination of trapping for the full 15 μsec was needed. It would have been futile to look for the exiting muons, because 999 out of 1000 decay first.

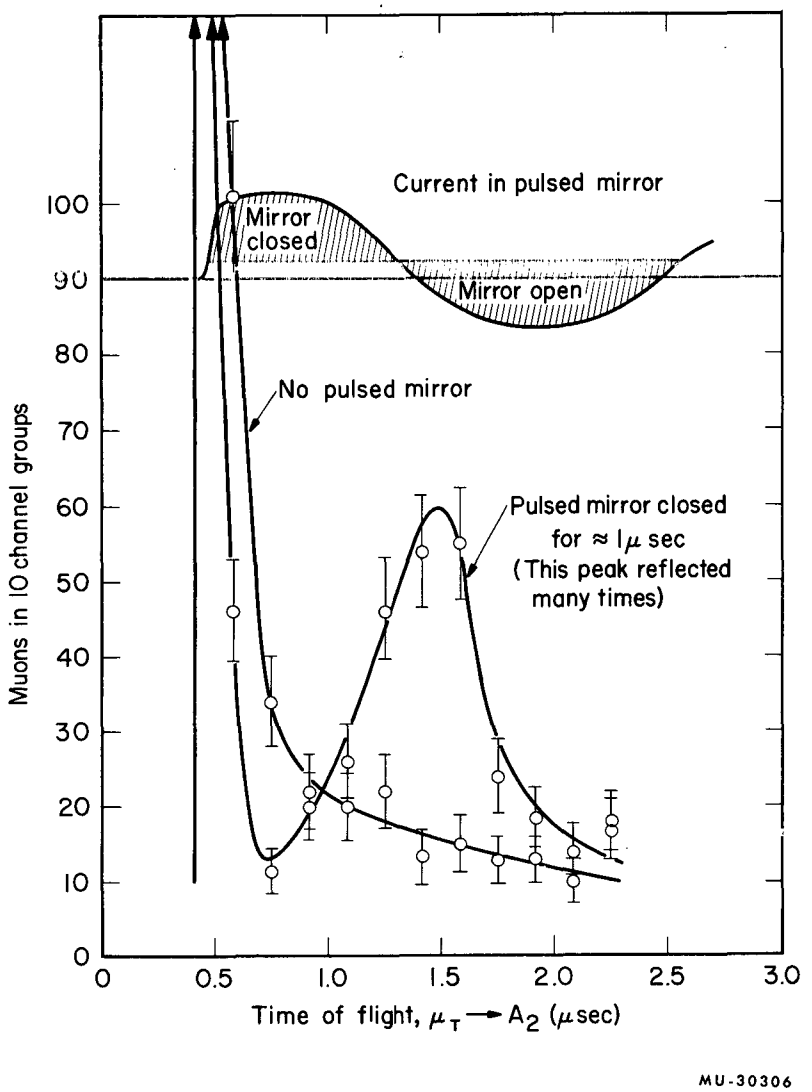

Fig. 26. Muons trapped in the solenoid for many reflections from the end mirrors (pulsed mirror closed for ≈ 1 μsec).

Therefore, decay electrons from muons were counted ($e_1 e_2$) with the top mirror pulsed on for the full 15 microsec, as well as with the top mirror off. Figure 27 shows the result. The difference between the two points on this figure does not give the actual signal since some of the electrons included in the "background" point come from trappable muons that have been reflected all the way back up to $\overline{A}_2$. Additional measurements of the efficiences for detecting electrons originating from different points of the chamber were made. These "electron efficiency" and background measurements indicated that, in the data-taking runs, about 40% of the electrons seen in ($e_1 e_2$) came from true trapped muons, and 60% came from muons that had activated all the logic and counting electronics but were not actually trapped; i.e., were sitting somewhere on the walls when they decayed. The expected $(g-2)_\mu$ asymmetry was thus computed to be:

$$A = a\, P\, S/(B+S), \tag{41}$$

where P = fractional polarization = 0.6

a = μ-decay asymmetry parameter = 1/3

S = signal electrons = 0.4

B = background electrons = 0.6 .

D. Final Data

After we finished the diagnostics described in the preceding sections, we took the final data with alternate incoming "trapped" muons having their spins not flipped and flipped. The final data are shown in Figs. 28 and 29. During the data taking runs the following items were kept under continuous surveillance.

a. Beam optics and solenoid currents,
b. Vacuum, and LN trap,
c. Counter voltages,
d. Voltages and currents in mirror and flip electronics,
e. Solenoid temperature,
f. All counting rates,
g. Cyclotron beam and its spill,
h. Gas pressures and flow in spark gap,
i. Delay and overall appearance of pulsed mirror current.

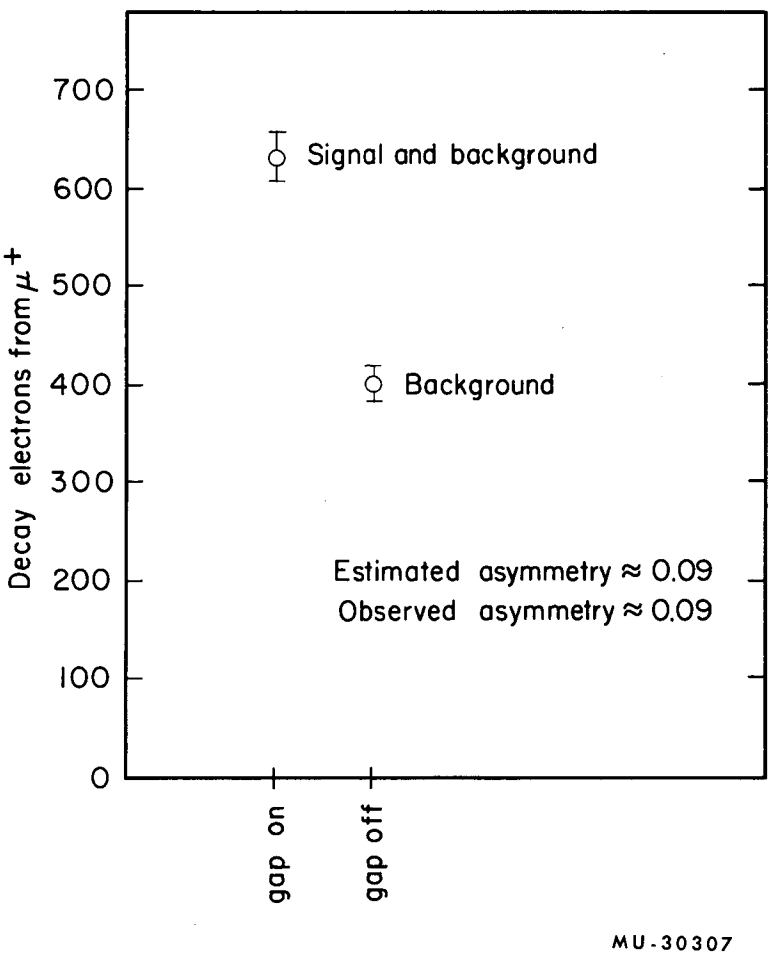

Fig. 27. Electrons in the e_1e_2 counters from muons with and without the full 15-μsec pulsed mirrors.

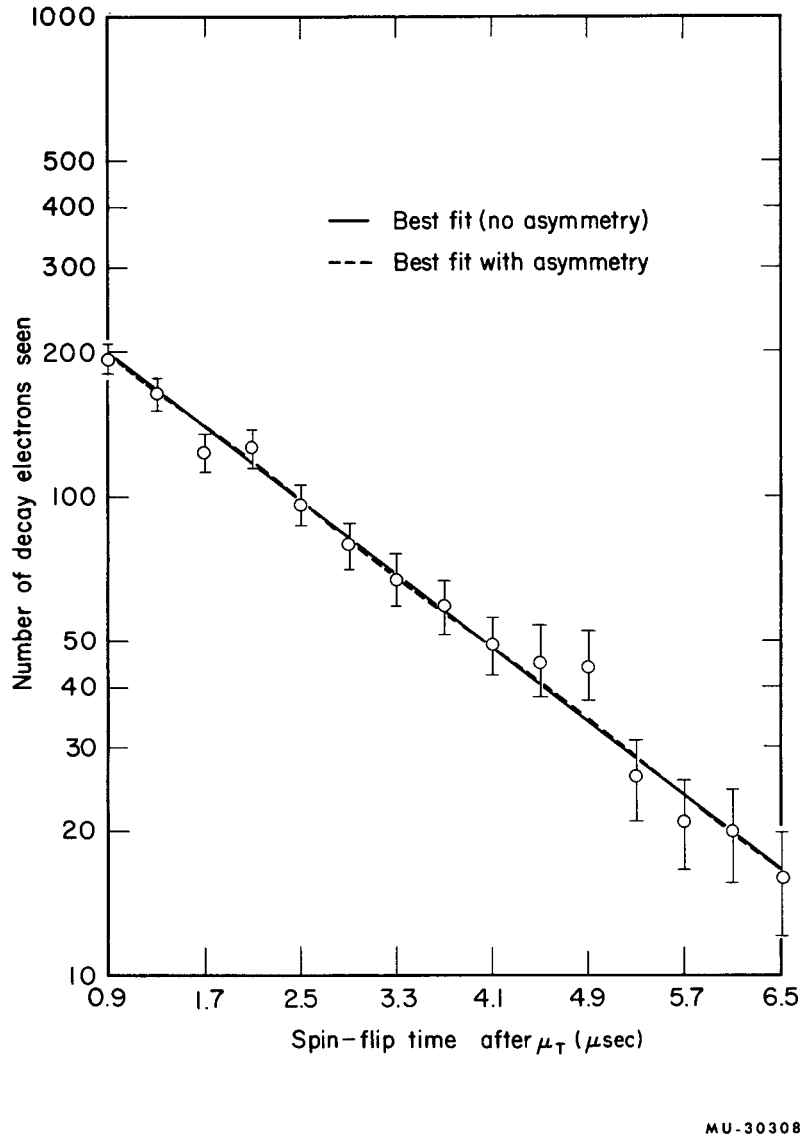

Fig. 28. Final no-flip data.

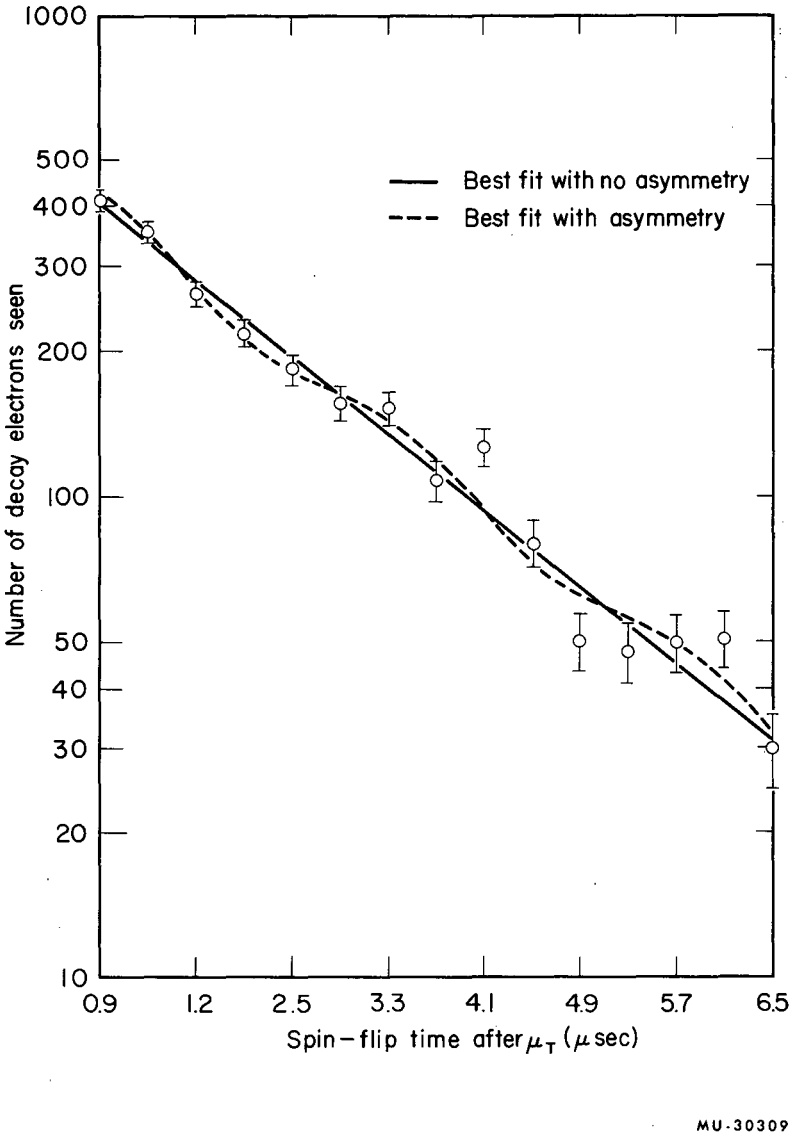

Fig. 29. Final flip data.

The weakest links in the whole system were the 30-kV capacitors in the spark gap. These capacitors received hard use, "ringing" for many cycles on each discharge. At distressingly frequent intervals, one or another of the three 30-kV condensers would break down. Replacement was mechanically inconvenient.

The overall counting rates were as follows:

a. S_1S_2 — 120,000/min,
b. $S_1S_2S_3$ — 29,000/min,
c. μ_T — 200/min,
d. μ_T followed by one of the anticounters (i.e., the muon was observed to be not trapped) - 144/min,
e. Estimated trapped muons — 20/min,
f. Electrons from muon decay — 1.8/min.

In order to lengthen 30-kV condenser life, we usually ran at half beam, obtaining the rates listed.

V. DATA ANALYSIS

A. Techniques

The data were analyzed by standard techniques (Refs. 30 and 31). The theoretical curve (Fig. 4) was fitted to the data by the maximum-likelihood method. The best-fit parameters of the theoretical function were then used in conjunction with the final data to compute the "error matrix," from which the final error estimates were obtained.

The no-flip data showed no obvious departure from a muon-lifetime decay curve. Nevertheless, the no-flip data were run through the same analysis procedures as the flip data, to ensure that systematic effects played no role in the $(g-2)_\mu$ determination.

1. Maximum-Likelihood Method

The "likelihood function" is simply the probability density for the data taking the form that was observed, assuming some theoretical distribution (which the data should approximate more and more closely as the amount of data approaches infinity). Thus, if N observations are made, and if the statistical errors may be considered Gaussian:

$$\mathcal{L} = \prod_{i=1}^{N} \frac{1}{2\pi\sigma_i} \exp\left\{ -\frac{1}{2}\left[(Y_i - Y_{E_i})/\sigma_i \right]^2 \right\}, \qquad (42)$$

where

Y_i = theoretical value for the ith observation

Y_{E_i} = experimental value for the ith observation

σ_i = estimated error in Y_{E_i}.

From Eq. (42) it is clear that $\mathcal{L}$ depends on the theoretical values assumed; and, since these values are in general dependent on some parameters, $\mathcal{L}$ may be considered a function of these theoretical parameters. Now $\mathcal{L}$ is maximized, and the parameters for which $\mathcal{L}$ is a maximum are the best-fit parameters, determined by the data.

In our case, the number of observations is the number of different spin-flip times used (equal to the number of PHA channels used). The curve to be fitted to the data is of the form

$$Y = T(1 + A \sin x)e^{-Dt} \qquad (43)$$

where $x = Ft + B$

t = time of flip pulse (after muon entry)

Y = electron counts at t

F = angular (g-2) frequency

B = initial phase of polarization

A = amplitude of (g-2) sinusoid

D = reciprocal of muon lifetime

T = normalizing factor.

The Y_{E_i} are then the numbers of electron counts in the N channels of the PHA, and to the usual Gaussian approximation, $\sigma_i^2 = Y_{E_i}$. If the parameters in the theoretical curve are denoted by A_m, at $\mathcal{L} = \mathcal{L}_{max}$:

$$\left.\frac{\partial \mathcal{L}}{\partial A_m}\right|_{A_m = A_m^*} = 0 \quad (0 < m \leq 5), \qquad (44)$$

where A_m^* is the best-fit A_m.

Thus, it seems that one has simply to solve these five simultaneous equations to determine A_m^*. Unfortunately, these conditions are necessary, but not sufficient, for $\mathcal{L} = \mathcal{L}_{max}$.

In the very special case where the parameters enter the theoretical curve in a linear fashion, the above conditions are, in fact, necessary and sufficient for $\mathcal{L} = \mathcal{L}_{max}$. Furthermore, it is equally valid to maximize $W = \log \mathcal{L}$, and then the necessary and sufficient conditions are that

$$\left.\frac{\partial W}{\partial A_m}\right|_{A_m = A_m^*} = 0 \,. \tag{45}$$

In this case there are several linear simultaneous equations for the A_m^*, and standard matrix techniques yield immediate answers.

In the analysis of the $(g-2)_\mu$ data, the nonlinear manner in which the A_m are involved preclude use of the powerful methods available for the more usual linear situation. The technique adopted, therefore, was to guess, by eye, the best parameter values. Then holding four parameters constant, we optimized the fifth, then another parameter, and so on. If the parameters were not correlated, five successive optimizations would have determined the best-fit curve. However, since the optimum value of one parameter depends on the values assumed for the other parameters, successive iterations were necessary in the optimization, until successive rounds of optimization yielded essentially identical best-fit parameter values. Figure 30 shows the flip-data likelihood function as $(g-2)_\mu$ (proportional to frequency, F) was varied, but with the other parameters held at their best-fit values.

2. Error Matrix

Correlations among the parameters also required the use of the error matrix technique for error estimation. In the event that there are no correlations, the likelihood function is an M-dimensional Gaussian which is the product of M one-dimensional Gaussians in one parameter each. In parameter space, therefore, the parameters define M orthogonal axes, and the error in one parameter is equal to the σ of the one-dimensional Gaussian.

In general, the parameter axes in parameter space are nonorthogonal and curvilinear. In the usual treatment (and the one adopted here), one assumes that the axes' curvature may be neglected, and only the nonorthogonality

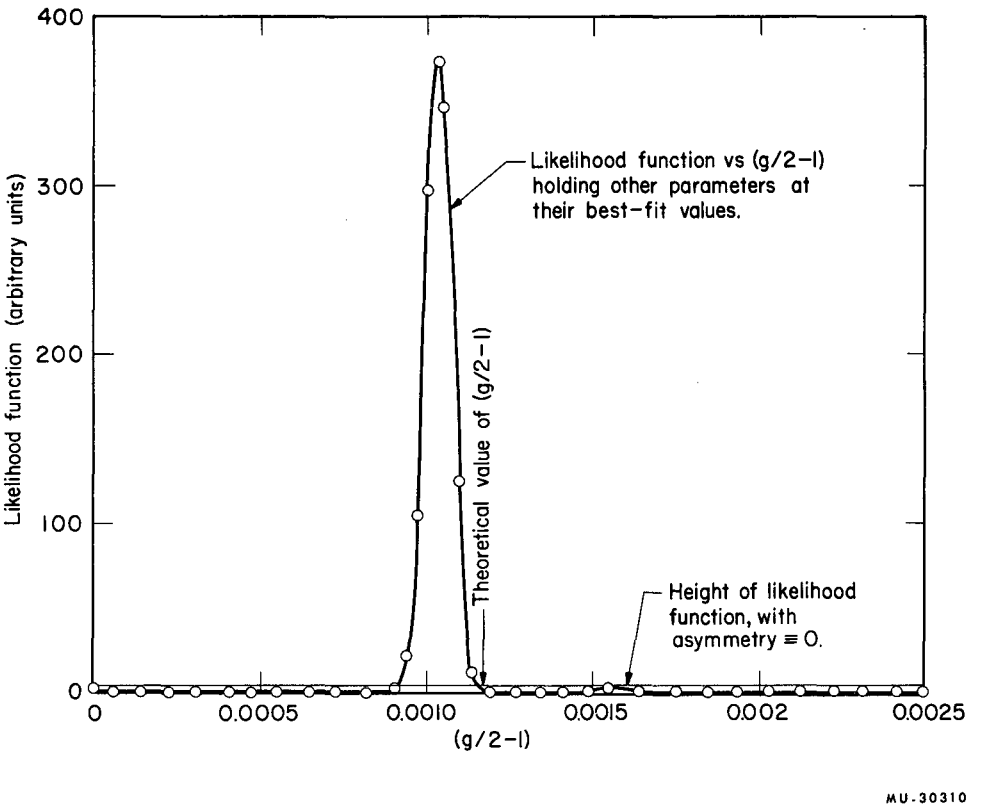

Fig. 30. Likelihood function for flip data.

plays a role. In this situation, the error in one parameter is not obtained from σ of the likelihood function when all other parameters are fixed. Figure 30, for example, shows a σ of about 5% in $(g-2)_\mu$; but varying the phase, B, causes the entire Gaussian to move back and forth. The error matrix gives the error as 11% in $(g-2)_\mu$ when this is taken into account.

The correlations among parameters are taken into account by the error matrix, and

$$\sigma_m \sigma_n \theta_{mn} = (H^{-1})_{mn}$$

where

$$H_{mn} = - \frac{\partial^2 W}{\partial A_m \partial A_n} \tag{46}$$

σ_m = error in determination of A_m^*

θ_{mn} = correlation between the A_m and A_n axes at $\mathcal{L} = \mathcal{L}_{max}$.

Therefore,

$$\sigma_m^2 = (H^{-1})_{mm} . \tag{47}$$

B. Experimental Results

The likelihood function for $(g-2)_\mu$, with the flip data used, is shown in Fig. 30. That systematic effects are not responsible for the peak is shown in Fig. 31, where the $(g-2)_\mu$ likelihood function for the no-flip data is compared to the flip likelihood function.

Initially it may seem odd that although the no-flip likelihood function wanders about the asymmetry = 0 line, the flip likelihood function does not. The explanation is that the best-fit asymmetry to the no flip data was very small. Thus the sine curve never gets outside the straight-line fit region, as shown in Fig. 32(a). In the flip case, however, the sine curve does make excursions outside the straight-line fit region [Fig. 32(b)], so that the sine fit is much worse than the straight-line fit except when its frequency and phase are just right.

The curve fitted to the data was

$$YF = T(1+A \sin X) \exp(-Dt), \tag{43}$$

where

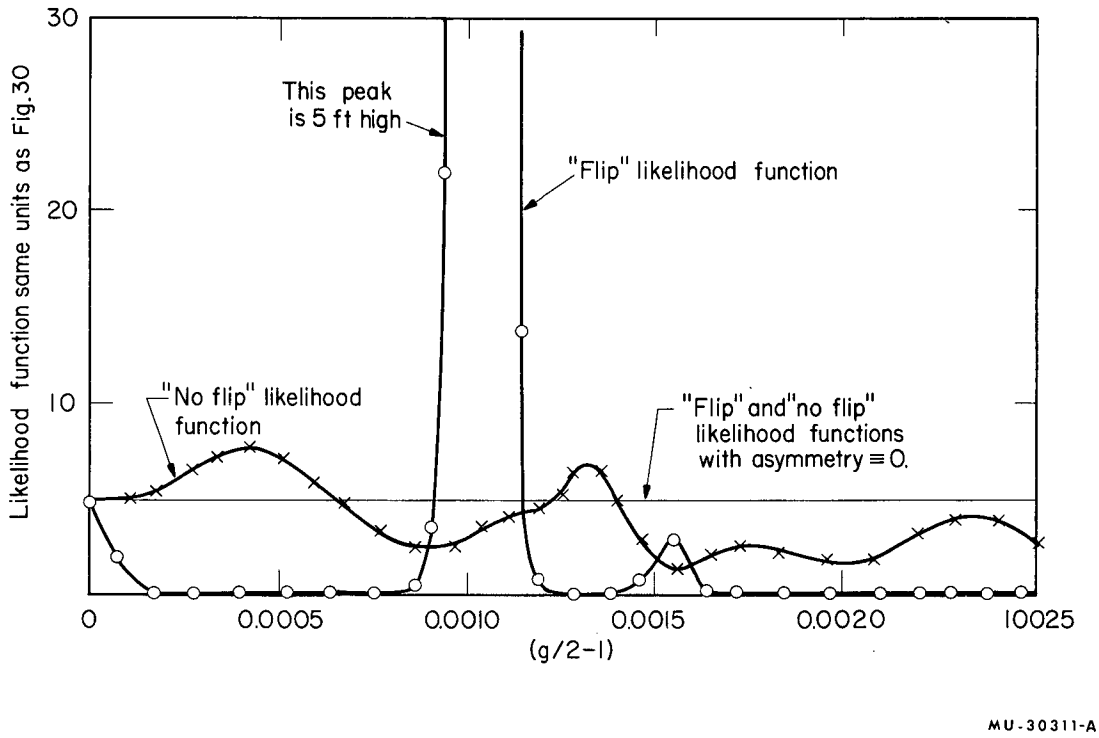

Fig. 31. Comparison of flip and no-flip likelihood functions.

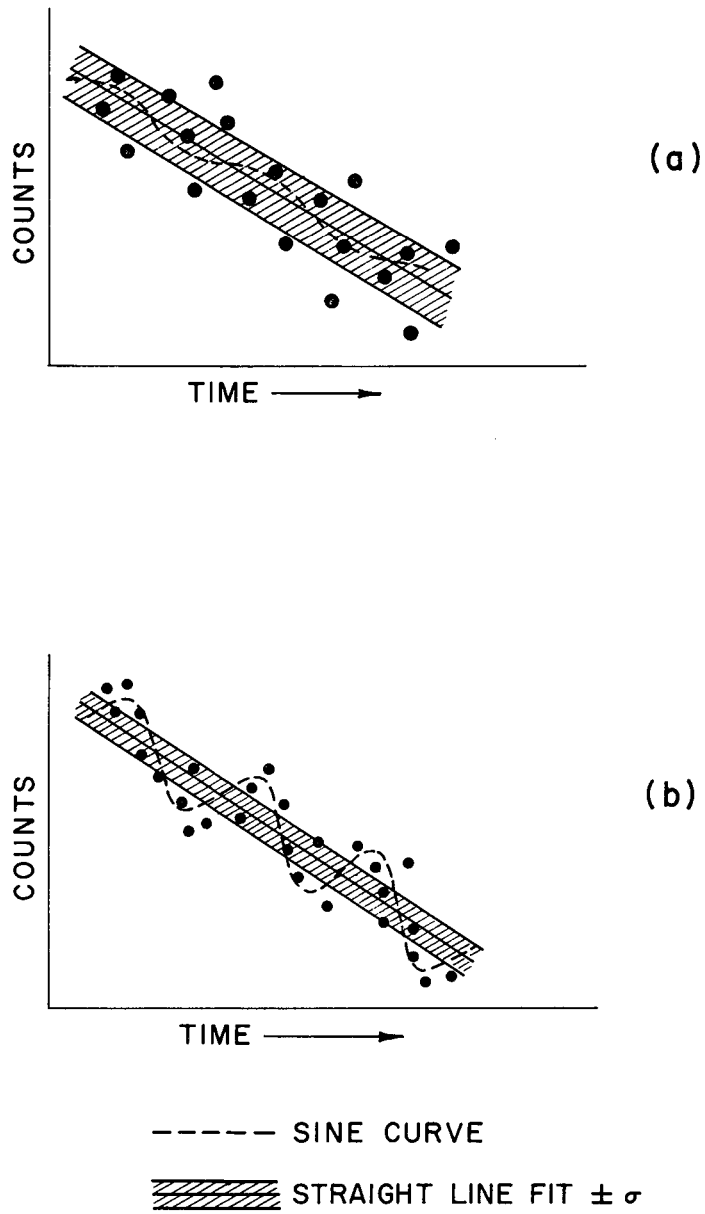

Fig. 32(a) Schematic representation of no-flip data
(b) Schematic representation of flip data.

YF = electron counts per channel of PHA

X = 2π Ft + B

t = time of flip pulse after muon entry (after μ_T) .

T = normalizing factor.

Fitting for all five parameters above, one obtains the results in Table VI.

Table VI. Best fit to final data.

A = 0.087 ± 0.031
B = - 1.25 ± 0.86 radians
F = 389.5 ± 40.3 kilocycles
T = 389.0 ± 13.0
D = 0.440 ± 0.014 μ sec^{-1}

The error in F is the statistical error in $(g-2)_\mu$. Much of this error is due to the fact that the initial phase B and the frequency F are rather strongly correlated. If the initial phase were precisely measured independently, it could be treated as a constant, and the determination of F would become considerably more precise. Therefore, an independent experiment was carried out to determine the properties of the polarized muon beam (Appendix A). The initial phase of the polarization was measured to an accuracy of about 2°; but unfortunately, this phase was found to be a function of the muon range. As differential range curves were obtained both in the $(g-2)_\mu$ run and in the beam study, we were tempted to equate the two curves. Because the $(g-2)_\mu$ run was carried out at the peak of the range curve, the correct initial phase would then be the one measured at the peak of the beam-study range curve. There are, however, two reasons for doubting the equality of the two curves. First, the $(g-2)_\mu$ range curve had a very different counter geometry and the measurements were made in a 28 kG field. Second, because less than 1% of the $(g-2)_\mu$ muons degraded to 40 MeV/c were trapped, the small fraction selected may have properties different from those of the whole 40-MeV/c population.

In the face of these difficulties, the initial phase could not be precisely determined, but was taken to be B = - 1.53 ± 0.24 radians. This is the median phase observed in the beam study (Appendix A). The error is half of the change in phase over the full width (at half maximum) of the muon-range curve in the beam study.

With this independent information on the initial phase, the best fit to the various parameters is given in Table VII.

Table VII. Best fit to final data with independent information on the initial phase.

A = 0.090 ± 0.031
B = - 1.53 ± 0.24 radians
F = 403.6 ± 23.8 kilocycles
T = 386 ± 13
D = 0.438 ± 0.014 μsec^{-1}

As discussed above

$$(g/2 - 1) = \frac{\omega_\Delta}{\omega_0} = \frac{\omega_\Delta m}{eB} \quad . \tag{48}$$

In terms of the fitted frequency F, this becomes

$$(g/2 - 1) = \frac{F}{e/m\ B} \quad , \tag{49}$$

where e/m is in kilocycles/gauss and B is in gauss.

The magnetic field of the solenoid was 28.2 ±0.2 kG. The ratio e/m for the muon is 13.5 kc/G. Using these values with that of F in Table VII, Eq. (49) yields:

$$(g/2 - 1) = 0.00106 \pm 0.000067 \ . \tag{50}$$

This value is 1.5 σ lower than the theoretical value and the CERN $(g-2)_\mu$ experimental result.

VI. CONCLUDING REMARKS

To within the accuracy of this experiment the energy of interaction between a 50-MeV/c muon and a static, uniform magnetic field is correctly given by quantum electrodynamics. To this accuracy, this experiment confirms, by a different method and with lower precision, the recent CERN results.

It is possible to discuss somewhat more quantitatively the bearing of the experimental result on the validity of QED at small distances (Refs. 32 through 36). There are many ways of introducing a cut-off length below which QED fails. One way is to replace the photon propagator $1/K^2$ with $(1/K^2) - [1/(K^2 + \Lambda^2)]$. The effect on $(g-2)_\mu$ of such a cutoff has been computed to be (Ref. 33)

$$(g-2)_\mu = \frac{a}{2\pi} \left[1 - \frac{2}{3} \left(\frac{\lambda_0}{\lambda_c} \right)^2 \right] , \qquad (51)$$

where $\lambda_0 \equiv$ the "cut-off" length $\equiv \frac{\hbar}{\Lambda}$

$\lambda_c \equiv$ the muon's Compton wavelength.

A second way is to express the anomalous moment as a dispersion integral, and then cut off the integral over the imaginary part at some upper limit Λ (Ref. 36). In this case,

$$(g-2)_\mu = \frac{a}{2\pi} \left[1 - 2 \left(\frac{\lambda_0}{\lambda_c} \right)^2 \right] . \qquad (52)$$

These two limits are presented in Table I along with the corresponding limits obtained from the CERN experiment.

The beautiful series of experiments on the electron by Crane et al. (Refs. 18 through 21), even though of much greater accuracy than the muon results, give less stringent cut-off lengths -- due to the smaller mass of the electron. From their work the photon propagator cut-off is $\lambda_0 \leq 2.3 \times 10^{-13}$ cm.

It would have been possible to have undertaken a second go-around with the apparatus. A factor of two or three improvement in accuracy should have been possible. In addition, a $(g-2)_\mu$ measurement for negative muons could also have been undertaken. However, in both cases more than just collecting electrons was involved. The HV storage condensors,

which were not satisfactory, continued to fail during the experiment. To replace these condensors and refurbish the gap took several hours. The HV gap itself required constant attention to keep its delay to a minimum -- as essential requirement. In addition, the vacuum system had two weak spots that were unceasing sources of trouble. Finally, as in all experiments with considerable electronic gear, there was the usual electronic lifetime (about a day here).

In summary, it took essentially the constant attention of the experimenters to keep the total apparatus running, and when the limit of endurance was reached, this initial phase of the experiment was over. To improve the reliability of the equipment to the point where 10 to 30 times as much data could be taken would have required several months of additional work on the gear and external circumstances did not permit it.

In light of our experience with this apparatus, we feel that an experiment along the lines of this one, performed at a "meson factory" accelerator, would have a reasonable chance of getting down to the 4th-order term in $(g-2)_\mu$. Several changes in design, as well as improvements on the existing design, would be desirable. The solenoid field could be increased by a factor of ≈ 3 using superconducting wire. This would result in a higher $(g-2)_\mu$ frequency and would also allow use of higher momentum muons. In our experiment both the electron background and the high-muon-loss figure are directly attributable to the necessity of degrading the incoming 150-MeV/c muons down to 50 MeV/c. The solenoid could be made considerably longer so that the mirror-closing problem would be eliminated and a higher mirror ratio could be used. The pulsed-mirror—fixed-mirror system should be replaced by a square-wave oscillator feeding both mirrors with the appropriate phases.

The possibility of GeV/c polarized muon beams at the new accelerators suggests taking advantage of the time-dilation factor. This advantage is a considerable one, but the solenoid type of apparatus described here is not suited to this possibility. No comparison of the relative merits of a GeV momentum type of experiment vs a solenoid type has been made.

ACKNOWLEDGMENTS

It is a pleasure to thank Professors M. G. White, W. Bleakney, Robert L. Thornton, and Kenneth M. Crowe for their continued support of this work, both financial and otherwise. Thanks are also due to James Vale, L. Hauser, L. Silvia, R. Walton, and all other members of the cyclotron crew for their excellent operation of the accelerator and their congenial and ingenious assistance with the experimental gear.

This work was done in part under the auspices of the U. S. Atomic Energy Commission.

APPENDICES

A. Polarization of Muons from In-Flight π Decay

The technique for producing a polarized muon beam in this experiment was to allow pions to decay in flight, and then to select the forward-decaying muons. To see why such a process should produce polarized muons, it is necessary to transform the muon spin from the pion (c.m.) frame to the laboratory frame.

Although spin may be defined relativistically in many ways, to avoid confusion we have adopted the definition given in Ref. 37. Suppose a muon is moving uniformly past an observer in some direction, and the observer states, "The spin is at an angle θ with respect to the muon velocity." This statement will be taken to mean that if the observer were accelerated in the direction of the muon velocity until he and the muon were in the same inertial frame, the observer would then say, "The spin is still at an angle θ with respect to the direction along which the muon was moving" (also the direction of the observer's acceleration).

In fact, the word "spin" has more connotations than are meant here. The problem is entirely classical, and the "muon with spin" can perfectly well be replaced by the "point compass" of the Thomas precession frame. The transformations derived here depend only on the properties of the Lorentz transformation.

From this starting point, the Lorentz transformation is all that is required to derive the spin transformations (Refs. 38-40). The peculiarities (to our Galilean senses) of the spin transformation follow from the fact that Lorentz transformations without rotations do not form a group.

In the center-of-mass (c.m.) system, the pion decay is very simple. A positive pion at rest decays into a positive muon and a neutrino; the muon and neutrino come off in opposite directions with spins pointing opposite their directions of motion. Thus the muon is 100% polarized in the pion rest frame.

According to the notation of E. P. Wigner (Ref. 38), the successive Lorentz transformations needed can be written out.

$$A(0,\phi) = \begin{bmatrix} 1 & 0 & 0 \\ 0 & \cosh\phi & \sinh\phi \\ 0 & \sinh\phi & \cosh\phi \end{bmatrix} \tag{53}$$

$A(0,\phi)$ is a Lorentz transformation producing a transformed coordinate system moving at $-V$ in the Z direction of the original system. The X axis is not needed and is suppressed throughout.

$$R(\theta) = \begin{bmatrix} \cos\theta & \sin\theta & 0 \\ -\sin\theta & \cos\theta & 0 \\ 0 & 0 & 1 \end{bmatrix} \tag{54}$$

Here $R(\theta)$ is a rotation operating on the unprimed system. It produces the primed system [Fig. 33(a)].

The direction in the YZ plane between Y and Z at an angle θ to Z is called the θ direction. Thus, the transformation that produces an unrotated system moving with velocity $-V$ in the θ direction is $R(\theta)\ A(0,\phi)\ R(-\theta) \equiv A(\theta,\phi)$.

We start in the muon rest frame, with the spin in the $-Z$ direction. The pion frame is obtained by the transformation $R(\theta)\ A(0,\phi_\mu)$. The muon now looks like Fig. 33(b), to an observer in the pion frame.

Now, the laboratory frame may be generated from the pion frame by $A(\pi/2, \phi_\pi)$. This defines the pion as travelling in the $+Y$ direction as seen by an observer in the laboratory frame. Thus, the overall transformation is $A(\pi/2, \phi_\pi)\ R(\theta)\ A(0, \phi_\mu)$. Explicit calculation gives for this transformation:

$$\begin{bmatrix} \cos\theta\cosh\phi_\pi & (\sin\theta\cosh\phi_\mu\cosh\phi_\pi + \sinh\phi_\mu\sinh\phi_\pi) & (\sin\theta\sinh\phi_\mu\cosh\phi_\pi + \cosh\phi_\mu\sinh\phi_\pi) \\ -\sin\theta & \cos\theta\cosh\phi_\mu & \cos\theta\sinh\phi_\pi \\ \cos\theta\sinh\phi_\pi & (\sin\theta\cosh\phi_\mu\sinh\phi_\pi + \sinh\phi_\mu\cosh\phi_\pi) & (\sin\theta\sinh\phi_\pi\sinh\phi_\mu + \cosh\phi_\mu\cosh\phi_\pi) \end{bmatrix} \tag{55}$$

But, for the spin to be parallel to the muon velocity, the observer's frame must be produced from the muon's rest frame by a transformation of the form $R(\theta)\ A(0,\phi)$:

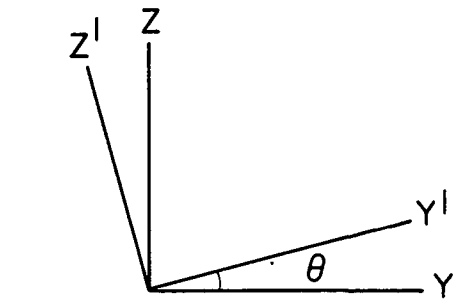

(a) R (θ) transformation

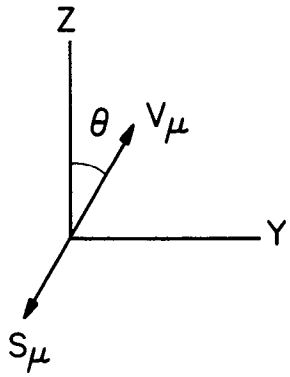

(b) Decay μ in π frame

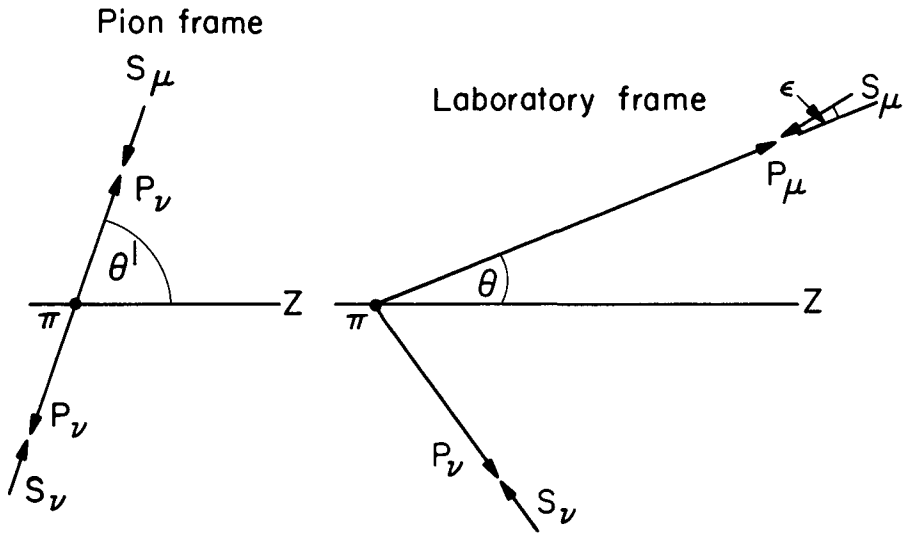

(c) Pion decay in pion and Laboratory frames of reference

MUB-8775

Fig. 33. Relativistic transformations of pion decay.
(a) R(θ) transformation.
(b) Decay μ in π frame.
(c) Pion decay in pion and laboratory frames of reference.

$$\begin{bmatrix} \cos\theta & \sin\theta\ \cosh\phi & \sin\theta\ \sinh\phi \\ -\sin\theta & \cos\theta\ \cosh\phi & \cos\theta\ \sinh\phi \\ 0 & \sinh\phi & \cosh\phi \end{bmatrix} \quad (56)$$

$A(\pi/2,\ \phi_\pi)\ R(\theta)\ A(0,\ \phi_\mu)$ can be put into the required form only by multiplying (in the group sense) from the right by $R(\epsilon)$, where

$$\tan\epsilon = \frac{\cos\theta\ \sinh\phi_\pi}{\sin\theta\ \cosh\phi_\mu\ \sinh\phi_\pi + \sinh\phi_\mu\ \cosh\phi_\pi} \quad (57)$$

$$= \frac{\cos\theta}{\gamma_\mu(\beta_\mu/\beta_\pi + \sin\theta)}$$

is easily verified by explicit calculation.

Thus, $A(\pi/2,\ \phi_\pi)\ R(\theta)A(0,\ \phi_\mu) = R(\theta')A(0,\ \phi')R\ (-\epsilon)$, (58)

so to an observer in the laboratory frame, the spin is rotated by ϵ counter-clockwise away from the muon velocity.

The expression for ϵ is readily converted into a more useful form, related to laboratory observables:

$$\tan\epsilon = \frac{\sin\theta'}{\gamma_\mu(\beta_\mu/\beta_\pi + \cos\theta')} \quad (59)$$

$$\tan\theta = \frac{\sin\theta'}{\gamma_\pi(\beta_\pi/\beta_\mu + \cos\theta')} , \quad (60)$$

where γ_μ, β_μ refer to the muon in the pion rest frame fixed by nature to be 1.04, 0.271 respectively, and γ_π, β_π refer to the pion in the laboratory frame. The pion travels in the +Z direction in the laboratory frame.

θ' = angle of muon's velocity in the pion rest frame with respect to the Z axis,

θ = angle of muon's velocity in the laboratory frame with respect to the Z axis,

ϵ = angle between muon spin, velocity in the laboratory frame.

The positive-pion decay in flight can be schematically represented as in Fig. 33(c).

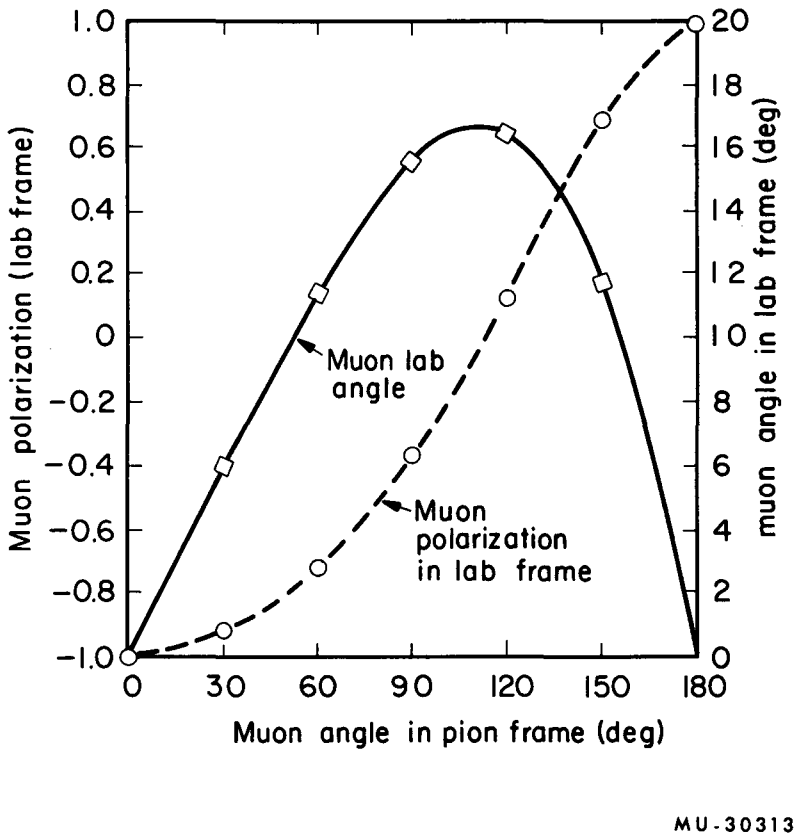

Fig. 34. Muon polarization from in-flight π decay. P_π = 137 MeV/c; P_μ max = 150 MeV/c.

Figure 34 summarizes the essential results for 137-MeV/c pions decaying in flight. The forward decay muons are polarized, as are the backward decaying muons. The forward decay muons have spins pointing opposite to their velocities, as in the pion rest frame.

Although the theoretical aspects of muon polarization from in-flight pion decay were quite clear, it was still necessary to determine experimentally the actual muon polarization produced by the optics system of Fig. 7. It is evident that the characteristics of the optics system (such as the angle of forward decay cone accepted) affect the polarization finally observed.

In order to measure muon-beam polarizations, a separate experiment was done. We were interested in the flux and polarization of various muon beams. The beam optics system used was that of the $(g-2)_\mu$ experiment.

Basically, the procedure was to stop the muons in carbon (which depolarizes the muon only slightly); the carbon was in a vertical 40-gauss magnetic field, which caused the muon spin to precess; the time distribution of decay electrons seen by a counter telescope in the horizontal plane of the muons then has the form

$$Y = T_p (1 + A \sin X) \exp(-Dt), \qquad (81)$$

where

Y = decay electrons seen at time t,

A = asymmetry (for 100% polarization, A = 0.33),

$X = 2\pi Ft + B$,

t = time after muon stops,

F = precession frequency $\propto$ g/m.

D = reciprocal of muon lifetime,

T_p = normalizing factor.

The equipment used is shown in Fig. 35. The Helmholtz coils were placed where the $(g-2)_\mu$ solenoid is shown in Fig. 7.

The muons enter the system through a small hole in the Pb shielding, as shown in Fig. 35. The signature of a stop in the carbon stopper is $S_1 S_2 \overline{S}_3$. This starts a time-to-pulse-height converter, which is stopped by the decay electron, $S_3 S_4 \overline{S}_0 \overline{S}_2$. The time-converter output goes to a

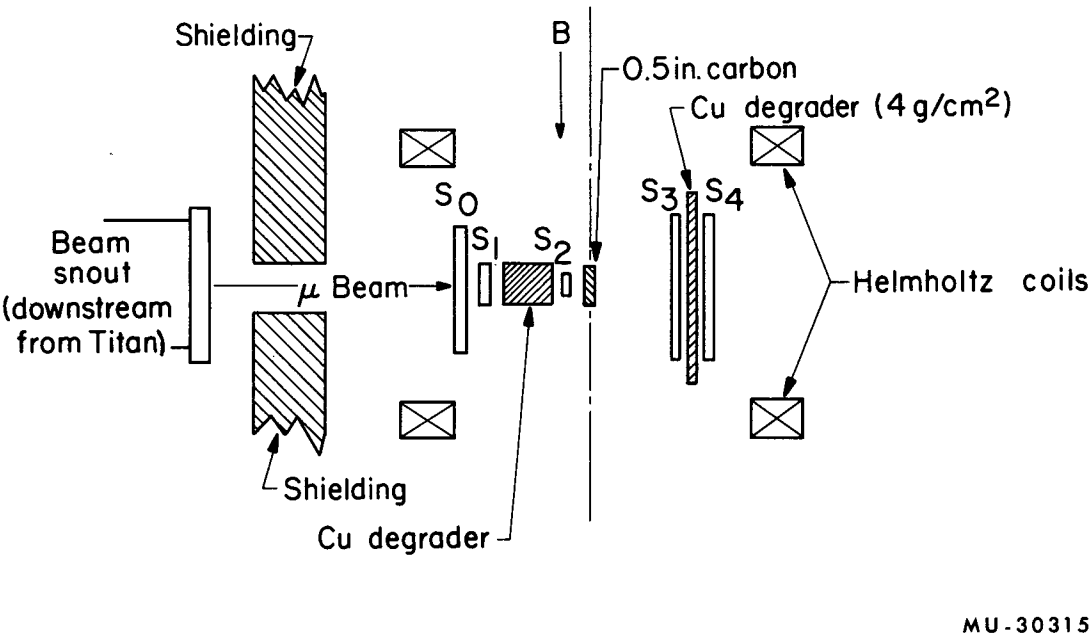

Fig. 35. Setup for measuring the initial phase of the (g-2) polarized muon beam.

pulse-height analyzer and is stored, giving rise to the decay electron-time distribution above. About two spin revolutions per lifetime are used.

The system was quite clean, thanks to the large anticounters $\overline{S}_0$ and $\overline{S}_3$. Backgrounds were low: typically, the decay electrons were observed for three lifetimes, with background at the end of three lifetimes being less than 5%.

The best polarization of μ^+ was found with the optics system set so that 135-MeV/c pions were accepted by Atlas, and 150-MeV/c forward-decay muons were accepted by Titan. The observed asymmetry (A) as defined above was 0.145; inasmuch as carbon depolarizes muons by $\approx 25\%$ (Ref. 41), the in-flight asymmetry was ≈ 0.20, and the polarization was therefore $\approx 60\%$.

An interesting feature of this polarized beam is that it is <u>not</u> polarized along its velocity, as one might expect. The reason is shown in Fig. 36. Immediately after Atlas there is a broad spread of pion momenta, with most of the pions being on the high-momentum side of the beam line (pion production is a sharply rising function of momentum at 135 MeV/c). These high-momentum pions do not have as far to decay as the 135-MeV/c pions do, but there are a lot of them. Such pions may produce 150-MeV/c muons by decaying not straight ahead, but off to the side somewhat, as shown in Fig. 36. Such a muon is polarized with its spin pointing largely to the beam's right. In fact, considering all 150-MeV/c muons from pion decay, it becomes clear that all the spins lie in the semicircle to the right of the beam.

The direction of the average polarization is found in fitting the initial phase [of Eq. (43)] to the decay-electron data. This was done for both signs of the Helmholtz magnetic field; the two phases so determined were consistent to within ≈ 2 degrees. We conclude that at the middle of the muon range, the average spin is in the horizontal plane and makes an angle of $102° \pm 2°$ with $\overline{V}$, rather than the expected angle of 180°. The phase depends on the range of the muons considered, however. Short-range muons are defined as the muons at the short-range half-maximum point of the differential range curve; long-range muons are defined as the muons at the long-range half-maximum point. With these definitions, short-range muons have an average spin angle of 107° with $\overline{V}$; long-range muons have an average spin angle of 80° with $\overline{V}$.

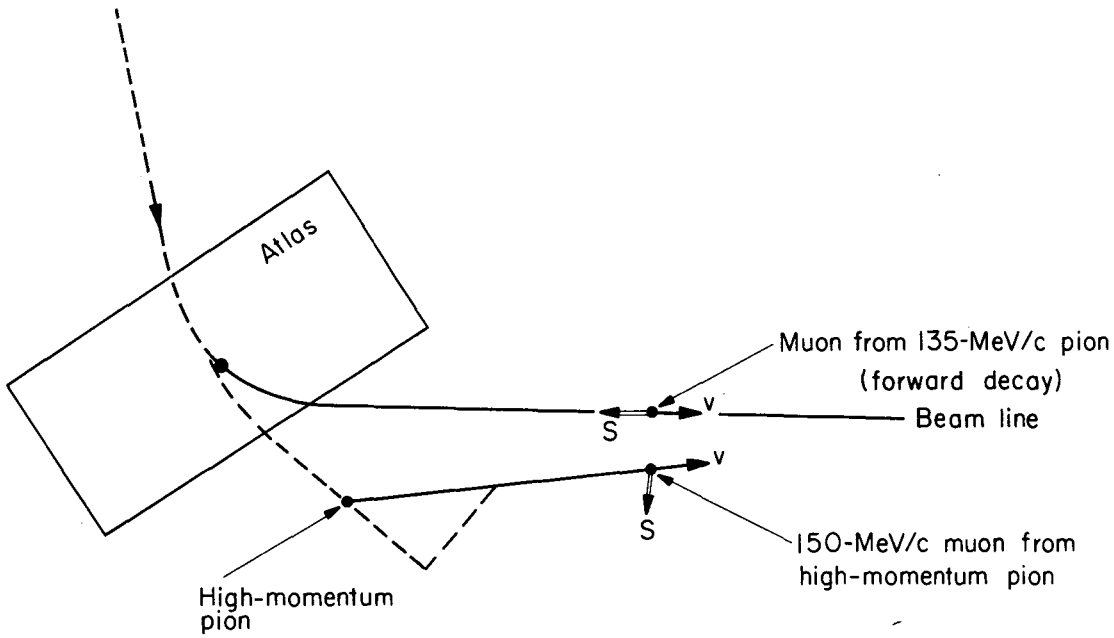

Fig. 36. Source of transverse muon polarization. Dashed line is pion flight path, and solid lines are muon flight paths.

The overall counting rates were as follows:

S_1S_2 = 2400 k/hour

$S_1S_2\bar{S}_3$ = 1800 k/hour (stopped in 1/2-inch thick carbon)

$S_3S_4\bar{S}_0\bar{S}_2$ = 170 k/hour

B. Error Matrix

The error matrix defined in Sec. V is derived in a straightforward way. The likelihood function may be Taylor expanded about A^*, and according to the notation of Sec. V.

$$\log(\mathcal{L}) = W(A) = W(A^*) + \sum_{m=1}^{M} \frac{\partial W}{\partial A_m}\bigg|_{A_m=A_m^*} \beta_m \qquad (62)$$

$$-1/2 \sum_{m,n} H_{mn}\beta_m\beta_n + \cdots ,$$

where

$$\beta_m = A_m - A_m^*$$

and

$$H_{mn} = -\frac{\partial^2 W}{\partial A_m \partial A_m}\bigg|_{A_m = A_m^*}$$

The second term vanishes, since at A^*, $\partial W/\partial A_m = 0$.

Therefore

$$\log \mathcal{L}(A) = W(A^*) - 1/2 \sum_{m,n} H_{mn}\beta_m\beta_n + \cdots . \qquad (63)$$

Neglecting higher order terms, we see that

$$\mathcal{L}(A) = C \exp(-1/2 \sum_{m,n} H_{mn}\beta_m\beta_n), \qquad (64)$$

which is an M-dimensional Gaussian. The validity of the error matrix rests on the assumption that the likelihood function is in fact approximately Gaussian. If the statistics are too poor for this to be so, the error matrix is on shaky ground.

Viewing the A_m as axes in parameter space, we wish to make a linear transformation that will diagonalize H, and make $\mathcal{L}(A)$ the product of M-independent one-dimensional Gaussians. In this new coordinate system, the new parameters (linear combinations of the old parameters) are not correlated, and the error in each is simply σ of the corresponding one-dimensional Gaussian. Therefore, let U be the unitary matrix that diagonalizes H.

$$U \cdot H \cdot U^{-1} = \begin{bmatrix} h_1 & & 0 \\ & h_2 & \\ 0 & & \ddots \\ & & & h_M \end{bmatrix} \equiv h \,, \tag{65}$$

where

$$\tilde{U} = U^{-1} \,.$$

The coordinate system is transformed according to

$$\gamma = \beta \cdot U^{-1} \,, \tag{66}$$

where γ_m are the new axes.

The differential element of probability in β space is

$$d^M P = C \exp\left[-\frac{1}{2} (\gamma \cdot U) \cdot H \cdot (\gamma \cdot U) \right] d^M\beta \,, \tag{67}$$

and since $\{|U| = 1\}$ is the Jacobian relating the volume elements $d^M\beta$ and $d^M\gamma$, we have in γ space

$$d^M P = C \exp\left\{ -\frac{1}{2} \sum_m h_m \gamma_m^2 \right\} d^M\gamma \,. \tag{68}$$

Now that the M dimensional Gaussian has been put in the form of the product of M-independent one-dimensional Gaussians,

$$\overline{\gamma_m \gamma_n} = \delta_{mn} h^{-1}{}_m = \Delta\gamma_m \Delta\gamma_n \,. \tag{69}$$

Therefore

$$\overline{\beta_m \beta_n} = \sum_{\ell,k} \overline{\gamma_\ell \gamma_k}\, U_{km} U_{\ell n}$$

$$= \sum_k U_{mk}\, h_k^{-1}\, U_{kn} \tag{70}$$

$$= (U^{-1} \cdot h \cdot U)_{mn} \,, \text{ and finally,}$$

$$\overline{(A_m - A_m^*)(A_n - A_n^*)} = (H^{-1})_{mn} , \tag{71}$$

where, as above,

$$H_{mn} = - \left. \frac{\partial^2 W}{\partial A_m \partial A_n} \right|_{A = A^*} . \tag{72}$$

As a simple example of this formula, consider the two-dimensional Gaussian

$$\mathcal{L} = C \exp \left\{ - \frac{1}{2} (x^2 + y^2) \right\} . \tag{73}$$

Here, $\mathcal{L}$ is the product of two independent one-dimensional Gaussians, and $x^* = y^* = 0$; $\Delta x = \Delta y = 1$. Suppose, however, that in the hypothetical experiment producing this $\mathcal{L}$, the desired parameters were x' and v, with $v = y/\sin\theta$, and $x' = x - v \cos\theta$. In other words, v is an axis at θ to x', and both axes have the same scale (no expansion or contraction) as before. From a physical point of view, it is clear that $\Delta x'$ and Δv should be larger than before since x' and v are more nearly degenerate, and, for $\theta = 0$, $\Delta x'$ and Δv are in fact infinite. However,

$$\mathcal{L}(v)\Big|_{x' = 0} = C \exp \left\{ - \frac{1}{2} v^2 \right\}$$

$$\mathcal{L}(x')\Big|_{v = 0} = C \exp \left\{ - \frac{1}{2} x'^2 \right\}, \tag{74}$$

and the unwary might conclude that $\Delta v = \Delta x' = 1$ again. But, the two-dimensional Gaussian is no longer a product of independent Gaussians:

$$\mathcal{L}(x', v) = C \exp \left\{ \frac{1}{2} (x'^2 + v^2 + 2 x' v \cos\theta) \right\} . \tag{75}$$

Therefore the error matrix must be used:

$$- \frac{\partial^2 W}{\partial x'^2} = - \frac{\partial^2 W}{\partial v^2} = + 1; \quad - \frac{\partial^2 W}{\partial x' \partial v} = + \cos\theta .$$

So:

$$H_{mn} = \begin{bmatrix} 1 & \cos\theta \\ \cos\theta & 1 \end{bmatrix} \tag{76}$$

and

$$(H^{-1})_{mn} = \frac{1}{(1-\cos^2\theta)} \begin{bmatrix} 1 & -\cos\theta \\ -\cos\theta & 1 \end{bmatrix} . \qquad (77)$$

Thus we conclude that $\Delta v = \Delta x' = 1/\sin\theta$. Note that $(H)^{-1}_{12} = (\Delta x)\,(\Delta x')\cos\theta$, where θ is the angle between axes in parameter space.

When the various parameters are independent, "outside" precise knowledge of one of the parameters will not improve the accuracy of remaining parameters. However, if the correlation among parameters is strong, then knowledge of the exact value of a parameter may markedly improve the accuracy of the remaining parameters. In the example above, suppose that $\theta = 6°$ [note that the angle may be found by observing the x', v correlation, $(H)^{-1}_{12}$]. Suppose further that an experiment has yielded $x' = 0 \pm 10$, $v = 0 \pm 10$. If an independent determination of x' is possible, so that $x' = 0 \pm \epsilon$ (where $\epsilon << 10$), then the experimental data may be fitted by varying v alone, and one would improve the accuracy 10 times: $v = 0 \pm 1$.

In more than two dimensions, the situation is not so easily visualized geometrically. In three dimensions, for example, let X, Y, Z be orthogonal axes, and let $W = 1/2\,(X^2 + Y^2 + Z^2)$. Suppose we are interested in the parameters:

$$\begin{aligned} X' &= X - Y'\cos\theta \\ Y' &= (Y - Z'\cos\phi)/\sin\theta \\ Z' &= Z/\sin\phi\ , \end{aligned} \qquad (78)$$

where

X' axis coincides with X axis

Y' axis is in the XY plane, at an $\measuredangle\,\theta$ to X.

Z' axis is in the YZ plane, at an $\measuredangle\,\phi$ to Y.

The error matrix may be computed, as above, to be:

$$\frac{1}{\sin^2\theta\sin^2\phi} \begin{bmatrix} 1 - \sin^2\theta\cos^2\phi & -\cos\theta & \sin\theta\cos\theta\cos\phi \\ -\cos\theta & 1 & -\sin\theta\cos\phi \\ \sin\theta\cos\theta\cos\phi & -\sin\theta\cos\phi & \sin^2\theta \end{bmatrix} . \qquad (79)$$

Note that, although $X' \perp Z'$, the X', Z' correlation is not zero, unless $X' \perp Y'$ also. Furthermore, as $\phi \to 0$, $\Delta X' \to \infty$ unless $X' \perp Y'$. Thus it could be said that X' is correlated to Z' through Y', even though $X' \perp Z'$.

C. Computer Programs for Data Analysis

The data were analyzed on an IBM 650 computer with Fortran programs. Thus only minor modifications would be required for the programs to be used on other computers (e.g., the addition of FORMAT statements). The programs included here are:

RAWFIT II
MACHINE SWEEP RAWFIT
ERROR MATRIX II
N BY N MATRIX INVERSION

All but the matrix-inversion program are applicable only when the curve being fitted to the data has the form

$$Y_F = T_p (1 + A \sin X) \exp(-Dt) \qquad (61)$$

where $X = (Ft + B)$, t is the independent variable, and T_p, A, F, B, and D are parameters to be fitted to the data.

The programs are discussed in the above order.

1. RAWFIT II

RAWFIT II computes chi squared and the likelihood function, given curve parameters and experimental data. As many as 64 experimental points may be accommodated.

Input Data

N = number of experimental points to be used.
YEXP (I) = experimentally observed value at point I.
SIG (I) = estimated error in YEXP (I).
TIME (I) = time at point I (TIME is the independent variable in the function to be fitted).

TCON
A
BETA
TAU
TOP
TNAP

} = parameters in the curve to be fitted to the YEXP (I):

YFIT = TOP* (1.0 + A* SINF (X))* EXPEF (-TIME(I)/TNAP), (80)

where

X = ((TIME (I) + TCON)/TAU)* 6.2832 + BETA . (81)

Output Data

"Final data" is punched out according to statements 42 and 43.

L = dummy, useful for sorting final data from intermediate data.

SSQD = chi squared.

PPRO = exp (-1/2 SSQD); proportional to the likelihood function.

PACT = likelihood function.

BPPRO = PPRO multiplied by a weight function; not of general interest.

The six curve-fitting parameters are also punched out.

"Intermediate data" is punched according to statement 30.

I indicates that the Ith experimental point is concerned.

YFIT = value of the fitted curve at the Ith point.

SQD = square of the difference YFIT - YEXP (I) in units of SIG (I).

General Operation

The input data are prepared in the following way: N is followed by TCON, after which come the experimental data punched on N cards, with each card containing one set of (YEXP (I), SIG (I), TIME (I)). Next, on any number (M) of cards, M sets of the five parameters in statement 20 are punched.

The computer then calculates the appropriate quantities for one set of the statement-20 parameters, then returns to do the next set, and so on, until all M sets are finished.

In compilation of the program, a subroutine for evaluation of sin(X) must be included.

```
C00000 RAWFIT II
C00000
      20 DIMENSION YEXP(64), SIG(64),
      21 TIME(64)
      40 READ, N
         READ,TCON
      60 DO 8   I=1,N
      80 READ, YEXP(I), SIG(I),
      81 TIME(I)
     100 PSIG=1.0
     120 DO 14  I=1,N
     140 PSIG=PSIG*SIG(I)
     160 CONTINUE
     180 L=300
     200 READ,A,BETA,TAU,TOP,TNAP
     220 SSQD=0.0
     240 DO 32   I=1,N
         T       =TIME(I)+TCON
     250 X=(T       /TAU)*6.2832+BETA
     260 YFIT=TOP*(1.0+A*SINF(X))*
     261 EXPEF(-TIME(I)/TNAP)
     280 SQD=((YEXP(I)-YFIT)/SIG(I))
     281 **2
     300 PUNCH,I,A,BETA,TAU,YFIT,SQD
     320 SSQD=SSQD+SQD
     340 CONTINUE
     360 PPRO=EXPEF(-0.5*SSQD)
     400 PACT=PPRO/((PSIG)*(2.5067)
     401 **N)
     420 PUNCH,L,SSQD,PPRO,PACT
     421 ,A,BETA,TAU
    1000 BPPRO=PPRO*EXPEF(-0.5*
    1001 (BETA/0.35)**2.0)
     430 PUNCH, L, TOP, TNAP ,BPPRO
     431 ,TCON
     440 GO TO 20
     460 END
```

2. MACHINE SWEEP RAWFIT

This program does essentially what RAWFIT II does, the major difference being that in this program the computer varies the curve parameters to be fitted, searching for the best fit. It optimizes each parameter in turn, and then reoptimizes, using smaller steps in parameter values. It continues this cycling until turned off by the operator. However, there is a major disadvantage. Because of the nonlinear way in which the parameters enter the curve to be fitted, the computation may converge to some insignificant local maximum in the likelihood function (a local minimum in chi squared), unless the initial values of the parameters read into the computer are fairly close to the true optimum values. If a general picture of the entire likelihood function is desired, then of course RAWFIT II is again the program to use.

As many as 150 experimental points may be used in MACHINE SWEEP RAWFIT. This program, suited to the analysis of PHA—stored-time distributions, makes some adjustment for nonlinearities in the time-converter—PHA system. Long times are assumed to be in low channels. The input-data format allows the PHA (if RIDL or Victoreen or similar machine) read-out to be converted directly into input-data cards (e. g. , Tally-Tape to card conversion, with no operator punching required). The statistical error in a given channel is assumed to be the square root of the stored number. A background term is included in the curve to be fitted.

Input Data

N = number of experimental points to be used.

CH (I) = channel number (of PHA) of Ith experimental.

YEXP (I) = experimental value stored in CH (I).

CN0 - CN6 = seven channel numbers (usually fractional), which are separated by 1-μsec intervals, where CN0 > CH (I) MAX, and CN6 < CH (I) MIN.

A (1)
A (2)
A (3)
A (4)
A (5)
A (6)
TC
} parameters in the curve to be fitted to the YEXP (I):

$$YF = A(4) * (1.0 + A(1) * SINF(X)) * EXPEF(-A(5) * T) + A(6) \qquad (82)$$

where

X = A (3) * T + A (2)

T = TT (I) + TC = TIME of Ith point (computed).

D (1), D (2), D (3), D (4), D (5), D (6) — initial increments of parameters to be used by the computer in sweeping parameter space for the best-fit point. D (I) is the increment corresponding to A (I).

TC = time at channel CN0 .

BUG = - (any number) for diagnostic punches,
+ (any number) for no diagnostic punches.

R = factor by which the D (1) are decreased after a (6) optimization.

J = index of A (J); optimization starts with A (J).

Output Data

Statement 155 punches the experimental input data, and the computed YM (I) and TT (I).

YM (I) = modification of YEXP (I) due to the time-converter—PHA nonlinearity.

TT (I) = time interval from CN0 to CH (I) .

Statement 214 punches various "internal" information; used for debugging.

Statements 301 - 306 punch final output data.

L = 1 + (number of reversals in direction of sweep in A (J) in looking for max).

A = all of the A (I).

J = shows which A (J) is being optimized.

D = all of the A (I) increments.

K = 1 on first computation of chi squared, 2 thereafter.

SCQ = chi squared at A.

SCQI = best (lowest) previous chi squared.

General Operation

Input data are prepared in the following way:
N is followed by the experimental data punched on N cards, with one set of (CH(I), YEXP (I)) per card. Next follows one card, with CN0 - CN6. Finally come the three last cards: A (1) - A (6) on the first; D (1) - D (6) on the second; and TC, BUG, R, J on the last.

The computer first computes and stores the YM (I) and TT (I), then begins computation of chi squared and the search for its minimum. The computer first optimizes A (J), then goes on to A (J + 1). After optimizing A (6), it reduces the D (I) by the factor R, and starts optimizing A (1). The machine continues through this cycle until turned off.

A subroutine for the evaluation of sin (X) must be provided in the compilation of the program.

3. ERROR MATRIX II

ERROR MATRIX II computes the matrix H_{mn} for the parameters A, BETA, FREQ, TOP, and DKRQ, where the fitted curve is

YFIT = TOP* (1.0 + A* SINF (X) * EXPEF (-DKFRQ TIME (I))) , (83)

where

X = 6.283185*FREQ*T + BETA

and

T = TIME (I) + TCON .

The program can accommodate up to 64 experimental points; it assumes that the statistical error in YEXP (I) is just $(\text{YEXP (I)})^{1/2}$. SIG (I) plays no role in the calculation.

The output matrix H_{mn} must be inverted before it yields any information on the errors in the parameter determination.

```
C00000 MACHINE SWEEP RAWFIT
C00000
      10 DIMENSION CH(150),YEXP(150),
      11 A(6),D(6),YM(150),TT(150)
      20 READ,N
      40 DO 6 I=1,N
      60 READ,CH(I),YEXP(I)
      80 READ,CN0,CN1,CN2,CN3,CN4,CN5,
      81 CN6
     160 DO 155 I=1,N
    1000 IF(CN1-CH(I))101,110,110
    1010 TT(I)
    1011    =(CN0-CH(I))/(CN0-CN1)
    1030 YM(I)=YEXP(I)
    1050 GO TO 155
    1100 IF(CN2-CH(I))111,120,120
    1110 TT(I)
    1111    =(CN1-CH(I))/(CN1-CN2)+1.0
    1130 YM(I)=YEXP(I)*(CN1-CN2)/
    1131 (CN0-CN1)
         GO TO 155
    1200 IF(CN3-CH(I))121,130,130
    1210 TT(I)
    1211    =(CN2-CH(I))/(CN2-CN3)+2.0
    1230 YM(I)=YEXP(I)*(CN2-CN3)/
    1231 (CN0-CN1)
         GO TO 155
    1300 IF(CN4-CH(I))131,140,140
    1310 TT(I)
    1311    =(CN3-CH(I))/(CN3-CN4)+3.0
    1330 YM(I)=YEXP(I)*(CN3-CN4)/
    1331 (CN0-CN1)
         GO TO 155
    1400 IF(CN5-CH(I))141,150,150
    1410 TT(I)
    1411    =(CN4-CH(I))/(CN4-CN5)+4.0
    1430 YM(I)=YEXP(I)*(CN4-CN5)/
    1431 (CN0-CN1)
         GO TO 155
    1500 TT(I)
    1501    =(CN5-CH(I))/(CN5-CN6)+5.0
    1530 YM(I)=YEXP(I)*(CN5-CN6)/
    1531 (CN0-CN1)
         GO TO 155
    1550 PUNCH,I,CH(I),YEXP(I),YM(I),
    1551 TT(I)
     100 READ,A
     110 READ,D
     120 READ,TC,BUG,R,J
    5020 K=1
    5040 L=1
     130 SGN=+1.0
     140 SCQ=0.0
    1600 DO 250 I=1,N
    2000 SIG=YEXP(I)**(-0.5)*YM(I)
    2020 T=TT(I)+TC
    2040 X=A(3)*T+A(2)
    2060 YF=A(4)*(1.0+A(1)*SINF(X))*
```

```
2080 CQ=((YF-YM(I))/SIG)**2
2100 SCQ=SCQ+CQ
2120 IF(BUG)214,250,250
2140 PUNCH,I,CH(I),YEXP(I),YM,YF,
2141 SIG,CQ,I,SCQ,TT(I),T
2500 CONTINUE
3010 PUNCH,L
3020 PUNCH,A,J
3040 PUNCH,D,K
3060 PUNCH,SCQ,SCQI,L,R
4000 IF(K-2)402,410,410
4020 SCQI=SCQ
4040 A(J)=A(J)+SGN*D(J)
4060 K=2
4080 GO TO 14
4100 IF(SCQI-SCQ)418,412,412
4120 A(J)=A(J)+SGN*D(J)
4140 SCQI=SCQ
4160 GO TO 14
4180 SGN=-SGN
4200 A(J)=A(J)+2.0*SGN*D(J)
4220 L=L+1
4240 IF(L-3)426,430,430
4260 GO TO 14
4300 L=1
4310 A(J)=A(J)-SGN*D(J)
4320 IF(J-6)434,440,440
4340 J=J+1
4360 A(J)=A(J)+SGN*D(J)
4380 GO TO 14
4400 J=1
4420 DO 444 KK=1,6
4440 D(KK)=D(KK)/R
4460 A(J)=A(J)+SGN*D(J)
4480 GO TO 14
4500 END
```

Input Data

N = number of experimental points used.

YEXP (I) = experimentally observed value at point I.

SIG (I) = arbitrary number.

TIME (I) = time at point I (time is the independent variable in the fitted curve).

TCON = constant time interval = physical time at I = 1.

A, BETA, FREQ, TOP, DKFRQ = values of fitted parameters (fitted in RAWFIT II or MACHINE SWEEP RAWFIT).

Output Data

Much internal data is punched out, but the error matrix itself is punched out row by row, one element per card on 25 cards in statement number 1007. Each card has three words: H (I, J); I; and J. The final output card contains the set of parameters A - DKFRQ for which the matrix is computed. Thus, the last 26 cards punched have the error matrix and its associated parameter values.

General Operation

The input data are prepared in the following way: N is followed by TCON, and then follow N cards with one set of (YEXP(I), SIG (I), TIME (I)) on each card. Last are the A - DKFRQ parameters, any number of sets, one set per card.

The computer computes the error matrix associated with each set of A - DKFRQ, until all sets are finished.

With this program, a predicted error matrix may be obtained before data are taken. For this, simply compute YFIT at the I points where data will be taken, and use the expected A - DKFRQ parameters. Then use these YFIT values as YEXP (I). The resultant matrix is what one would obtain by averaging the matrices of many experimental runs, and is the best prediction possible.

A subroutine for evaluation of sin(X) and cos(X) must be included.

```
C00000 ERROR MATRIX II (NOT INVERTED)
C00000
      50 DIMENSION YEXP(64),SIG(64),
      51 TIME(64),H(5,5)
     100 READ,N
     110 READ,TCON
     150 DO 20 I=1,N
     200 READ,YEXP(I),SIG(I),TIME(I)
     250 READ,A,BETA,FREQ,TOP,DKFRQ
    5000 DO 506 I=1,5
    5020 DO 504 J=I,5
    5040H(I,J)=0.0
    5060 CONTINUE
     300 DO  899 I=1,N
     310 T=TIME(I)+TCON
     350 X=6.283185*FREQ*T       +BETA
     400 SSS=SINF(X)
     450 CCC=COSF(X)
     500 EEXP=EXPEF(-DKFRQ*TIME(I))
     550 YFIT=TOP*(1.0+A*SSS)*EEXP
     600 DIFF=(YFIT)-(YEXP(I))
     650 PUNCH, I,X,SSS,CCC,EEXP,YFIT
     660 PUNCH,YEXP(I),DIFF
    8000 H(1,1)=H(1,1)+(1.0/YEXP(I))*
    8001 (TOP*SSS*EEXP)**2.0
    8010 PUNCH,I,H(1,1)
    8050 H(1,2)=H(1,2)+(1.0/YEXP(I))*
    8051 (DIFF+TOP*A*SSS*EEXP)*EEXP*
    8052 TOP*CCC
    8060 PUNCH,I,H(1,2)
    8100 H(1,3)=H(1,3)+(1.0/YEXP(I))*
    8101 (DIFF+TOP*SSS*EEXP*A)*TOP*
    8102 6.283185*T       *CCC*EEXP
    8110 PUNCH,I,H(1,3)
    8150 H(1,4)=H(1,4)+(1.0/YEXP(I))*
    8151 (DIFF+YFIT)*SSS*EEXP
    8160 PUNCH,I,H(1,4)
    8200 H(1,5)=H(1,5)+(1.0/YEXP(I))*
    8201 (DIFF+YFIT)*TOP*SSS*(-TIME(I)
    8202 )*EEXP
    8210 PUNCH,I,H(1,5)
    8250 H(2,2)=H(2,2)+(1.0/YEXP(I))*
    8251 (DIFF*TOP*A*(-SSS)*EEXP+(TOP
    8252 *A*CCC*EEXP)**2.0)
    8260 PUNCH,I,H(2,2)
    8300 H(2,3)=H(2,3)+(1.0/YEXP(I))*
    8301 (-DIFF*SSS+TOP*A*CCC*CCC*EEXP
    8302 )*TOP*A*6.283185*T       *EEXP
    8310 PUNCH,I,H(2,3)
    8350 H(2,4)=H(2,4)+(1.0/YEXP(I))*
    8351 (DIFF+YFIT)*A*CCC*EEXP
    8360 PUNCH,I,H(2,4)
    8400 H(2,5)=H(2,5)+(1.0/YEXP(I))*
    8401 (DIFF+YFIT)*TOP*A*CCC*EEXP*
    8402 (-TIME(I))
    8410 PUNCH,I,H(2,5)
    8450 H(3,3)=H(3,3)+(1.0/YEXP(I))*
    8451 (DIFF*TOP*A*(6.283185*T
    8452 )**2.0*(-SSS)*EEXP+(TOP*A*
```

```
     8453 6.283185*T       *CCC*EEXP)**
     8454 2.0)
     8460 PUNCH,I,H(3,3)
     8500 H(3,4)=H(3,4)+(1.0/YEXP(I))*
     8501 (DIFF+YFIT)*A*6.283185*T
     8502     *CCC*EEXP
     8510 PUNCH,I,H(3,4)
     8550 H(3,5)=H(3,5)+(1.0/YEXP(I))*
     8551 (DIFF+YFIT)*TOP*A*6.283185*
     8552 (-TIME(I))*T       *CCC*EEXP
     8560 PUNCH,I,H(3,5)
     8600 H(4,4)=H(4,4)+(1.0/YEXP(I))*
     8601 ((1.0+A*SSS)*EEXP)**2.0
     8610 PUNCH,I,H(4,4)
     8650 H(4,5)=H(4,5)+(1.0/YEXP(I))*
     8651 (DIFF+YFIT)*(1.0+A*SSS)*
     8652 (-TIME(I))*EEXP
     8660 PUNCH,I,H(4,5)
     8700 H(5,5)=H(5,5)+(1.0/YEXP(I))*
     8701 (DIFF*TOP*(1.0+A*SSS)*TIME(I)
     8702 **2.0*EEXP+(YFIT*TIME(I))**
     8703 2.0)
     8710 PUNCH,I,H(5,5)
     8990 CONTINUE
    10000 DO 1009 I=1,5
    10010 DO 1007 J=1,5
    10030 IF (I-J) 1007,1007,1005
    10050 H(I,J)=H(J,I)
    10070 PUNCH,H(I,J),I,J
    10090 CONTINUE
    10110 PUNCH,A,BETA,FREQ,TOP,DKFRQ
    11110 GO TO 25
     2050 END
```

4. N BY N MATRIX INVERSION

This program was written to invert the error matrix, but works on any square matrix up to a 9 by 9. Larger matrices could be provided for if the COMPUTED GO TO were given more branches.

Input Data

A, BETA, FREQ, TOP, DKFRQ — These constants play no role in the program, and may be punched with any identifying information.

N = order of the N BY N matrix.

H (I) = elements of the matrix to be inverted, in row-by-row order, one element per card.

Output Data

Statement 445 punches the elements H (I) of the original matrix, the index I, and the elements G (I) of the inverted matrix, row by row, on N^2 cards.

Next, the A - DKFRQ identification is punched.

General Operation

In order to store the matrices properly (where N is variable), it was necessary to give the matrices the single index I. $1 \leq I \leq N^2$. This should cause no trouble; all matrices are read and punched row-wise, one element per card.

The program fails if any diagonal matrix element is zero in the matrix to be inverted. In practice, such a matrix may still be handled, simply by replacing diagonal zeroes by ϵ, where $\epsilon = 10^{-20}$ x (smallest nonzero element). The program also fails if det H = 0, since the matrix is then singular.

The program will invert any number of matrices, returning after each inversion to statement 6 to read A - DKFRQ and start the next inversion.

```
C00000 N BY N MATRIX INVERSION
C00000
     50 DIMENSION G(81 ),B(9),H(81 )
     60 READ,A,BETA,FREQ,TOP,DKFRQ
     70 READ,N
     80 NN=N*N
   3010 DO 345 I=1,NN
   3450 READ, H(I  )
    150 DO 35 I=1,NN
    250 G(  I)=H(I  )
    350 CONTINUE
    430 PUNCH,N
   2000 GO TO  (201,202,203,204,205,
   2001 206,207,208,209),N
   2010 KK=0100010101
        GO TO 40
   2020 KK=0200020101
        GO TO 40
   2030 KK=0300030101
        GO TO 40
   2040 KK=0400040101
        GO TO 40
   2050 KK=0500050101
        GO TO 40
   2060 KK=0600060101
        GO TO 40
   2070 KK=0700070101
        GO TO 40
   2080 KK=0800080101
        GO TO 40
   2090 KK=0900090101
    400 KKK=XMIRF(KK)
   4010 DO 445 I=1,NN
   4450 PUNCH,H(I  ),I,  G(  I)
   1000 PUNCH,A,BETA,FREQ,TOP,DKFRQ
    570 GO TO 6
    600 END
```

The program must have a matrix inversion subroutine (here called by XMIRF (KK)) built in during compilation.

D. Spin Flip for Nonconcentric Orbits

In the design of this experiment, spin flip of muons in nonconcentric orbits was a matter of some concern. If the amount of flip were found to depend strongly on the eccentricity of the muon orbits, the effect would be to decrease the observed (g-2) asymmetry. Fortunately, it turns out that the spin-flip angle is essentially independent of the eccentricity, as long as the orbit encircles the center flip rod, and as long as the flip pulse is adiabatic (slowly varying in time) with respect to the muon's cyclotron period.

To the extent that the flip pulse is adiabatic, we may simply consider one complete cyclotron revolution of the muon, during which B_{flip} is nearly constant. It can be shown that B_{flip} as seen by the muon is not a function of the orbit eccentricity.

To see this, consider a muon orbit of radius r, and let it be off center by a, as shown in Fig. 37.

It is most convenient to use a coordinate system where the muon orbit is centered, and the solenoid flip-pulse rod is off center. First, note that $\overline{B_{flip}}$ over $0 \leq \theta \leq 2\pi$ is in fact azimuthal; by symmetry $(\overline{B_{flip}})_r$ for $0 \leq \theta \leq \pi = -(\overline{B_{flip}})_r$ for $\pi \leq \theta \leq 2\pi$, so that over the whole circle, $(\overline{B_{flip}})_r = 0$. Thus we have only to compute $(\overline{B_{flip}})_\theta$ over the orbit. If we define $B_{flip} \equiv B/P$, we have, for a concentric orbit (a = 0),

$$(\overline{B_{flip}})_\theta = \frac{B}{r} \quad . \tag{84}$$

For a nonconcentric orbit,

$$(\overline{B_{flip}})_\theta = \frac{1}{\pi} \int_0^\pi \frac{B}{P} \cos\beta \, d\theta \quad . \tag{85}$$

Expressing P and β in terms of the single variable θ, we obtain

$$P^2 = a^2 - 2ar\cos\theta + r^2 \tag{86}$$

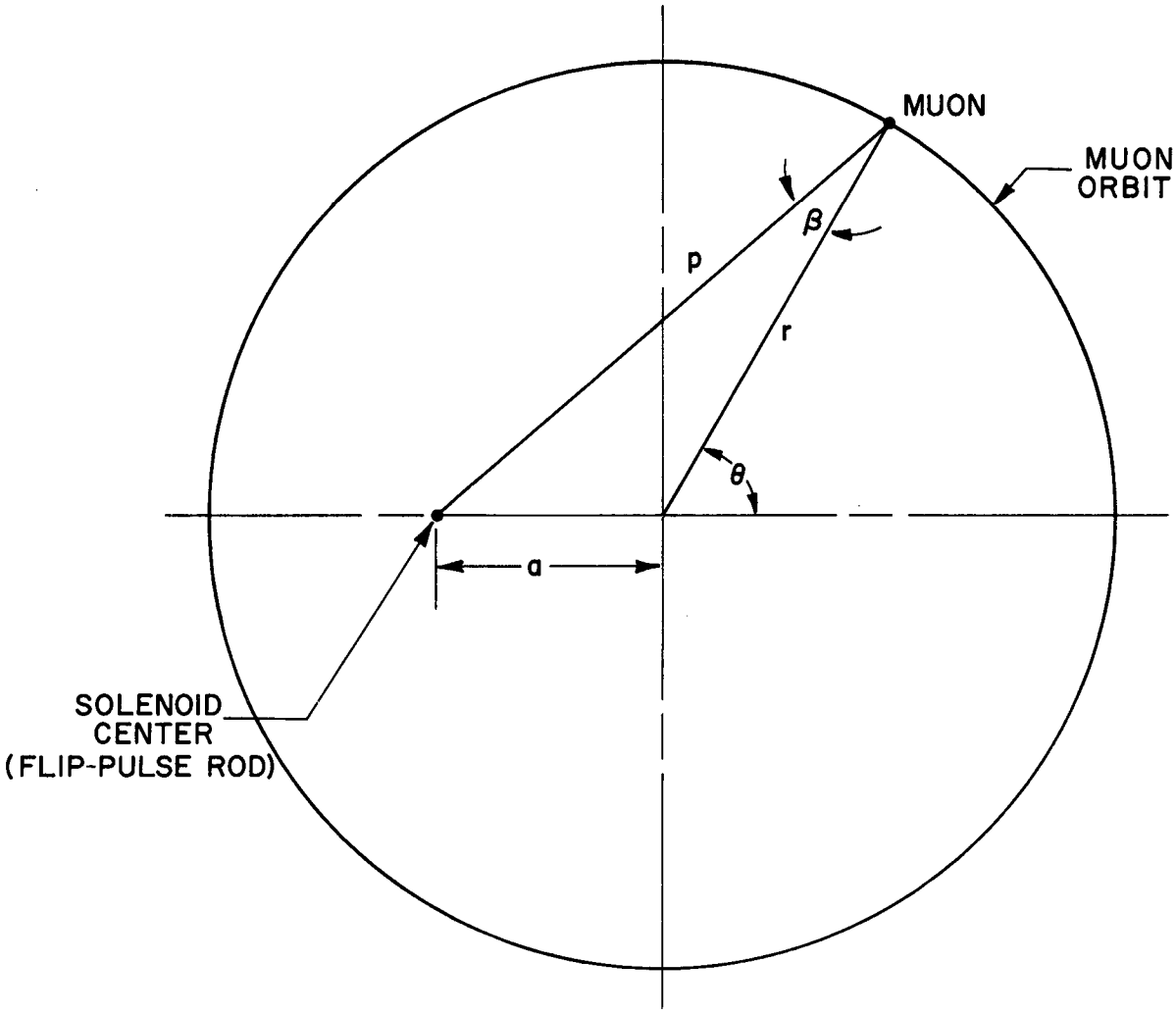

Fig. 37. Eccentric muon orbit in the solenoid.

and

$$\cos \beta = \frac{P^2 + r^2 - a^2}{2 Pr} \quad . \tag{87}$$

Substituting these values in the integral, we get

$$\overline{(B_{flip})}_\theta = \frac{B}{\pi} \int_0^\pi \left\{ \frac{1}{2r} + \frac{r^2 - a^2}{2r(a^2 - 2aP\cos\theta + r^2)} \right\} d\theta \tag{88}$$

$$= \frac{B}{2r} + \frac{B}{\pi} \frac{(r^2 - a^2)}{2r} I \, , \tag{89}$$

where

$$I \equiv \int_0^\pi \frac{d\theta}{(a^2 + r^2 - 2ar\cos\theta)} \quad . \tag{90}$$

This is a standard integral, and

$$I = \frac{\pi}{r^2 - a^2} \quad . \tag{91}$$

Thus

$$\overline{(B_{flip})}_\theta = \frac{B}{r} \quad , \tag{92}$$

which is identical to the expression for concentric orbits. Thus $\overline{(B_{flip})}_\theta$ is the same for all orbits looping the flip rod.

As shown in Sec. II.B, the $(g-2)_\mu$ spin precession in this frame of reference (the muon's cyclotron frame) is also adiabatic with respect to the muon's cyclotron period. In fact, the $(g-2)_\mu$ precession is less than $1/2°$ in one muon cyclotron period. The angle of spin flip in one muon cyclotron period is then very nearly proportional to the average $\overline{(B_{flip})}_\theta$, regardless of the eccentricity of the orbit. Thus, the <u>total</u> angle of spin flip is very nearly the same for concentric and nonconcentric muons, if the flip pulse is smooth and extends over several muon cyclotron periods. These conditions are fulfilled in the experiment.

FOOTNOTES AND REFERENCES

*Now at University of California, Santa Barbara.

†Now at CERN, Geneva, Switzerland.

1. J. Schwinger, Phys. Rev. 73, 416 (1948); and Phys. Rev. 76, 790 (1949).
2. R. Karplus, and N. M. Kroll, Phys. Rev. 77, 536 (1950).
3. H. Suura, and E. H. Wichmann, Phys. Rev. 105, 1930(L), (1957).
4. A. Petermann, Phys. Rev. 105, 1931(L), (1957).
5. C. M. Sommerfield, Phys. Rev. 107, 328(L), (1957).
6. A. Petermann, Nucl. Phys. 3, 689 (1957).
7. A. Petermann, Helv. Phys. Acta 30, 407 (1957).
8. C. M. Sommerfield, Ann. Phys. 5, 26 (1958).
9. A. Petermann, Nucl Phys. 5, 677 (1958).
10. G. Schrank, PPAD 304D (1960).
11. G. Charpak, F. J. M. Farley, R. L. Garwin, T. Muller, J. C. Sens, V. L. Telegdi, and A. Zichichi, Phys. Rev. Letters 6, 128 (1961).
12. G. Charpak, F. J. M. Farley, R. L. Garwin, T. Muller, J. C. Sens, and A. Zichichi, Nuovo Cimento 22, 1043 (1961).
13. G. Charpak, F. J. M. Farley, R. L. Garwin, T. Muller, J. C. Sens, and A. Zichichi, Proceedings of the International Conference on High Energy Nuclear Physics, Geneva, 1962, p. 476, (CERN Scientific Information Service, Geneva, Switzerland, 1962).
14. G. Charpak, F. J. M. Farley, R. L. Garwin, T. Muller, J. C. Sens, A. Zichichi, Nuovo Cimento 37, 1241 (1965).
15. R. A. Swanson, G. R. Henry, and G. Schrank, Beam Transport System, UCRL-11086, October 1963.
16. P. A. M. Dirac, Proc. Roy. Soc. A114, 243, (1927).
17. W. H. Louisell, R. W. Pidd, H. R. Crane, Phys. Rev. 94, 7 (1954).
18. A. A. Schupp, R. W. Pidd, and R. W. Crane, Bull. Am. Phys. Soc. Ser. II 4, 250 (1959).
19. D. F. Nelson, A. A. Schupp, R. W. Pidd, and H. R. Crane, Phys. Rev. Letters 2, 492 (1959).
20. A. A. Schupp, R. W. Pidd, and H. R. Crane, Phys. Rev. 121, 1 (1961).
21. D. T. Wilkinson, and H. R. Crane, Phys. Rev. 130, 852 (1963).

22. F. Bloch, Phys. Rev. 70, 460 (1046).
23. G. Schrank, and G. Henry, PPAD 323D (1960)
24. R. Hagedorn, CERN 62-18.
25. V. Bargmann, L. Michel, and V. Telegdi, Phys. Rev. Letters 2, 435 (1959).
26. G. Henry, G. Schrank, and R. Swanson, PPAD 506D (1963).
27. G. Schrank, R. Kreps, G. Henry, PPAD 320D (1960)
28. G. Henry, G. Schrank, PPAD 524E (1964) and PPAD 395D (1961).
29. G. Schrank, G. Henry, A. Kerns, R. Swanson, Rev. Sci. Instr. 35, 1326 (1964).
30. Jay Orear, Notes on Statistics for Physicists, UCRL-8417, August 1958.
31. E. J. Williams, Regression Analysis, (John Wiley and Sons, Inc., N. Y., 1959).
32. S. M. Berman, Proceedings of the International Conference on High Energy Nuclear Physics, Geneva, 1962, (CERN Scientific Information Service, Geneva, Switzerland, 1962)p. 870.
33. V. B. Berestetskii, O. N. Krokhin, and A. K. Khlebnikov, Soviet Phys., JETP 3, 761 (L) (1956-57).
34. S. D. Drell, and F. Zachariasen, Phys. Rev. 111, 1727 (1958).
35. S. D. Drell, Ann. Phys. 4, 75 (1958).
36. V. B. Berestetskii, Soviet Physics, JETP 12, 993 (1961).
37. C. G. Darwin, Proc. Roy. Soc. (London) A124, 425 (1929).
38. E. P. Wigner, Revs. Mod. Phys. 29, 255 (1957).
39. W. S. C. Williams, An Introduction to Elementary Particles (Academic Press, New York, 1961).
40. G. Ascoli, Zeit. Physik 150, 407 (1958).
41. S. Gorodetzky, Th. Muller, M. Port, and A. Zichichi, Phys. Rev. Letters 2, 133 (1962).